

ABSTRACT

CHEN, HONGJIANG. The Mechanical-Electrochemical Coupling Effects in Lithium-ion Batteries under Non-equilibrium Process (Under the direction of Dr. Hsiao-Ying Shadow Huang).

Lithium-ion batteries have been widely used from power tools and portable electronics to electric vehicles. However, Li-ion batteries' capacity loss and cycling aging at high (dis)charging rate (C-rate) have limited many potential applications and hindered development of emerging technologies. To improve the performance of Li-ion batteries, it is important to understand the coupling effect between the mechanical behaviors and the electrochemical response of electrodes, as the capacity loss and cycling aging are related to the mechanics of electrodes during (dis)charging. Moreover, based on the mechanical-electrochemical coupling effect, defects, such as dislocations, influence the states of electrodes in Li-ion batteries. However, few of study provided a systematic formulation that describes the coupling effect under strong non-equilibrium process (high C-rate) and large deformation. The dislocation-electrochemistry relation has only been observed experimentally and has not been fully clarified.

This research focuses on understanding the physical mechanisms of the mechanical-electrochemical coupling effect and revealing the role of dislocations in the state transformation of electrodes in Li-ion batteries under fast (dis)charging process. By utilizing elastic mechanics for dislocations, we simulate the anisotropic stress and displacement fields of a LiFePO_4 (LFP) particle containing different densities and orientations of dislocations. The kinetic performance influenced by the mechanical-electrochemical coupling effects are compared among different dislocation configurations in the LFP particle. In addition, to analyze the variations of phase transitions in electrodes, we model the free energy with path factors which depend on multi-layered states described by a series of order parameters, based on non-equilibrium

thermodynamics. The generation/annihilation of dislocations is coupled with the electrochemical reaction of Li-ion on the surface of electrode particles. The path of energy changing is dominated by the density of dislocations. Derived governing equations for the kinetics of the order parameters reveal the phenomena of abnormal phase transitions for LFP and layered oxides under high rate (de)lithiation, which agree with the existing experimental observations. Furthermore, to clarify the mechanical-electrochemical coupling effect for the electrodes with large deformation, we combine continuum mechanics, non-equilibrium thermodynamics, and variational theory to develop a generalized theory to describe the variations of Li-ion fractions, stress distribution, and electrode's finite deformation over non-equilibrium process. The simulation for a Sn anode particle compares the influences of different C-rates on the states of the particle and the polarization of electrical potential.

This research investigates the state evolutions for different electrodes of Li-ion batteries under non-equilibrium process, which provides insight to understand the features of electrodes and reveals strategies of improving the performance for Li-ion batteries.

© Copyright 2024 by Hongjiang Chen

All Rights Reserved

The Mechanical-Electrochemical Coupling Effects in Lithium-ion Batteries under Non-equilibrium Process

by
Hongjiang Chen

A dissertation submitted to the Graduate Faculty of
North Carolina State University
in partial fulfillment of the
requirements for the degree of
Doctor of Philosophy

Mechanical Engineering

Raleigh, North Carolina
2024

APPROVED BY:

Hsiao-Ying Shadow Huang
Committee Chair

Kara Peters

Liming Xiong

Veronica Augustyn

Nina Balke

DEDICATION

To my love, Min Lan

To my parents, Shanshun Chen and Fulian Dai

To my little boy coming soon, Maxwell Chen

Thank you for staying with me to complete this work.

ACKNOWLEDGMENTS

Thank North Carolina State University and Department of Mechanical & Aerospace Engineering for giving me the opportunity to pursue the Doctor of Philosophy degree.

Thank my advisor, Dr. Hsiao-Ying Shadow Huang for continued guidance and help.

Thank my committee members, Dr. Kara Peters, Dr. Liming Xiong, Dr. Veronica Augustyn, and Dr. Nina Balke for being willing to serve on my committee.

Thank my family for their support.

TABLE OF CONTENTS

LIST OF TABLES	vi
LIST OF FIGURES	vii
CHAPTER 1 Introduction and Literature Review	1
1.1 Basic Structure and Electrochemistry of Lithium-ion Batteries	1
1.2 Mechanical Behaviors in Lithium-ion Batteries	3
1.3 Dislocation Induced Stress and Electrochemical Performance	5
1.4 Rate Capability and the Variation of Phase Transitions	8
1.5 Formulation for the Electrodes with Finite Deformation	12
1.6 Research Scope	15
CHAPTER 2 Exploration of the Dislocation-Electrochemistry Relation in LiFePO ₄ Cathode Materials	17
2.1 Modeling Method.....	18
2.1.1 Mechanics of dislocations for LiFePO ₄ cathode particles	18
2.1.2 Kinetics of CV scan for LiFePO ₄ cathode particles.....	21
2.1.3 Algorithm and parameters.....	25
2.2 Results and Discussion	28
2.3 Conclusion	46
CHAPTER 3 Paths of Energy Change for Electrodes of Lithium-ion Batteries under Non-equilibrium Process.....	48
3.1 Modeling Method.....	48
3.1.1 Free energy with multi-layered states and path factors	48
3.1.2 Governing equations for the kinetics of main parameters	54
3.1.3 Numerical simulations	59
3.2 Results and Discussion	65
3.3 Conclusion	83
CHAPTER 4 Modeling and Simulation of the Non-equilibrium Process for a Continuous Solid Solution System in Lithium-ion Batteries.....	85
4.1 Modeling Method.....	86
4.1.1 General theory.....	86
4.1.1.1 Mass conservation and kinematics of continuums for solution systems	87
4.1.1.2 Momentum equation and energy equation.....	90
4.1.1.3 Equation of the entropy production rate	92
4.1.1.4 Constitutive relations of state functions.....	94

4.1.2 Simplification and application	96
4.1.2.1 Mass conservation and kinematics.....	97
4.1.2.2 Dissipation models of non-equilibrium process	100
4.1.2.3 Models of state functions	105
4.1.3 Numerical simulation.....	108
4.1.3.1 Transformation of equations and numerical method	108
4.1.3.2 Geometry and material parameters of the particle	111
4.1.3.3 Boundary conditions, initial conditions and deformation.....	115
4.2 Results and Discussions.....	119
4.3 Conclusion	141
CHAPTER 5 Summary.....	143
REFERENCES	147
APPENDIX A.....	157
APPENDIX B	159
B.1 Introduction to the Metric-based Kinematics of Finite Deformation.....	159
B.2 Generalized Mass Conservation Equation	163
B.3 Entropy Production Rate	165
B.4 Relative Chemical Potential	166
B.5 Transformed Equations	169
B.6 Relation between D and L.....	169
B.7 Differential of Expanded Surface Area.....	170
B.8 The Component of $v^L_{(2)}$ in the Lab Space	171

LIST OF TABLES

Table 2.1 Material parameters used for the simulation.	27
Table 3.1 Physical meaning of order parameters.	50
Table 3.2 Material parameters for LFP.	61
Table 3.3 Material parameters for NMC111.	63
Table 4.1 Material parameters used in the simulation.	114

LIST OF FIGURES

Figure 2.1 Stress fields and displacement fields of a Li_YFePO_4 particle for different dislocation densities when dislocation#1 with orientation-1 and phase fraction $x_p = 0.9$. Group A has dislocation#1 and 2. Group B has dislocation#1, 2, and 3. Group C has dislocation#1, 2, 3, and 4. Group D has dislocation#1, 2, 3, 4, and 5. The Burgers vectors of dislocation#1, 2, 3, 4, and 5 are (1, 0), (1, 0), (-1, 0), (1, 0), and (-1, 0) respectively. With a higher dislocation density, the larger average value of hydrostatic stress $\sigma_h = (\sigma_{xx} + \sigma_{yy} + \sigma_{zz}) / 3$ suggests a higher electrical potential of the particle. The sharp interfaces in displacement fields indicate where the slip planes of dislocations are located. 29

Figure 2.2 Stress fields and displacement fields of a Li_YFePO_4 particle for different dislocation densities when dislocation#1 with orientation-2 and phase fraction $x_p = 0.9$. Group A has dislocation#1 and 2. Group B has dislocation#1, 2, and 3. Group C has dislocation#1, 2, 3, and 4. Group D has dislocation#1, 2, 3, 4, and 5. The Burgers vectors of dislocation#1, 2, 3, 4, and 5 are (0, -0.6), (1, 0), (-1, 0), (1, 0), and (-1, 0) respectively. With a higher dislocation density, the larger average value of hydrostatic stress $\sigma_h = (\sigma_{xx} + \sigma_{yy} + \sigma_{zz}) / 3$ suggests a higher electrical potential of the particle. The sharp interfaces in displacement fields indicate where the slip planes of dislocations are located. 31

Figure 2.3 Stress fields and displacement fields of a Li_YFePO_4 particle for different dislocation densities when dislocation#1 with orientation-3 and phase fraction $x_p = 0.9$. Group A has dislocation#1 and 2. Group B has dislocation#1, 2, and 3. Group C has dislocation#1, 2, 3, and 4. Group D has dislocation#1, 2, 3, 4, and 5. The Burgers vectors of dislocation#1, 2, 3, 4, and 5 are (-1, 0), (1, 0), (-1, 0), (1, 0), and (-1, 0) respectively. With a higher dislocation density, the larger average value of hydrostatic stress $\sigma_h = (\sigma_{xx} + \sigma_{yy} + \sigma_{zz}) / 3$ suggests a higher electrical potential of the particle. The sharp interfaces in displacement fields indicate where the slip planes of dislocations are located. 32

Figure 2.4 CV curves for different dislocation densities of a Li_YFePO_4 particle, where dislocation#1 with (a) orientation-1 (1, 0), (b) orientation-2 (0, -0.6), and (c) orientation-3 (-1,

0). The scan rate of every CV curve is 16 mV/s. The gray region indicates the overpotential of two-phase coexistence ($0 < x_p < 1$). From group A to group D, the dislocation density increases. For every orientation of dislocation#1, the CV curve with a higher dislocation density shows a larger displacement relative to the CV curve with no dislocation. The displacement of CV curves consists of shift and distortion, which depend on the density and orientation of dislocations. For each dislocation density, orientation-3 (-1, 0) displays the strongest shift and distortion, and orientation-1 (1, 0) shows the weakest shift and distortion. The kinetic performance of electrodes may hence be promoted by increasing the dislocation density and adjusting the orientations of dislocations. 35

Figure 2.5 CV curves of a Li_YFePO_4 particle for different scan rates with different orientations of dislocation#1 and different dislocation densities. The gray region indicates the overpotential of two-phase coexistence ($0 < x_p < 1$). From group A to group D, the dislocation density increases. For every scan rate (v), the peak current density (the peak value of i) and peak overpotential ($\Delta\varphi$ corresponding to the peak current density) of CV curves depend on both the orientation of dislocation#1 and the dislocation density of the particle. The CV curves in group D with orientation-3 (-1, 0) (Figure 2.51) display the highest peak current density and peak overpotential for all scan rates, which implies the highest effective diffusivity of Li^+ and the largest electrical power. With a higher scan rate, dislocations have stronger effects on increasing the peak current density and peak overpotential, which suggests that the kinetic performance of the particle with a stronger non-equilibrium state may be promoted more by adjusting dislocations. 37

Figure 2.6 (a) $\Delta\sigma_{hAVG}$, the change of the average hydrostatic stress of a Li_YFePO_4 particle when the dislocation density increases, with phase fraction $x_p = 0$ and $x_p = 1$. $\Delta\sigma_{hAVG} > 0$ indicates that dislocations may help Li_YFePO_4 be in tension. The nonconstant $\Delta\sigma_{hAVG}$ shows the nonlinear relation between the stress and dislocation density. The difference of $\Delta\sigma_{hAVG}$ between $x_p = 0$ and $x_p = 1$ induced by the phase transformation suggests the different effects of dislocations for different states of charge (SOCs). **(b)** D_{RS} , the effective diffusivities calculated by the Randles-Sevcik equation [107] for different dislocation densities with different orientations of

dislocation#1. The particle with a larger dislocation density has a higher D_{RS} , especially for orientation-3 (-1, 0), which implies that increasing the dislocation density and adjusting the dislocation orientation may promote the kinetic performance of the electrodes in lithium-ion batteries. 39

Figure 3.1 Free energy of LFP vs. order parameters ζ^{III} and ζ^{IV} when dislocation density **(a)** $Y = 0$, **(b)** $Y = -2$, and **(c)** $Y = -4$. For 2-dimensional LFP model, the component of ζ^{IV} tensor, ζ_1^{IV} and ζ_2^{IV} , independently affect the probability density function (PDF) of Li^+ sites' location in (z_1, z_2) space. LFP shows crystal structure for **(d)** both directions when $\zeta_1^{\text{IV}} = 1$ and $\zeta_2^{\text{IV}} = 1$, and only one direction when **(e)** $\zeta_1^{\text{IV}} = 1$, $\zeta_2^{\text{IV}} = 0$ or **(f)** $\zeta_1^{\text{IV}} = 0$ and $\zeta_2^{\text{IV}} = 1$ 66

Figure 3.2 Scaled chemical potential of Li^+ in LFP at different fraction for **(a)** 0.1C delithiation, **(b)** 10C delithiation, and **(c)** 10C lithiation. The evolutions of main parameters with the same C-rates are recorded in **(d-f)** respectively. The order-disorder phase transition is revealed under **(g)** 30C delithiation, **(h)** 50C delithiation, and **(i)** 50C lithiation. 69

Figure 3.3 Simulated XRD graphs and electrical potentials for LFP under **(a)** 5C, **(b)** 10C, **(c)** 20C cycling, and **(d)** 90 seconds 10C delithiation followed by 270 seconds open circuit relaxation. The XRD peak location 0 and 1 indicate the lattice parameters of Li-rich phase and Li-poor phase under equilibrium state, respectively. The diffusional driving force coefficient A^L satisfies $A_\alpha^L RT / l_c = 0.1$ and $A_\beta^L RT / l_c = 0.3$ 72

Figure 3.4 Li^+ fraction profiles in ten LFP particles with different sizes that obey the log-normal distribution (mean size 186nm, standard deviation 0.35) during **(a)** 5C and **(b)** 20C cycling, and **(c)** 90 seconds 10C delithiation followed by 270 seconds open circuit relaxation. All particles are scaled to the same nondimensionalized size. Larger particles are marked by larger numbers. Based on the symmetry, all particles are simulated in half. The left end and the right end are respectively the center and the surface of every particle. 74

Figure 3.5 Simulated XRD graphs and electrical potentials for LFP under **(a)** 5C, **(b)** 10C, and **(c)** 20C cycling. The XRD peak location 0 and 1 indicate the lattice parameters of Li-rich phase and Li-poor phase under equilibrium state, respectively. The diffusional driving force coefficient A^L is a constant that satisfies $A_\alpha^L RT / l_c = A_\beta^L RT / l_c = 0.15$ 77

Figure 3.6 Profiles of (a) crystalline (ζ^{IV}) and (b) electrical current for a single LFP particle with size 300 nm during 4V vs Li/Li⁺ potentiostatic delithiation, where z_1 is the spatial coordinate of the particle. Only half of the particle is simulated due to symmetry. 79

Figure 3.7 Simulated XRD graphs and electrical potentials for NMC111 multi-particles under (a) C/15 and (b) 4C cycles. The XRD peak location 0 and 1 indicate the lattice parameters of fully lithiated and fully delithiated equilibrium state, respectively. The Li⁺ fraction profiles in ten particles with different sizes that obey the log-normal distribution (mean size 186nm, standard deviation 0.15) are shown in (c) for C/15 and (d) for 4C cycles. All particles are scaled to the same nondimensionalized size. Larger particles are marked by larger numbers. Based on the symmetry, all particles are simulated in half. The left end and the right end are respectively the center and the surface of every particle. 82

Figure 4.1 (a) A representative Sn anode particle used in the simulation. Initially, the particle is a spherical cap with a fillet. The radius of the spherical cap is 1.5 μm . The radius of the fillet between points C and D is 0.375 μm . The distance between the spherical center and the current collector is 0.75 μm . (b) The curves of the thermodynamic coefficient of diffusion L and the diffusivity D serve as functions of the molar fraction of occupied Li⁺ sites $y'_{(1)}$ 112

Figure 4.2 A representative evolution of several key parameters in Sn particle: Molar fraction of occupied Li⁺ sites $y'_{(1)}$, velocity of Li⁺ continuum relative to the Sn space $\mathbf{v}_{(1)}$, mass center velocity relative to lab space \mathbf{v}^L , hydrostatic elastic strain $\epsilon_H^{(e)}$, and relative chemical potential $\mu_{(12)}$ during lithiation (C-rate=3) and relaxation. $y'_{(1)}$ and $\mu_{(12)}$ increase with uneven distributions during lithiation, which indicates the non-equilibrium state of the system. During relaxation, the distributions of all parameters are gradually even, which represents the gradually weakened non-equilibrium state. The particle volume continues to increase during whole process because $\epsilon_H^{(e)}$ increases during both lithiation and relaxation. 121

Figure 4.3 (a) Plasticity rate $\lambda^{(p)}$ at SOC 0.1 and 0.5, followed by the relaxation until $t_R = 180$ s. The maximum plasticity rate locates near the bottom region of the particle. (b) Maximum plasticity rate in the particle during lithiation and relaxation with three different C-rates. During

lithiation, the maximum $\lambda^{(p)}$ of every particle initially increases and till reaching to a constant value. A higher C-rate indicates a higher maximum $\lambda^{(p)}$ 123

Figure 4.4 Hydrostatic elastic stress σ_H during lithiation (SOC = 0.1 – 0.5) and relaxation (t_R = 30-600 seconds) at three different C-rates (3C, 1.5C, and 0.75C). σ_H becomes negative during lithiation at all C-rates. $\sigma_H < 0$ means that free energy is decreased when particle volume is increased. Volume expansion is hence a spontaneous behavior of the particle. A higher C-rate corresponds, σ_H becomes more negative, which implies a faster decrease of free energy and a faster volume expansion of the particle. During relaxation, σ_H with all C-rates get close to zero with gradually even distributions, which indicate the slowdown of free energy change. 125

Figure 4.5 Hydrostatic viscous stress $\tau_H^{(e)}$ during lithiation (SOC = 0.1 – 0.5) and relaxation (t_R = 30-600 seconds) at three different C-rates (3C, 1.5C, and 0.75C). A higher C-rate indicates a higher $\tau_H^{(e)}$ which slightly decreases with increased SOC. During relaxation, $\tau_H^{(e)}$ with all C-rates are close to zero with gradually even distributions, which indicate that particles approach to the equilibrium state..... 127

Figure 4.6 Hydrostatic Cauchy stress p_H during lithiation (SOC = 0.1 – 0.5) and relaxation (t_R = 30-600 seconds) at three different C-rates (3C, 1.5C, and 0.75C). The negative value of p_H indicates that the particle is mostly in compression. The bottom region shows stronger compression than the bulk region due to the bonding between the particle and current collector. A higher C-rate and a higher SOC indicate a stronger uneven-distribution of p_H . The uneven distribution gradually disappears during relaxation, which indicates the particles approach to the equilibrium state..... 129

Figure 4.7 The evolution of whole cell voltage change $\Delta\phi$ induced by the anode during charging/relaxation at three different C-rates. A higher C-rate indicates a higher $\Delta\phi$ during lithiation. The relaxation stage of $\Delta\phi$ for every C-rate includes a steep decrease followed by a gentle decrease. A higher C-rate corresponds to a lower final voltage change $\Delta\phi$. Thus, the cell charged by a lower C-rate results in a higher voltage at the end of relaxation. 131

CHAPTER 1

Introduction and Literature Review

1.1 Basic Structure and Electrochemistry of Lithium-ion Batteries

The basic structure of typical lithium-ion batteries includes cathode, anode, separator, current collectors, and electrolyte [1]. The separator is placed between cathode and anode to prevent electrical short circuit. Li^+ can move between anode and cathode by diffusing in electrolyte and passing through the separator, meanwhile, free electrons flow between anode and cathode through the current collectors and the external circuit [2]. The intrinsic chemical potential of Li^+ in anode is higher than that in cathode, which produces a chemical force causing Li^+ to tend to move from anode to cathode [3]. In the open circuit condition, without the diffusion of Li^+ , the chemical force must be balanced by an electrostatic force generated by the difference of the electrical potentials between the electrodes [3]. The electrical potential difference between electrodes under the open circuit condition is called open circuit voltage, which is determined by the chemical potential difference of Li^+ between the electrodes [3]. If one electrode is defined as the reference electrode (i.e., zero electrical potential), the open circuit voltage is the open circuit potential of the other electrode (working electrode). In the charging (discharging) condition, the voltage between cathode and anode is higher (lower) than the open circuit voltage. This voltage deviation is caused by the polarization of electrodes, which involve following kinetic effects, (1) the activation of the electrochemical reactions, (2) the mass transport limitation of species, and (3) the resistance due to the contact problems between different phases and components in electrodes [4].

Currently, three classes of cathode materials have been widely applied in commercial Li-ion batteries: layered (LiCoO_2 and $\text{LiNi}_{1/3}\text{Mn}_{1/3}\text{Co}_{1/3}\text{O}_2$), spinel (LiMn_2O_4 and $\text{LiMn}_{3/2}\text{Ni}_{1/2}\text{O}_4$),

and olivine (LiFePO_4 and $\text{LiFe}_{1/2}\text{Mn}_{1/2}\text{PO}_4$), which respectively supply 2-D, 3D, and 1D diffusion channels for Li^+ [5]. For anode, graphite and alloys (Si, Sn) are typical candidates [6]. Different cathode/anode materials have different electrochemical reactions and open circuit electrical potentials. For example, the half-cell reactions and the corresponding average open circuit potentials (Volt, V) for LiCoO_2 , LiFePO_4 , and graphite are listed below,

$\text{LiCoO}_2 \rightleftharpoons \text{Li}_{1-x}\text{CoO}_2 + x\text{Li}^+ + xe^-$ with 4.2V vs. Li^0/Li^+ [5][7], $\text{LiFePO}_4 \rightleftharpoons \text{FePO}_4 + \text{Li}^+ + e^-$ with 3.45V vs. Li^0/Li^+ [5][8], and $6\text{C} + x\text{Li}^+ + xe^- \rightleftharpoons \text{Li}_x\text{C}_6$ with 0.1V vs. Li^0/Li^+ [6][7]. The above symbol Li^0/Li^+ represents the Li metal electrode, which is the reference electrode for measuring the open circuit potentials of the different electrodes. The overall reactions for LiCoO_2 and LiFePO_4 cathodes with the graphite anode are $\text{LiCoO}_2 + 6\text{C} \rightleftharpoons \text{Li}_{1-x}\text{CoO}_2 + \text{Li}_x\text{C}_6$ and $\text{LiFePO}_4 + 6\text{C} \rightleftharpoons \text{FePO}_4 + \text{LiC}_6$ respectively.

1.2 Mechanical Behaviors in Lithium-ion Batteries

During charging and discharging, the concentration changes of Li^+ in electrodes lead to the volume changes of electrodes [9][10]. Compared to the fully delithiated state, the volumes under fully lithiated state for $\text{LiNi}_{1/3}\text{Mn}_{1/3}\text{Co}_{1/3}\text{O}_2$, LiFePO_4 , and Sn are expanded by 5.1%, 4.2%, and 283% respectively [6][11][12]. The deformation can lead to the mechanical stress inside electrode particles, especially when the concentration of Li^+ is unevenly distributed due to the mass transport limitation or the phase separation [13]. The stress alters the chemical potential of Li^+ inside electrodes, which changes the voltages of Li-ion batteries. In addition, the stress may decrease the mechanical reliability of electrodes.

The performance and life of Li-ion batteries are related to the mechanical effects mentioned above, which have been revealed in several studies [14]. For example, Wang et al. [15] presented the crack-induced capacity fade of LiFePO_4 during cycling. Piper et al. [16] reported that compressive stress may decrease the effective specific capacity of Si anodes. Cycling-induced crack propagation of a single crystal Si anode was observed and simulated by Shi et al. [17]. For decreasing the capacity loss and improving the lifetime of Li-ion batteries, it is important to understand the relation between the mechanical behaviors and the electrochemical responses of Li-ion batteries.

The mechanical behaviors of electrodes include the stress and deformation induced by the diffusion of Li^+ . Based on the assumptions of infinitesimal deformation and diffusion of Li^+ governed by Fick's law, the diffusion-induced stress of a spherical electrode particle was analytically solved by Cheng and Verbrugge [18]. Due to the simplicity of Fick's law, the diffusion-induced stress may be simulated conveniently for more complicated geometry of electrodes [19], [20]. Kim et al. [21] used focused ion beam and scanning electron microscopy to

generate a reconstructed 3-D LiFePO₄ model, whose simulated diffusion-induced Von-Mises stress was higher for a larger (dis)charging rate (C-rate). However, Fick's law neglects the influence of mechanical behaviors on the diffusion of Li⁺. The stresses in electrodes have been shown to be coupled with lithium-ion diffusion and electrochemical reactions in several studies [16] [22] [23] [24] and furthermore influence the kinetic performance of Li-ion batteries. This influence may be reflected by the mechanical-chemical potential of Li⁺ which can be considered as part of the driving force of Li⁺ diffusion. To fully present the mechanical-diffusional coupling effect, some studies introduced the stress of electrode into their chemical potential models of Li⁺ [25] [26] [27] [28]. The stress-induced chemical potential of solid was initiated by Larche and Cahn [29] (Equation (1.1.1)):

$$\mu_{\sigma} = -\frac{1}{3}V_{PM}Tr(\boldsymbol{\sigma}), \quad (1.1.1)$$

where μ_{σ} is stress-induced chemical potential, V_{PM} is partial molar volume, Tr is trace operator, and $\boldsymbol{\sigma}$ is stress tensor. This coupling effect can be applied to describe the influences of dislocations on the performance of lithium-ion batteries.

1.3 Dislocation Induced Stress and Electrochemical Performance

As the lifetime and performance of Li-ion batteries relate to the existing cracks and the mechanical-diffusional-electrochemical coupling effect in electrodes, the influences of dislocations on the mechanical stress fields of electrodes have been investigated in several studies: Liu et al. [30] showed the coupling effect between dislocations, diffusion, and electrochemical reactions by modeling the stresses in a spherical electrode particle. Li et al. [31] simulated the cooperative surface and dislocation effects on the diffusion-induced stress in a spherical electrode particle. Zhu et al. [32] studied the dislocation effect on the diffusion-induced stress in a hollow spherical particle, in which the influence of the wall thickness of the hollow particle on the dislocation effect was discussed. Among the above contributions, dislocations were demonstrated to suppress the fractures in electrodes since the tensile stress in the particles could be reduced by the presence of dislocations. In contrast to the above positive influences of dislocations in electrodes, Yan et al. [33] observed the dislocation-based crack incubation mechanism in $\text{LiNi}_{1/3}\text{Mn}_{1/3}\text{Co}_{1/3}\text{O}_2$. Moreover, Singer et al. [34] reported that dislocation networks should be the origin of the voltage fade in lithium-rich layered oxides (LRLO) $\text{Li}_{1.2}\text{Ni}_{0.133}\text{Mn}_{0.533}\text{Co}_{0.133}\text{O}_2$ during cycling because of the crystal structural changes resulted from dislocations. Thus, dislocations may have both positive and negative effects on the performance of electrodes and associated complicated dislocation-involved mechanics and electrochemistry have not been fully clarified yet.

With the development of defect engineering [35] [36] [37], controlling the dislocations in electrodes has been considered as a potential strategy to improve the performance of Li-ion batteries. For example, in the study of Yan et al. [38], the engineered edge dislocations that were generated during the fabrication of Co_3O_4 electrodes modified the surface facets of Co_3O_4

nanosheets and improved the cycling efficiency of the electrodes. It was observed that engineered dislocations have helped alleviate the volume change during cycling, supplied more nucleation sites for phase transformations, and promoted the diffusion of lithium-ions and electrons. Nevertheless, using the engineered dislocations to further optimize the electrodes of Li-ion batteries still requires a comprehensive understanding of the influences of dislocations on the particle deformation, ionic diffusion, and electrochemical reactions of electrodes.

Most of the studies modeling the dislocation-involved stress fields in electrode particles were based on the assumption of isotropic materials while also neglecting the effect of the orientations of dislocations, which is over-simplified for an anisotropic material such as LiFePO_4 [12]. That is, material properties of LiFePO_4 varies during (de)lithiation due to molar fraction changes of lithium [12][39]. Huang and Wang [40] had first incorporated a model from Indenbom and Lothe [41] to elucidate the mechanical effects of the dislocation orientation in a LiFePO_4 particle. Furthermore, Dhiman and Huang [42] studied the influences of phase separation induced by the lithium molar fraction variations and different dislocation orientations on cyclic voltammetry (CV) behaviors for a LiFePO_4 particle. Specifically, the stress field were studied while incorporating the electrochemical reaction by using the modified Butler Volmer equation [42] [43].

In addition, dislocations can appear not only due to the fabrication of electrodes but also during the (dis)charging cycling. The state of charge (SOC) of an electrode particle is an important factor generating an array of dislocations in a particle during (de)lithiation. For example, in a thin film anode, lithiation speed and the diffusion layer thickness, which represent the SOC, highly impacted the nucleation and density distribution of the misfit dislocations in the anode, as reported by Li et al. [44]. Ulvestad et al. [45] observed that the dislocation lines in a

nano-sized $\text{LiNi}_{0.5}\text{Mn}_{1.5}\text{O}_4$ cathode particle moved towards the boundary of the particle, in which the positions of the dislocation lines depended on the SOC of the particle. Nevertheless, the relation between the dislocation density and the SOC is electrode material dependent. Singer et al. [34] reported that the dislocation density of the LRLO particles is much more sensitive to electrical potential (i.e., an indicator of the SOC), compared to the $\text{LiNi}_{0.8}\text{Co}_{0.15}\text{Al}_{0.05}\text{O}_2$ (NCA) particle. Moreover, the correlation of the dislocation density to the electrical potential for the LRLO particles is observed to be related to the geometries of the particles [34]. Aforementioned studies suggest that these characteristics of dislocations have substantial effects on the electrochemical performance, which has not yet been investigated for LiFePO_4 . Due to the anisotropy of LiFePO_4 , it is arguable that the dislocation density should have a strong influence on the dislocation orientation, and vice versa.

To further understand the effects of dislocations on the anisotropic electrodes with phase transformations such as LiFePO_4 , we focus on the influences of the dislocation density and orientation, the associated effective diffusivities of a LiFePO_4 particle, as well as the related electrochemical performance of LiFePO_4 . Based on linear elastic mechanics, the superposition principle, and the mechanical-electrochemical coupling effect, the stress fields, displacement fields, and CV curves at different scan rates are studied and discussed.

1.4 Rate Capability and the Variation of Phase Transitions

As one of the essential attributes for the Li-ion batteries needed to be (dis)charged rapidly, rate capability indicates the efficiency, stability, and reliability when batteries are under non-equilibrium process. Higher rate capability suggests that Li-ion batteries have less voltage polarization (power loss), more (dis)charged capacity (Coulombic efficiency), and slower aging (irreversible capacity loss) under high current (dis)charging. The phase transitions of electrodes have been considered as a significant factor influencing the rate capability of Li-ion batteries. The energy barriers of the nucleation and growth of new phases can be reflected in the chemical potential of Li and thus decrease the rate capability of electrodes by increasing the voltage polarization[46][47]. Compared to the solid solution phase, Li-rich and Li-poor phases have much lower Li^+ diffusivity due to lack of interaction frequency between Li^+ and vacancy, which suggests the larger voltage polarization. Phase transition induced voltage polarization with a higher electrical current makes the charging/discharging voltage arrives its maximum/minimum earlier, which decreases the total charged/discharged capacity[48][49][50][51]. The inhomogeneous stress field and the stress concentration caused by the Li^+ miscibility gap for phase separation [13][52] decrease the mechanical reliability of electrode particles [53][54], which can be aggravated by higher (dis)charging rates (C-rates)[55][21][19]. Understanding and controlling the phase transitions of electrodes are therefore crucial for improving the rate capability of Li-ion batteries.

Several studies applied diffraction techniques to seek the factors influencing the miscibility gap of Li^+ in LiFePO_4 (LFP), a commercialized cathode material with two phases separation [39], under equilibrium state. Kobayashi et al. [56] reported that the miscibility gap of Li^+ in LFP decreases with decreased particle size at room temperature, and finally disappears

when particles are less than the limit size 40nm. Meethong and Huang [57] observed the LFP samples with different particle sizes under different temperatures, whose miscibility gaps are decreased with increased temperatures and decreased particle sizes, with the limit size around 10-25nm for temperature from -20°C to 45°C. Besides particle size and temperature, the miscibility gap of Li⁺ in a nanosized LFP particle is strongly dependent on the overall Li⁺ composition of the particle, which is concluded by Wagemaker et al. [58]. The above changes of miscibility gap in LFP can be attributed to the coherency between Li-rich phase and Li-poor phase. To minimize the total free energy of particles, coherency induced interfacial strain energy strongly suppresses the phase separation and promotes the rate capability for LFP, as mentioned in Cogswell et al. [59] and Kasavajjula et al. [60]. However, even though the phase separation is suppressed by the coherency strain, the coherency induced inhomogeneous stress is an inevitable factor decreasing the mechanical reliability of particles [61].

Besides decreasing the particle size, increasing the (dis)charging current can also suppress the phase separation for LFP. The operando Li⁺ composition of LFP particles in Lim et al. [62] shows solid solution at high C-rates ($>\sim 1C$), phase separation at low C-rates ($<\sim 0.4C$), and sharp interface between Li-rich and Li-poor zones after relaxation. The phase suppression for LFP under non-equilibrium process are also observed using diffraction techniques in Zhang et al. [63], Liu et al. [64], and Sharma et al. [65], where the diffraction peaks change their locations gradually instead of keeping static during (de)lithiation and recover to the normal locations of Li-rich and Li poor phases after relaxation. In addition, strong non-equilibrium can change the structure of LFP from order to disorder. The in-situ transmission electron microscopy (TEM) graphs in Niu et al. [66] display that LFP nanowires show meta-stable coexistence between crystal structure and amorphous structure under potentiostatic delithiation, during which

the amorphous structure locates by the boundary of nanowires. The crystal structure of LFP supplies a 1-dimensional channel for Li^+ diffusion [67]. The structure change should alter the diffusion coefficient tensor of Li^+ which is an important parameter influencing the rate capability. The formation of the non-equilibrium solid solution phase for LFP has been modeled in Bai et al. [68], in which the core factor controlling the suppression is the sensitivity of the exchange current density upon Li^+ concentration. Zhao et al. [69] applied population dynamics to explain and model the diffraction graphs revealing the solid solution phases for LFP under nonequilibrium process. The modeling methodology in Zhao et al. [69] is designing the kinetics relation between the changing rate of Li^+ concentration and Li^+ concentration for counteracting the intrinsic driving force of phase separation, which is essentially equivalent to the methodology in Bai et al. [68]. However, the suppression symmetry between delithiation and lithiation in the results of both Bai et al. [68] and Zhao et al. [69] does not agree with that in experiments [62] [64]. The order-disorder transition of LFP under strong non-equilibrium state observed in Niu et al. [66] cannot be explained by the methodology in Bai et al. [68] and Zhao et al. [69].

To improve the rate capability, suppressing the phase separation is necessary for not only LFP, but also layered oxides. As the cathode materials with a single solid solution phase under equilibrium [39], layered oxides can generate phase separation under non-equilibrium delithiation, as shown in the XRD graphs in Li et al. [70], Lee et al. [71], Yoon et al. [72], and Zhou et al. [73]. Unlike LFP, the variation of the phase transition for layered oxides is not symmetric between delithiation and lithiation, i.e., the phase separation only appears during delithiation. Grenier et al. [74][75] and Robert et al. [76] attribute the variation of phase transition in layered oxides to the change of chemical reaction coefficient on particle surfaces and the insufficient Li^+ mobility at the beginning of delithiation. However, quantitative

simulation and analysis were not supplied to validate the explanation in their studies. By combining the change of Li^+ mobility and the population effect, Park et al. [77] simulated the variation of phase transition for layered oxides. The modeling methodology used in Park et al. [77] for layered oxides is equivalent to that for LFP in Bai et al. [68] and Zhao et al. [69], with the different material properties for the opposite kinetic effect, i.e., suppressing the phase separation for LFP and promoting the phase separation for layered oxides. In contrast to LFP, the asymmetry caused by the modeling methodology agrees with the observations for layered oxides mentioned above. However, the methodology generates strong asymmetry in the capacity loss between lithiation and delithiation, which is reflected in Park et al. [77] but much larger than that in experiments [70][74][75][76].

Therefore, existing contributions cannot well explain the variations of phase transitions for the electrodes under non-equilibrium processes. To seek a strategy for enhancing the rate capability of Li-ion batteries, this study considers that the phenomena (1) the variations between phase separation and solid solution for LFP and layered oxides and (2) the order-disorder phase transition for LFP structure are caused by the same mechanism but different material properties. As the density and orientation of dislocations can affect the stress and strain field in electrodes [10], the free energy change induced by dislocations causes the state transformation of electrode materials. Because dislocations are local defects throughout the crystal structure, increased dislocation may ruin the crystal structure and finally lead to the disorder. The mechanical-electrochemical coupling effect [9] connects dislocations to the evolution of structural states. This connection plays a significant role in our mechanism for the variation of phase transitions in electrode materials.

1.5 Formulation for the Electrodes with Finite Deformation

Deformation is one of the essential factors in the mechanical-electrochemical coupling effect. The diffusion induced deformation in LiFePO_4 and layered oxides are usually analyzed using linear elastic mechanics since their volume deformation for full charging is around 4%, which is acceptable for the linear elasticity [12]. Moreover, the deformation induced by a single dislocation is also small enough relative to the whole particle [10]. To include the mechanical-electrochemical effect, the stresses corresponding to both diffusion induced deformation and dislocation induced deformation can be directly substituted in Larche and Cahn stress induced chemical potential model (Equation (1.1.1)) when strains are small enough. The Larche-Cahn model is derived from the linear theory of elasticity and thus should be used based on the assumption of infinitesimal deformation. However, many alloy anodes of Li-ion batteries have large volume expansion and contraction during lithiation and delithiation, respectively [6][78]. In studies of modeling the finite deformation of electrodes, the mechanical-chemical potentials were formulated based on the Larche-Cahn model, even though the assumption of infinitesimal deformation is not possible [26] [27] [79] [80] [81] [82] [83] [84]. A formulation for the mechanical-diffusional coupling effect of the electrodes with finite deformation is still unclear.

The diffusion of Li^+ in an electrode is coupled with not only the mechanical behaviors but also the electrical potential of the electrode since the electrochemical reaction is related to the mechanical-chemical potential of Li^+ . The electrode at a higher (dis)charging rate (C-rate) has more capacity loss [85] and cycling aging [86], which may be related to the viscous effect of the electrode via the mechanical-chemical potential during faster deformation at the higher C-rate. The dissipation effect could become significant with larger deformation in electrodes because of their faster strain rates. However, few studies formulated the mechanical-diffusional-

electrochemical coupling effect with solid viscosity. To this end, we adapt a non-equilibrium process with finite deformation to fully describe electrodes exhibiting different evolutions of strain and stress during lithiation/delithiation at different C-rates.

In addition, the diffusion of Li^+ can form creep strain or convection in an electrode continuum. On the scale of continuum, different atoms are indistinguishable. The stress of an electrode should be the statistical average of the atom interaction in the electrode [87]. Hence Li^+ should share the stress and be treated as a part of the electrode. The electrode mass flow induced by Li^+ diffusion corresponds to a partial deformation of the electrode continuum. This deformation can be considered as diffusion-induced creep strain [88]. In the measurement from Pharr et al. [89], the variation of electrical potential of a Si film electrode demonstrated transient trend reversal with each change of C-rate. This phenomenon may be related to the diffusion induced creep strain, as C-rate can directly influence the diffusion-induced creep strain. Selecting the matrix of the electrode, such as Si atoms of Si alloy anode, as the material configuration of deformation may mathematically obviate the diffusion-induced creep strain, meanwhile the convection induced by the mass flow must be included in the formulation of electrodes. To close this knowledge gap, we consider the diffusion-induced creep strain and/or the convection effect of electrodes in the current study.

Furthermore, the diffusion of Li^+ can generate phase separation for some electrode materials, such as LiFePO_4 , graphite and Si [6][90]. The diffusion-induced stress may be influenced by the phase separation [91]. Many studies that considered the phase separation and the mechanical-diffusional coupling effect incorporate a sharp interface between Li-rich phase and Li-poor phase [82] [92] [93], but the sharp interface can only be applied to special geometries such as film or spherical electrodes. To address this current limitation, our study

includes a continuous phase field in the formulation of electrodes to present the phase separation for general geometries.

In this research, based on the continuum mechanics [94] [95], non-equilibrium thermodynamics [96] and variational theory [97], a formulation including convection effect is developed for the non-equilibrium process with finite deformation in electrodes of Li-ion batteries. Mechanics, diffusion, phase transformation, chemical reaction and electrical potential are fully coupled with each other in the formulation. We start with basic axioms such as mass conservation and the 1st law of thermodynamics to develop a general theory. The general theory is then applied to a simplified Li-Sn system. A set of equations is numerically solved for a Sn anode particle with an initial spherical cap geometry. This research uses a rigorous mathematical formulation to develop a generalized method to describe the evolutions of mechanical-electrochemical behaviors of electrodes during (dis)charging at various C-rates.

1.6 Research Scope

The goal of this research is to understand and model the states evolution of electrodes in Lithium-ion batteries during fast charging and discharging process, based on continuum mechanics and non-equilibrium thermodynamics. In our formulation, the mechanical behavior, Li^+ diffusion and electrochemical reaction in electrodes are coupled together, which is known as the mechanical-electrochemical coupling effect. The mechanism of the influences of material defects, i.e., dislocations, on the electrochemical performance and phase transitions are elucidated, in which the mechanical-electrochemical coupling effect plays a significant role. Specifically, this research includes the following objectives.

In CHAPTER 2, we investigate the effects of fixed dislocations on the electrochemical performance of LiFePO_4 cathode. Based on dislocation mechanics and linear stress-induced chemical potential model, we numerically simulate the stress and displacement field induced by fixed dislocations in a single LiFePO_4 particle. Cyclic voltammetry (CV) curves are generated for presenting the kinetic performance of the particle. We compare the mechanical responses and effective diffusivities for different densities and orientations of dislocations.

In CHAPTER 3, we study the mechanisms of phase transition for electrodes. Dislocations and the mechanical-electrochemical coupling effect complicate the structure evolution during non-equilibrium process. Based on non-equilibrium thermodynamics, the abnormal phase transition patterns for LiFePO_4 and layered oxides cathode during fast (de)lithiation are elucidated. The crystal-amorphous structure change for LiFePO_4 under strong non-equilibrium state is included in the model. The dislocation in this part is kinetic with density change. The mechanism and model are validated by comparing (1) numerically simulated XRD graphs to reported experimental XRD graphs for LiFePO_4 and layered oxides multiple particles

respectively, and (2) numerically simulated order-disorder phase field with experimental TEM graphs for a single LiFePO_4 nanowire.

In CHAPTER 4, to study the electrodes with large deformation, the modeling formulation is expanded to finite deformation, by combining continuum mechanics, non-equilibrium thermodynamics and variational theory. Solid viscosity, convection and diffusion induced creep are included. The rigorous mathematical formulation starts with developing a general theory based on fundamental axioms. Then the general theory is applied to a simplified Li-Sn system. Derived governing equations are numerically solved for a Sn particle. The simulation results compare the evolutions of mechanical and electrochemical responses at various C-rates.

CHAPTER 5 summarizes the conclusions of this research.

CHAPTER 2

Exploration of the Dislocation-Electrochemistry Relation in LiFePO₄ Cathode Materials

This chapter focuses on the influences of a few characteristics of dislocations on the electrochemical performance of an anisotropic cathode material, lithium iron phosphate (LiFePO₄). Utilizing linear elastic mechanics and the superposition principle, we study stress and displacement fields of a LiFePO₄ particle containing different densities and orientations of dislocations. With the mechanical-electrochemical coupling effects expressed by the modified Butler-Volmer equation and using the finite different method, the cyclic voltammetry curves for different dislocation configurations in the particle are investigated.

The contents in this chapter are reproduced based on the published work below, Hongjiang Chen, Sangwook Kim, Hsiao-Ying Shadow Huang, “Exploration of the dislocation-electrochemistry relation in LiFePO₄ cathode materials”, *Acta Materialia*, Volume 237, 2022, 118158, ISSN 1359-6454, <https://doi.org/10.1016/j.actamat.2022.118158>.

2.1 Modeling Method

2.1.1 Mechanics of dislocations for LiFePO₄ cathode particles

The stress field resulted from a dislocation in a anisotropic material LiFePO₄ particle is calculated using Equation (2.1.1) [41] as shown below,

$$\sigma_{ij} = \frac{b_x \lambda (C_{12} - \bar{C}_{11})}{4\pi q^2 \tau^2 \bar{C}_{11} C_{66} \sin \phi} \left\{ \begin{array}{l} C_{ij11} [(\bar{C}_{11} + C_{12} + C_{66}) r_x^2 r_y + \lambda^2 C_{66} r_y^3] \\ -C_{ij12} (\bar{C}_{11} + C_{12}) (r_x^3 - \lambda^2 r_x r_y^2) \\ -\frac{C_{ij22}}{C_{22}} [(C_{12}^2 + \bar{C}_{11} C_{12} + 2C_{12} C_{66} + \bar{C}_{11} C_{66}) r_x^2 r_y - \bar{C}_{11} C_{66} \lambda^2 r_y^3] \end{array} \right\}, \quad (2.1.1)$$

$$-\frac{b_y \lambda (C_{12} - \bar{C}_{11})}{4\pi q^2 \tau^2 \bar{C}_{11} C_{66} \sin \phi} \left\{ \begin{array}{l} C_{ij22} [(\bar{C}_{11} + C_{12} + C_{66}) \lambda^2 r_x r_y^2 + C_{66} r_x^3] \\ -C_{ij12} (\bar{C}_{11} + C_{12}) (\lambda^2 r_y^3 - r_x^2 r_y) \\ -\frac{C_{ij11}}{C_{11}} [(C_{12}^2 + \bar{C}_{11} C_{12} + 2C_{12} C_{66} + \bar{C}_{11} C_{66}) \lambda^2 r_x r_y^2 - \bar{C}_{11} C_{66} r_x^3] \end{array} \right\}$$

with $\bar{C}_{11} = (C_{11} C_{22})^{1/2}$, $\lambda = (C_{11} / C_{22})^{1/4}$, $\phi = \frac{1}{2} \cos^{-1} \left(\frac{C_{12}^2 + 2C_{12} C_{66} - \bar{C}_{11}^2}{2\bar{C}_{11} C_{66}} \right)$,

$q^2 = r_x^2 + 2r_x r_y \lambda \cos \phi + r_y^2 \lambda^2$, and $\tau^2 = r_x^2 - 2r_x r_y \lambda \cos \phi + r_y^2 \lambda^2$, where σ_{ij} is the stress component of the particle, (b_x, b_y) is the Burgers vector of the dislocation, C_{ij} and C_{mnpq} are the engineering component and the theoretical component of the stiffness tensor of the particle respectively, (r_x, r_y) is the radius vector in the particle with respect to the dislocation core.

The displacement field resulted from a dislocation in a anisotropic material LiFePO₄ particle is calculated using Equation (2.1.2) and Equation (2.1.3) [41] as shown below,

$$u_x = \frac{b_x}{4\pi} \left[\omega + \frac{\bar{C}_{11}^2 - C_{12}^2}{2\bar{C}_{11} C_{66} \sin 2\phi} \ln \left(\frac{q}{\tau} \right) \right] + \frac{b_y}{4\pi \lambda \bar{C}_{11} \sin 2\phi} \left[(\bar{C}_{11} - C_{12}) \cos \phi \ln(q\tau) - (\bar{C}_{11} + C_{12}) \eta_x \sin \phi \right]$$

,(2.1.2)

$$u_y = -\frac{\lambda b_x}{4\pi \bar{C}_{11} \sin 2\phi} \left[(\bar{C}_{11} - C_{12}) \cos \phi \ln(q\tau) - (\bar{C}_{11} + C_{12}) \eta_y \sin \phi \right] + \frac{b_y}{4\pi} \left[\omega - \frac{\bar{C}_{11}^2 - C_{12}^2}{2\bar{C}_{11} C_{66} \sin 2\phi} \ln\left(\frac{q}{\tau}\right) \right] \quad (2.1.3)$$

where u_x and u_y are the horizontal and the vertical components of the displacement respectively. ω , η_x , and η_y are named auxiliary angles.

During lithiation and delithiation, a LiFePO₄ cathode particle has three stages: Li-poor phase, Li-rich phase, and two-phase coexistence [39]. Both Li-poor and Li-rich phases have the orthorhombic crystal structure [98], which satisfies the symmetry prerequisite of Equations (2.1.1), (2.1.2), and (2.1.3) [41]. The material properties (i.e., stiffness coefficients) of the particle at each stage during (de)lithiation are different [12]. In the two-phase coexistence region, we assume that the overall stiffness of the particle is a linear function (i.e., rule of mixture) of the phase fraction of the Li-rich phase: $C_{ij} = (1 - x_p) C_{(FePO_4)ij} + x_p C_{(LiFePO_4)ij}$, where x_p is the Li-rich phase fraction, $x_p = 0$ indicates the single Li-poor phase, $x_p = 1$ indicates the single Li-rich phase, $C_{(FePO_4)ij}$ is the stiffness component of the Li-poor phase, and $C_{(LiFePO_4)ij}$ is the stiffness component of the Li-rich phase [19] [99] [100]. This chapter emphasizes the influence of dislocation-induced stress on electrochemical performance. The material properties (i.e., stiffness and partial molar volume) of LiFePO₄ are assumed to be independent of dislocations for simplicity.

The auxiliary angles ω , η_x , and η_y in Equations (2.1.2) and (2.1.3) are obtained by numerically solving the equations below,

$$[D_\Psi] \cdot \omega = \frac{2 \sec^2(\Psi) \sin(\phi) [\lambda + \lambda^3 \tan^2(\Psi)]}{1 - 2\lambda^2 \cos(2\phi) \tan^2 \Psi + \lambda^4 \tan^4 \Psi}, \quad (2.1.4)$$

$$[D_\Psi] \cdot \eta_x = -\frac{2\lambda^2 \sec^2(\Psi) \sin(2\phi) \tan \Psi}{1 - 2\lambda^2 \cos(2\phi) \tan^2 \Psi + \lambda^4 \tan^4 \Psi}, \quad (2.1.5)$$

$$[D_\Psi] \cdot \eta_y = \frac{2\lambda^2 \csc^2(\Psi) \sin(2\phi) \cot \Psi}{\lambda^4 - 2\lambda^2 \cos(2\phi) \cot^2 \Psi + \cot^4 \Psi}, \quad (2.1.6)$$

with the boundary conditions $\omega(\Psi = 0) = 0$, $\eta_x(\Psi = 0) = 0$, and $\eta_y(\Psi = 0) = 0$, where Ψ is the azimuth relative to the Burgers vector, with the range $-\pi < \Psi \leq \pi$, and $[D_\Psi]$ is the finite difference matrix with respect to Ψ . The derivation of Equations (2.1.4), (2.1.5) and (2.1.6) are shown in the **Error! Reference source not found.**

We use the superposition principle to calculate the stress and displacement fields induced by multiple dislocations in a LiFePO₄ particle: the overall stress and displacement of a particle are the summations of the stress and displacement resulted from each dislocation calculated using Equations (2.1.1), (2.1.2), and (2.1.3). For simplicity, we use a 2-D particle model with the plane strain condition to investigate the stress and displacement fields resulted from dislocations. The geometry of the particle model is adapted from Dhiman and Huang [42], which is a rectangle of 100 nm × 60 nm, containing 60 unit cells. The size of the region dominated by the nonlinear deformation around a dislocation core is about 4 nm × 4 nm [101], which is small enough compared to the size of the particle model. As the nonlinear effect is negligible, Equations (2.1.1), (2.1.2), and (2.1.3) are valid for the particle size 100 nm × 60nm. We define the center of the rectangle as the origin of the Cartesian coordinate frame, in which the coordinate ranges of the particle are [-50 nm, 50 nm] for the x-axis and [-30 nm, 30 nm] for the y-axis. We assumed that the length of a dislocation line in our particle model is 90% of the particle thickness along the z direction, hence the dislocation density for one dislocation is $1.5 \times 10^{10} \text{ cm}^{-2}$, which agrees with the measurement in Singer et al. [34].

To investigate the influences of the density and orientation of dislocations, we assign five dislocations at different locations: dislocation#1 at (-20 nm, -12 nm) with three different Burgers vector directions discussed below, dislocation#2 at (40 nm, 24 nm) with the Burgers vector (1, 0), dislocation#3 at (25 nm, -15 nm) with the Burgers vector (-1, 0), dislocation#4 at (-40 nm, 17 nm) with the Burgers vector (1, 0), and dislocation#5 at (0, -24 nm) with the Burgers vector (-1, 0). Three Burgers vector directions at dislocation#1 are chosen from the set $\{(1, 0), (0, -0.6), (-1, 0)\}$, where (1, 0) is named orientation-1, (0, -0.6) denotes orientation-2, and (-1, 0) represents orientation-3. Five dislocations compose four groups with different dislocation densities for simulations: group A contains two dislocations (i.e., dislocation#1 and dislocation#2), group B contains three dislocations (i.e., dislocation#1, dislocation#2, and dislocation#3), group C contains four dislocations (i.e., dislocation#1, 2, 3, and 4), group D contains five dislocations (i.e., dislocation#1, 2, 3, 4, and 5), where each group includes three different orientations of dislocation#1 (i.e., (1, 0), (0, -0.6), or (-1, 0)).

2.1.2 Kinetics of CV scan for LiFePO₄ cathode particles

During the CV scan of a LiFePO₄ cathode material, the difference between the instant electrical potential of the particle and the equilibrium electrical potential of two-phase coexistence is named “overpotential” and denoted by $\Delta\phi$, whose range is $-0.3 \text{ V} < \Delta\phi < 0.3 \text{ V}$. In a complete scan cycle, $\Delta\phi$ changes from 0.3 V to -0.3 V with a scan rate v , and then increases back to 0.3 V with the same v . To present the detailed influences of dislocations on the kinetic performance of LiFePO₄ materials, we simulate 5 different scan rates: 1mV/s, 2mV/s, 4mV/s, 8mV/s, and 16mV/s. Collectively, a total of 61 simulations are conducted, including the case of perfect crystals with no dislocations.

As mentioned in Tang et al. [102], the required activation energy for the phase transformation from Li-rich phase to Li-poor phase decreases with increased $\Delta\varphi$, and eventually reaches zero at the critical overpotential $\Delta\varphi_c$. In this regard, a LiFePO₄ particle would spontaneously exhibit the single Li-poor phase when $\Delta\varphi \geq \Delta\varphi_c$. During the quasi-equilibrium process, $\Delta\varphi_c$ has the lowest value $\Delta\varphi_c^* = 30.283$ mV [102]. As CV scans are non-equilibrium processes, the required $\Delta\varphi_c$ for CV scans should be higher than $\Delta\varphi_c^*$ due to electrochemical polarization [103]. Although the electrochemical polarization should be different for different electric currents, the required overpotential of LiFePO₄ for generating Faradic current may show little variations in the CV scans at different scan rates, which is around 60 mV for scan rates from 0.5mV/s to 15mV/s [104] [105]. The total $\Delta\varphi_c$ hence should be around 90mV for different scan rates. For the sake of simplicity, we select that $\Delta\varphi_c = 3\Delta\varphi_c^*$ in our simulation of CV scans with all five scan rates mentioned above (i.e., 1mV/s, 2mV/s, 4mV/s, 8mV/s, and 16mV/s). In addition, the critical overpotential of the phase transformation should have two values: a higher value and a lower one to present two boundaries at the two-phase coexistence region. The higher value $\Delta\varphi_c$ is the lowest overpotential for the Li-poor single phase ($x_p = 0$), and the lower value is the highest overpotential for the Li-rich single phase ($x_p = 1$). The lower value indicates the critical point of zero activation energy for the phase transformation from Li-poor phase to Li-rich phase. For simplicity, it is acceptable to assume that the transformation from Li-poor phase to Li-rich phase is symmetric to the transformation from Li-rich phase to Li-poor phase, which indicates that the overpotential region of the single Li-rich phase is $\Delta\varphi \leq -\Delta\varphi_c$. Thus, the phase fraction x_p may be considered as a piecewise function of $\Delta\varphi$ as follows: $x_p = 0$ for $\Delta\varphi \geq \Delta\varphi_c$; $0 < x_p < 1$ for $-\Delta\varphi_c < \Delta\varphi < \Delta\varphi_c$; and $x_p = 1$ for $\Delta\varphi \leq -\Delta\varphi_c$, where x_p is assumed to be a linear function

of $\Delta\varphi$ in the two-phase coexistence region ($0 < x_p < 1$). The stiffness coefficients of the particle during the two-phase coexistence depend on the phase fraction x_p when $\Delta\varphi$ decrease from 90.849 mV to -90.849 mV.

As the process of the phase transformation during CV scans has been explicitly elucidated, we may use Fickian diffusion to simplify kinetics of the LiFePO₄ particle, which are shown in Equation (2.1.7) and Equation (2.1.8) below:

$$\frac{\partial c}{\partial t} = D\nabla^2 c, \quad (2.1.7)$$

where c is the concentration of oxidized or reduced species, D is the bulk diffusivity, ∇^2 is the Laplacian operator, and t is time. To solve Equation (2.1.7), we need one initial condition and two boundary conditions. The initial condition is $c_o(t=0) = c_o^*$ with $c_r(t=0) = 0$, where c_o is the concentration of the oxidized species, c_o^* is the maximum concentration of the oxidized species, c_r is the concentration of the reduced species. We use the semi-infinite boundary condition as the 1st boundary condition of Equation (2.1.7) since the thickness of the diffusion layer during CV scans is assumed to be very small relative to the size of the whole particle. The 2nd boundary condition is given by Equation (2.1.8) below,

$$\frac{i}{F} = -D\nabla c_r, \quad (2.1.8)$$

where i is the electric current density on the particle surface and F is the Faraday's constant.

The current density of a LiFePO₄ particle is controlled by chemical kinetics on the particle surface, which involves the mechanical stress resulted from dislocations and the electrical potential of the particle. We adopt the modified Butler-Volmer equation [42] shown below for the current density i in Equation (2.1.8):

$$i = i_0 \left\{ \frac{c_o(0,t)}{c_o^*} \exp\left(-\alpha \frac{F\Delta\phi - \sigma_{hAVG}\Omega}{RT}\right) - \frac{c_R(0,t)}{c_R^*} \exp\left[(1-\alpha) \frac{F\Delta\phi - \sigma_{hAVG}\Omega}{RT}\right] \right\}, \quad (2.1.9)$$

with $i_0 = -Fk_0$, where i_0 is the exchange current density, k_0 is the reference pre-exponential factor, $c_o(0,t)$ is the concentration of the oxidized species on the particle surface, $c_R(0,t)$ is the concentration of the reduced species on the particle surface, c_R^* is the maximum concentration of the reduced species, α is the symmetry factor in chemical kinetics, σ_{hAVG} is the average hydrostatic stress of the particle, R is the gas constant, T is temperature, and Ω is the partial molar volume of Li^+ in the particle, which is assumed to be a linear function of the molar fraction of occupied Li^+ sites as shown below,

$$\Omega = \Omega_{AVG} \left[2k \left(y_{Li} - \frac{1}{2} \right) + 1 \right], \quad (2.1.10)$$

where Ω_{AVG} is the average partial molar volume of Li^+ , k is a material property (i.e., fraction coefficient), and y_{Li} is the molar fraction of occupied Li^+ sites. In the modified Butler-Volmer equation (Equation (2.1.9)), Ω is calculated using the value of y_{Li} on the particle surface governed by Equation (2.1.7) and Equation (2.1.8), σ_{hAVG} is the mean of the hydrostatic stress σ_h over the 2-D particle model, with $\sigma_h = \frac{1}{3}(\sigma_{xx} + \sigma_{yy} + \sigma_{zz})$, where σ_{xx} , σ_{yy} , and σ_{zz} are stress components calculated using Equation (2.1.1), with x , y , and z corresponding to the indices 1, 2, and 3, respectively.

The kinetic performance of a LiFePO_4 particle can be revealed by a single variable, named effective diffusivity, which represents the combined performance of the Li^+ diffusion in the particle and the electrochemical reaction on the particle surface. We use the Randles-Sevcik

equation [106] shown below to calculate the effective diffusivity of the particle containing different dislocation groups:

$$i_p = 0.4463 F c_o^* \left(\frac{F v D_{RS}}{RT} \right)^{\frac{1}{2}}, \quad (2.1.11)$$

where i_p is the peak current density and D_{RS} is the effective diffusivity.

2.1.3 Algorithm and parameters

The simulation algorithm coded with MATLAB includes nine steps as follows: (1) We solve Equations (2.1.4), (2.1.5) and (2.1.6) to obtain the numerical auxiliary angle functions $\omega(\Psi)$, $\eta_x(\Psi)$, and $\eta_y(\Psi)$. (2) After discretizing the 2-D particle model, the stress components of all grid nodes are calculated using Equation (2.1.1) for each dislocation. (3) We calculate the angles between the radius vectors of all grid nodes and the Burgers vectors of dislocations, and then calculate the auxiliary angles of all grid nodes using the interpolation method with the numerical functions $\omega(\Psi)$, $\eta_x(\Psi)$, and $\eta_y(\Psi)$. (4) For each dislocation, the displacement components of all grid nodes are obtained by substituting the auxiliary angles from step (3) into Equations (2.1.2) and (2.1.3). (5) We sum the stresses and displacements induced by all dislocations in the particle model. (6) By repeating steps (2) to (5), the average hydrostatic stresses at different phase fractions are calculated for all dislocation groups. (7) We calculate the numerical relations between σ_{hAVG} and $\Delta\phi$ for all dislocation groups using the interpolation method with the relation between x_p and $\Delta\phi$ mentioned in Section 2.1.2. (8) Based on the numerical functions $\sigma_{hAVG}(\Delta\phi)$, we use the finite difference method shown in Bard and Faulkner [107] to solve Equations (2.1.7), (2.1.8), (2.1.9), and (2.1.10), and then obtain the

electric current densities for all scan rates and all dislocation groups. (9) We substitute the peak current densities from step (8) into the Randles-Sevcik equation (Equation (2.1.11)) to solve the effective diffusivities D_{RS} for all dislocation groups.

In Equations (2.1.1), (2.1.2), and (2.1.3), the strategy of adapting phase fraction-dependent anisotropic materials of LiFePO_4 are obtained from Kim and Huang [19] and ChiuHuang and Huang [99] [100]. Other parameters used for the simulation are listed in Table 2.1. For different distribution of dislocations at different scan rates, the ranges of Li^+ fraction for two-phase coexistence during scans should be different. It is necessary to assign the range of Li^+ fraction for one case of simulation to fit the material parameters in the modified Butler-Volmer equation and the partial molar volume of Li^+ in the particle (i.e., Equations (2.1.9) and (2.1.10)). According to the open-circuit voltage of LiFePO_4 shown in Yamada et al. [108], the range of the molar fraction of occupied Li^+ sites for two-phase coexistence during the quasi-equilibrium process is $0.05 < y_{Li} < 0.89$. That is, Li-ion molar fraction $y_{Li} = 0.05$ when phase fraction $x_p = 0$, and Li-ion molar fraction $y_{Li} = 0.89$ when phase fraction $x_p = 1$. We select this range and the dislocations of group D/orientation-3 (-1, 0) with $v = 0.65$ mV/s as the conditions of fitting the material parameters k_0 in the modified Butler-Volmer equation (Equation (2.1.9)), Ω_{AVG} and k in the equation of partial molar volume of Li^+ (Equation (2.1.10)).

Table 2.1 Material parameters used for the simulation.

#Estimated value based on the results in Maxisch and Ceder [12]. ‡Estimated value based on the results in Churikov et al. [109]. †Estimated value fit to the results in Yamada et al. [108].

Parameter	Unit	Value	Parameter	Unit	Value
c_O^*	mol / m^3	1×10^6 #	k_0	$mol \cdot m^{-2} \cdot s^{-1}$	1×10^{-8} †
c_R^*	mol / m^3	1×10^6 #	T	K	298.15
D	m^2 / s	1×10^{-17} ‡	k	-	0.848 †
α	-	0.5	Ω_{AVG}	m^3 / mol	1.5×10^{-5} †

2.2 Results and Discussion

Figure 2.1 displays the stress and displacement fields of the LiFePO_4 particle model with different dislocation densities, where dislocation#1 with orientation-1 $(1, 0)$ and the phase fraction $x_p = 0.9$ of the particle. Group A includes dislocation#1 and dislocation#2. Group B contains dislocation#1, 2, and 3. Group C has dislocation#1, 2, 3, and 4. Group D includes all five dislocations. The Burgers vectors of dislocation#1, 2, 3, 4, and 5 in Figure 2.1 are $(1, 0)$, $(1, 0)$, $(-1, 0)$, $(1, 0)$, and $(-1, 0)$, respectively. As the directions of the Burgers vectors of all dislocations are $(1, 0)$ or $(-1, 0)$, only u_x shows the sharp interfaces which presents the location of slip planes of dislocations.

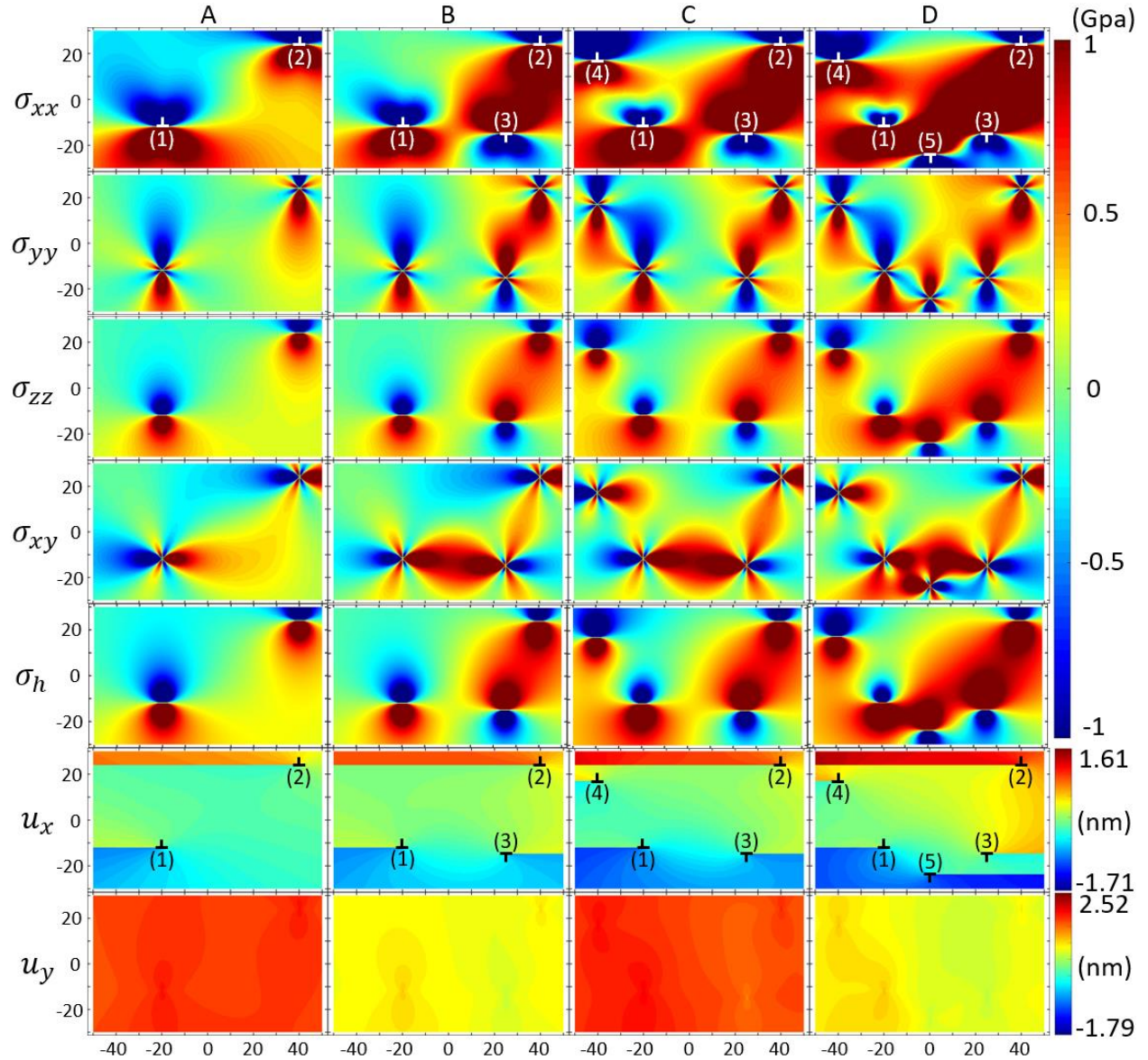


Figure 2.1 Stress fields and displacement fields of a Li_YFePO_4 particle for different dislocation densities when dislocation#1 with orientation-1 and phase fraction $x_p = 0.9$. Group A has dislocation#1 and 2. Group B has dislocation#1, 2, and 3. Group C has dislocation#1, 2, 3, and 4. Group D has dislocation#1, 2, 3, 4, and 5. The Burgers vectors of dislocation#1, 2, 3, 4, and 5 are $(1, 0)$, $(1, 0)$, $(-1, 0)$, $(1, 0)$, and $(-1, 0)$ respectively. With a higher dislocation density, the larger average value of hydrostatic stress $\sigma_h = (\sigma_{xx} + \sigma_{yy} + \sigma_{zz}) / 3$ suggests a higher electrical potential of the particle. The sharp interfaces in displacement fields indicate where the slip planes of dislocations are located.

Figure 2.2 shows the stress and displacement fields when the Burgers vector of dislocation#1 is (0, -0.6) (orientation-2). The phase fraction and the arrangements of dislocation#2, 3, 4, 5 in Figure 2.2 are the same as those in Figure 2.1, for easy comparison to demonstrate the effects of dislocation orientation. The slip plane of dislocation#1 with orientation-2 (0, -0.6) is presented by the corresponding sharp interface of u_y in Figure 2.2. The stress and displacement fields of the particle for orientation-3 (-1, 0) of dislocation#1 are shown in Figure 2.3, in which the phase fraction and the arrangements of dislocation#2, 3, 4, 5 are the same as those in Figure 2.1 and Figure 2.2. The sharp interface of u_x around dislocation#1 in Figure 2.3 indicates the slip plane of dislocation#1 with orientation-3 (-1, 0).

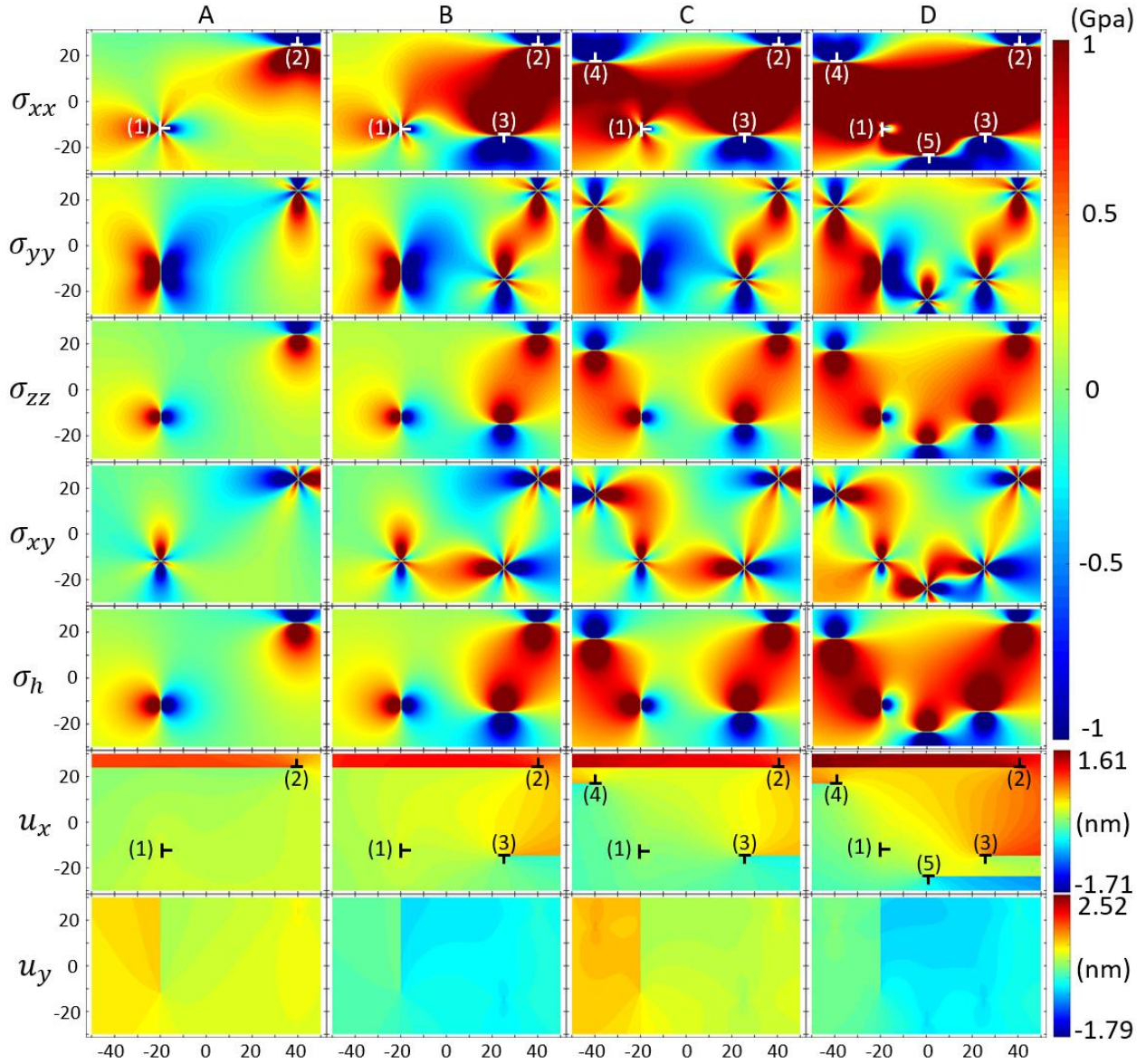


Figure 2.2 Stress fields and displacement fields of a Li_yFePO_4 particle for different dislocation densities when dislocation#1 with orientation-2 and phase fraction $x_p = 0.9$. Group A has dislocation#1 and 2. Group B has dislocation#1, 2, and 3. Group C has dislocation#1, 2, 3, and 4. Group D has dislocation#1, 2, 3, 4, and 5. The Burgers vectors of dislocation#1, 2, 3, 4, and 5 are $(0, -0.6)$, $(1, 0)$, $(-1, 0)$, $(1, 0)$, and $(-1, 0)$ respectively. With a higher dislocation density, the larger average value of hydrostatic stress $\sigma_h = (\sigma_{xx} + \sigma_{yy} + \sigma_{zz})/3$ suggests a higher electrical potential of the particle. The sharp interfaces in displacement fields indicate where the slip planes of dislocations are located.

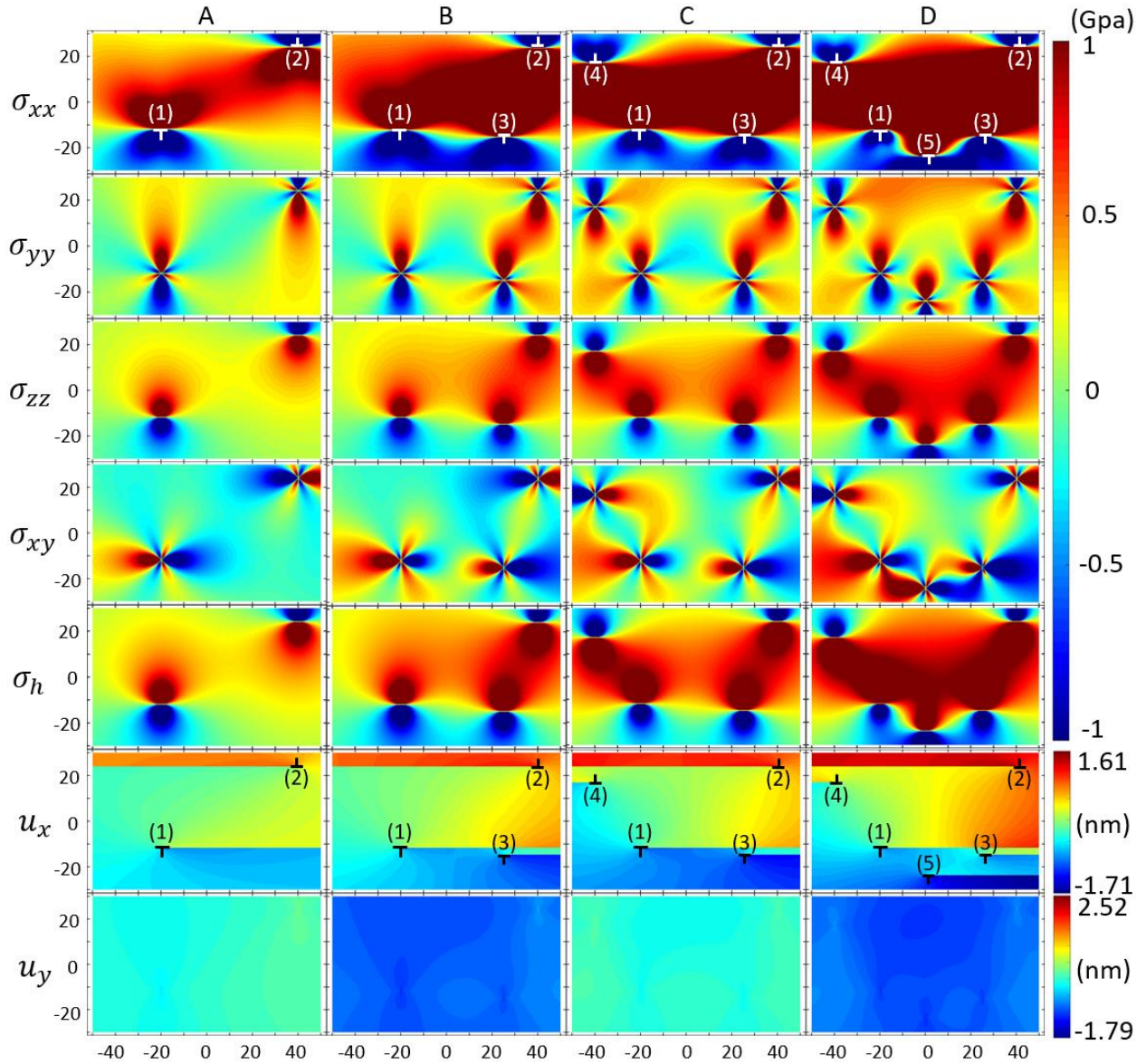


Figure 2.3 Stress fields and displacement fields of a Li_YFePO_4 particle for different dislocation densities when dislocation#1 with orientation-3 and phase fraction $x_p = 0.9$. Group A has dislocation#1 and 2. Group B has dislocation#1, 2, and 3. Group C has dislocation#1, 2, 3, and 4. Group D has dislocation#1, 2, 3, 4, and 5. The Burgers vectors of dislocation#1, 2, 3, 4, and 5 are $(-1, 0)$, $(1, 0)$, $(-1, 0)$, $(1, 0)$, and $(-1, 0)$ respectively. With a higher dislocation density, the larger average value of hydrostatic stress $\sigma_h = (\sigma_{xx} + \sigma_{yy} + \sigma_{zz}) / 3$ suggests a higher electrical potential of the particle. The sharp interfaces in displacement fields indicate where the slip planes of dislocations are located.

In Figure 2.1, Figure 2.2, and Figure 2.3, from group A to group D, the average values of σ_{xx} , σ_{yy} , and σ_{zz} increase for all orientations of dislocation#1, which indicates a larger average hydrostatic stress for a higher dislocation density. Hence, using the modified Butler-Volmer equation (Equation (2.1.9)) yields that increasing the dislocation density may enhance the electrical potential of LiFePO₄ cathodes. The sharp interfaces (i.e., lattice slip planes) in displacement fields in Figure 2.1, Figure 2.2, and Figure 2.3 reveal the dislocation-induced plastic deformation of the particle, where the existence of lattice slip plane is the key indicator of discrete plastic deformation at the interface. Of note, the total plastic strain of a crystal particle can be the accumulation of discrete dislocation plasticity from multiple dislocations. With the increased dislocation density, differences between the maximum and minimum displacement fields are observed, indicating enlarged average plastic strains for all orientations of dislocation#1 (Figure 2.1, Figure 2.2, and Figure 2.3).

By comparing Figure 2.1, Figure 2.2, and Figure 2.3, we observe the effect of different dislocation slip directions, i.e., the dislocation orientation, on stress fields. As shown in Equation (2.1.1), the stress induced by each dislocation core is influenced by the dislocation orientation. The average stress of a particle is hence different for different dislocation orientations. For each dislocation density, the orientation-3 (-1, 0) (Figure 2.3) exhibits the highest average values of σ_{xx} , σ_{yy} , σ_{zz} , and hydrostatic stress σ_h of the particle. Based on the modified Butler-Volmer equation (Equation (2.1.9)), we thus deduce that the particle with orientation-3 (-1, 0) for dislocation#1 exhibits the highest electrical potential in CV scans.

The detailed influence of the dislocation orientation on the electrochemical performance of the LiFePO₄ particle model is revealed by CV curves for different dislocation densities in Figure 2.4, where the scan rate of each CV curve is 16 mV/s. In the gray region (-90.849 mV <

$\Delta\varphi < 90.849$ mV) in Figure 2.4, the LiFePO_4 particle shows two-phase coexistence. The stiffness coefficients of the particle during two-phase coexistence depend on the phase fraction x_p that is assumed to change linearly from 0 to 1 when $\Delta\varphi$ decrease from 90.849 mV to -90.849 mV. For every orientation of dislocation#1, the CV curve with a higher dislocation density shows a larger shift and stronger distortion relative to the CV curve with no dislocation. This comparison indicates that the dislocation density may help LiFePO_4 provide larger electrical power, suggesting better kinetic performance. By comparing Figure 2.4a-c, we observe the extents of the dislocation-induced shift and distortion of a CV curve relate to the dislocation orientation. For every dislocation density, the CV curve with orientation-3 (-1, 0) for dislocation#1 exhibits the highest electrical potential, and the CV curve with orientation-1 (1, 0) for dislocation#1 shows the weakest shift and distortion. We may hence promote the kinetic performance of LiFePO_4 cathode materials by increasing the density and tailoring the orientations of dislocations.

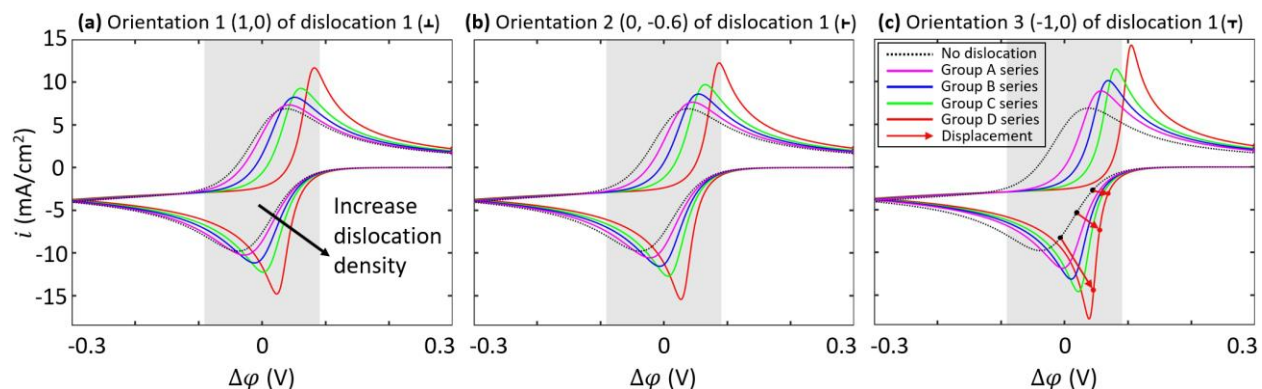


Figure 2.4 CV curves for different dislocation densities of a Li_YFePO_4 particle, where dislocation#1 with **(a)** orientation-1 (1, 0), **(b)** orientation-2 (0, -0.6), and **(c)** orientation-3 (-1, 0). The scan rate of every CV curve is 16 mV/s. The gray region indicates the overpotential of two-phase coexistence ($0 < x_p < 1$). From group A to group D, the dislocation density increases. For every orientation of dislocation#1, the CV curve with a higher dislocation density shows a larger displacement relative to the CV curve with no dislocation. The displacement of CV curves consists of shift and distortion, which depend on the density and orientation of dislocations. For each dislocation density, orientation-3 (-1, 0) displays the strongest shift and distortion, and orientation-1 (1, 0) shows the weakest shift and distortion. The kinetic performance of electrodes may hence be promoted by increasing the dislocation density and adjusting the orientations of dislocations.

To illustrate the effects of scanning rates, the influences of the density and orientation of dislocations on CV curves are presented in Figure 2.5, where the scanning direction and the overpotential range of two-phase coexistence (the gray region) are the same as those in Figure 2.4. Both the orientation of dislocation#1 and the dislocation density of the particle influence the peak current density (i.e., the peak value of i) and the peak overpotential (i.e., the value of $\Delta\phi$ corresponds to the peak current density) of CV curves. For each scan rate ν in Figure 2.5, the CV curve in group D (i.e., contains the greatest number of dislocation density) with orientation-3 (-1, 0) displays the highest peak current density and peak overpotential (Figure 2.5I). Based on the Randles-Sevcik equation (Equation (2.1.11)), the highest peak current density indicates the highest effective diffusivity, which implies that the effective diffusivity of a LiFePO₄ particle may be increased by adjusting the characteristics of dislocations. With a higher scanning rate, dislocations have stronger effects on determining the peak current density and peak overpotential. By comparing the CV curves of group A with orientation-1 (1, 0) (Figure 2.5a) with the CV curves of group D with orientation-3 (-1, 0) in Figure 2.5I, we can see that (1) the peak current densities during delithiation increase from 1.267 mA/cm² to 2.164 mA/cm² (1.708 times) for $\nu = 1$ mV/s, and from 7.325 mA/cm² to 14.258 mA/cm² (1.946 times) for $\nu = 16$ mV/s, and (2) the corresponding peak overpotential increase from 0.038 mV to 0.08 mV (2.105 times) for $\nu = 1$ mV/s, and from 0.042 mV to 0.106 mV (2.524 times) for $\nu = 16$ mV/s. This result indicates that the dislocation-promoted electrical power is larger for a higher scanning rate. Because a larger scanning rate represents a stronger non-equilibrium state of the particle, the electrochemical performance of LiFePO₄ (dis)charged with a higher C-rate (i.e., under a stronger non-equilibrium state) may be enhanced by the existence of dislocations.

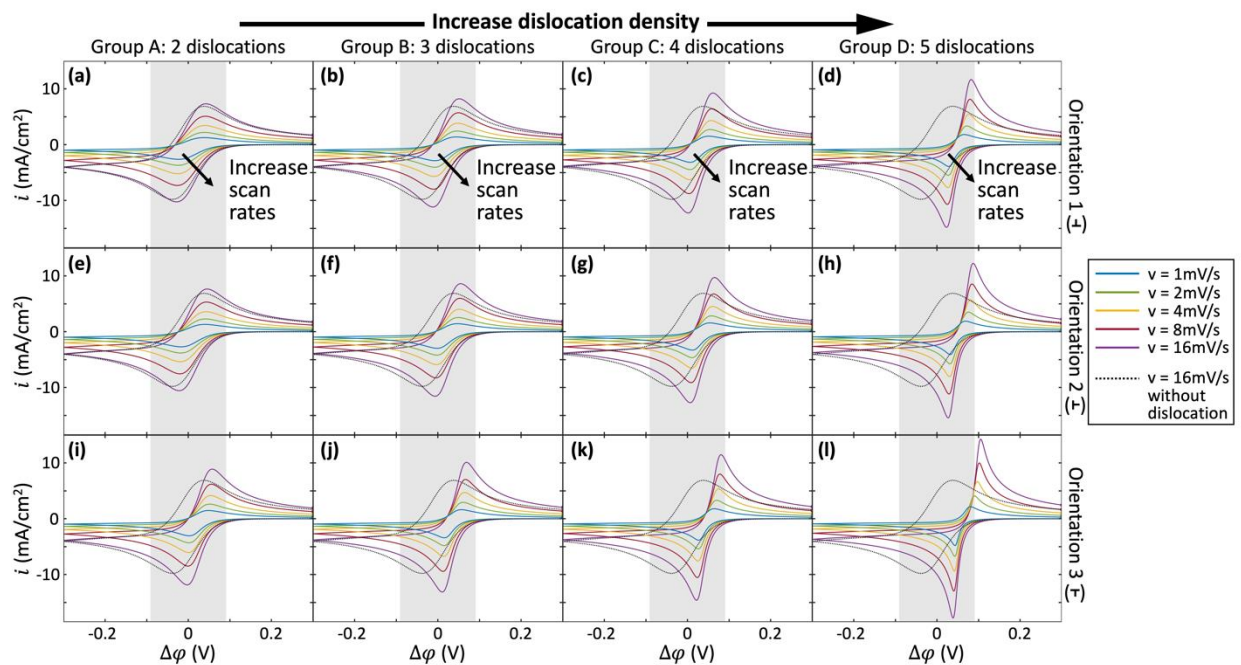


Figure 2.5 CV curves of a Li_yFePO_4 particle for different scan rates with different orientations of dislocation#1 and different dislocation densities. The gray region indicates the overpotential of two-phase coexistence ($0 < x_p < 1$). From group A to group D, the dislocation density increases. For every scan rate (v), the peak current density (the peak value of i) and peak overpotential ($\Delta\phi$ corresponding to the peak current density) of CV curves depend on both the orientation of dislocation#1 and the dislocation density of the particle. The CV curves in group D with orientation-3 (-1, 0) (Figure 2.5l) display the highest peak current density and peak overpotential for all scan rates, which implies the highest effective diffusivity of Li^+ and the largest electrical power. With a higher scan rate, dislocations have stronger effects on increasing the peak current density and peak overpotential, which suggests that the kinetic performance of the particle with a stronger non-equilibrium state may be promoted more by adjusting dislocations.

The average value of the hydrostatic stress, σ_{hAVG} in the modified Butler-Volmer equation (Equation (2.1.9)) is the key parameter connecting effects of dislocations and electrochemical performance for a LiFePO₄ particle. With the increased dislocation density, the change of the average hydrostatic stress, $\Delta\sigma_{hAVG}$, between different dislocation groups is presented in Figure 2.6a. $\Delta\sigma_{hAVG}$ is shown to be larger than zero for every dislocation density, indicating the particle is in tension due to dislocations for both Li-rich phase (denote in *) and Li-poor phase (denote in □). The modified Butler-Volmer equation (Equation (2.1.9)) suggests that $\Delta\sigma_{hAVG} > 0$ leads to the increase of electrical potential for the same current density, as shown in Figure 2.4 and Figure 2.5, which also increases electrical power. A varied $\Delta\sigma_{hAVG}$ value in Figure 2.6a suggests a nonlinear relation between the stress and dislocation density for the particle. By increasing the dislocation density is not sufficient to increase σ_{hAVG} , because $\Delta\sigma_{hAVG}$ is determined by both the location and the orientation of any additional dislocation, which is noticeable by comparing Figure 2.1, Figure 2.2, and Figure 2.3. Tailoring these characteristics of dislocations is essential for promoting the kinetic performance of a LiFePO₄ particle.

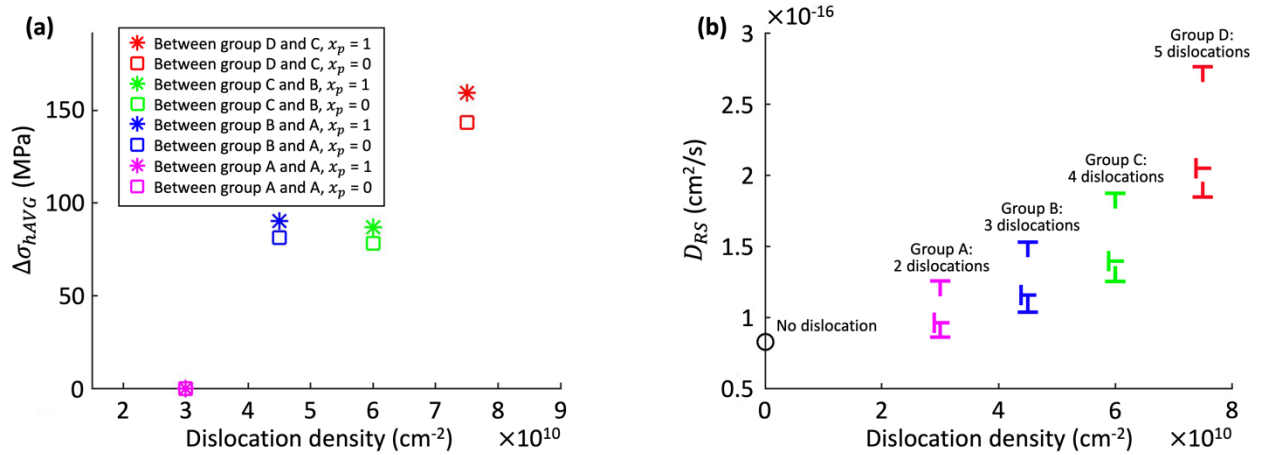


Figure 2.6 (a) $\Delta\sigma_{hAVG}$, the change of the average hydrostatic stress of a Li_yFePO_4 particle when the dislocation density increases, with phase fraction $x_p = 0$ and $x_p = 1$. $\Delta\sigma_{hAVG} > 0$ indicates that dislocations may help Li_yFePO_4 be in tension. The nonconstant $\Delta\sigma_{hAVG}$ shows the nonlinear relation between the stress and dislocation density. The difference of $\Delta\sigma_{hAVG}$ between $x_p = 0$ and $x_p = 1$ induced by the phase transformation suggests the different effects of dislocations for different states of charge (SOCs). **(b)** D_{RS} , the effective diffusivities calculated by the Randles-Sevcik equation [107] for different dislocation densities with different orientations of dislocation#1. The particle with a larger dislocation density has a higher D_{RS} , especially for orientation-3 (-1, 0), which implies that increasing the dislocation density and adjusting the dislocation orientation may promote the kinetic performance of the electrodes in lithium-ion batteries.

Because of the different stiffness coefficients between the Li-rich phase (denote in $*$) and the Li-poor phase (denote in \square), the $\Delta\sigma_{hAVG}$ with $x_p = 1$ is observed higher than the $\Delta\sigma_{hAVG}$ with $x_p = 0$ for every dislocation density in Figure 2.6a. Based on the modified Butler-Volmer equation (Equation (2.1.9)), the electrical potential of a discharged LiFePO₄ particle is hence increased more by the existence of dislocations than that of a charged particle. Therefore, among the particles with the same initial and final electrical potentials during (dis)charging, the particle with dislocations may have larger change of SOC than the particle without dislocations. This mechanism suggests that adding dislocations may help LiFePO₄ cathode materials mitigating the capacity loss during (dis)charging. Figure 2.6a shows that the difference of $\Delta\sigma_{hAVG}$ between $x_p = 1$ and $x_p = 0$ is larger when the $\Delta\sigma_{hAVG}$ of $x_p = 0$ is larger, which suggests that a larger $\Delta\sigma_{hAVG}$ from additional dislocations may increase the capacity. Thus, the increase of capacity could be achieved by carefully adding dislocations.

The dislocation-affected electrochemical performance of a LiFePO₄ particle can be reflected by the increased effective diffusivity as shown in Figure 2.6b. With the peak current densities during lithiation at different scan rates (Figure 2.5), the effective diffusivity D_{RS} of Li⁺ is calculated using the Randles-Sevcik equation (i.e., Equation (2.1.11)). D_{RS} is a parameter that reveals the combined effects of the bulk diffusivity D of Li⁺ in the particle and the rate of the chemical reaction on the particle surface. A larger D_{RS} represents a faster (de)lithiation. Figure 2.6b shows that D_{RS} is higher for a particle with higher dislocation density; and the increase rate of D_{RS} depends on the orientation of dislocation#1 and the dislocation density of the particle. For group D with orientation-3 (-1, 0), $D_{RS} = 2.72 \times 10^{-16}$ cm²/s, which is 3.3 times larger as

compared with D_{RS} for no dislocation ($0.826 \times 10^{-16} \text{ cm}^2/\text{s}$). Hence, we may improve the effective diffusivity of LiFePO_4 cathodes by introducing dislocations with increased density and carefully chosen orientation. In the observation of Singer et al. [34], the dislocation density was larger for a higher voltage of the cathode VS Li^+ (a higher SOC). Although what they measured were Li-rich layered oxides, we may expect that the LiFePO_4 cathode with a higher SOC has a larger effective diffusivity, once the orientations of dislocations are justified.

Besides the increased density and carefully chosen orientations of dislocations, the variational partial molar volume of Li^+ is also a key factor of the increased effective diffusivity in Figure 2.6b. This relation can be qualitatively interpreted by following steps: (1) The area under a CV curve between the minimal overpotential $\Delta\varphi_{MIN}$ and the maximal overpotential $\Delta\varphi_{MAX}$ during the 1st half scan is denoted by A , which is determined by the discharged electric charge quantity because of the equality below:

$$A = \int_{\Delta\varphi_{MAX}}^{\Delta\varphi_{MIN}} id\Delta\varphi = \int_{t_1}^{t_2} ivdt = v \int_{t_1}^{t_2} idt = vQ,$$

where t_1 and t_2 are the initial and final time of the 1st half CV scan respectively; and Q is the discharged electric charge quantity. (2) As discussed above, dislocations may increase the capacity during (dis)charging. For the same scanning rate with the orientation of dislocation#1, the particle has more dislocations may thus be discharged with more electricity during the 1st half scan, suggesting that the absolute value of A for the CV curve should be equal to or larger than that for the CV curve of a particle with lesser dislocations. It is consistent with the CV curves observed in Figure 2.4 and Figure 2.5. (3) The CV curves with dislocations can be considered as being transformed from one with no dislocation. The transformation can be characterized by the displacement of CV curves relative to the one with no dislocation in the coordinate system,

which is shown in Figure 2.4c. The displacement of CV curves consists of a shift and a distortion which indicate rigid movement and shape changes, respectively. (4) The CV curves are generated based on Fick's law (Equation (2.1.7)), whose boundary conditions include the modified Butler-Volmer equation (Equation (2.1.9)). Mathematically, the term $\sigma_{hAVG}\Omega$ in Equation (2.1.9) represents the horizontal shift of CV curves in the CV coordinate system. If $\sigma_{hAVG}\Omega$ is a constant value during scanning, the displacement of CV curves is horizontal and evenly distributed, as shown in Dhiman and Huang [42]. In this case, the CV curves for particles with different characteristics of dislocations should have the same shape at different horizontal locations in the CV coordinate system, and then the corresponding peak current densities of CV curves are all the same. (5) For variational Ω expressed by the molar fraction of Li^+ (Equation (2.1.10)), $\sigma_{hAVG}\Omega$ increases with the increased y_{Li} during scanning, suggesting that the distances of the horizontal shift of CV curves are smaller at the beginning of scans when y_{Li} value is small. With a variational horizontal shift, to keep the absolute value of area A for the CV curve equal to or larger than that for the one for particles without dislocations, the CV curve for particles with dislocations would be distorted. In this case, the curves are no longer horizontally shifting with the same distance at different locations in the CV coordinate system. That is, distortion is introduced to compensate the effects of variational $\sigma_{hAVG}\Omega$, as shown in Figure 2.4c. (6) For a bigger σ_{hAVG} value, $\sigma_{hAVG}\Omega$ has a larger variation, and it indicates a stronger distortion. This result explains that the particle with more dislocations exhibits a larger absolute value of the peak current density in the 1st half CV scan, as shown in Figure 2.4 and Figure 2.5. (7) The peak current density in the 1st half scan is used for calculating the effective diffusivity in the Randles-

Sevcik equation (i.e., Equation (2.1.11)). Based on a variational Ω , the particle with a larger σ_{hAVG} value is therefore has a higher effective diffusivity D_{RS} as displayed in Figure 2.6b.

As shown in Figure 2.4 and Figure 2.5, the CV curves for particles have more dislocations has stronger distortion, which makes the part of the curve of the 1st half scan closer to the part of the curve of the 2nd half scan. Mathematically, there should be intersections in a CV curve if the term $\sigma_{hAVG}\Omega$ in Equation (2.1.9) is large enough. However, for LiFePO₄ cathodes, the CV curve with intersections has not been observed yet in experiments. Due to the limited effective diffusivities, it might confine the influence of dislocations on peak current density. Dislocation-induced distortions of CV curves may hence be spontaneously restricted to avoid the intersections, which mitigate dislocation effects.

Compared to the CV curves with the constant partial molar volume shown in Dhiman and Huang [42], the CV curves in this study are distorted due to the variational partial molar volume, as discussed above, suggesting that using carefully tailored dislocations to promote the effective diffusivity of lithium is suitable for the electrodes whose partial molar volumes are functions of the SOC or Li⁺ concentration. The variational partial molar volume may also be revealed under nonequilibrium state. Due to the solid viscosity during the nonequilibrium process, the volume change of electrodes may be delayed relative to the fraction change of Li⁺, which has been shown in the experimental study of Liu et al. [110] and modeling study of Chen and Huang [9]. The delay indicates that the effective partial molar volume is variational during (de)lithiation, even if the intrinsic partial molar volume is constant. The increase of the effective diffusivity is more noticeable for the electrode under a stronger non-equilibrium process, as mentioned above. To include the electrochemical polarization in the non-equilibrium process, the extent of two-phase coexistence in CV spectra (the gray zone in Figure 2.4 and Figure 2.5) in this study is

wider than that in Dhiman and Huang [42], which makes the stiffness change induced by the phase transformation becoming more gradual. In contrast, the sharper change of stiffness in the narrower extent of two-phase coexistence in Dhiman and Huang [42] led to small fluctuations of CV curves in the two-phase coexistence regions (cf. Figure 4 and Figure 5 in Dhiman and Huang [42]).

The dislocation density and dislocation-induced stress in most existing studies were formulated using below equations [111],

$$\rho = \frac{\beta}{b} \frac{\partial c}{\partial r}, \quad (2.2.1)$$

$$\sigma_d = M \chi \mu b \sqrt{\rho}, \quad (2.2.2)$$

where ρ is the dislocation density, β is lattice contraction coefficient, b is the magnitude of the Burgers vector, $\partial c / \partial r$ is the concentration gradient, σ_d is the dislocation-induced stress, M is the Taylor orientation factor, χ is the empirical constant, and μ is the shear modulus. For example, Ma et al. [112] modeled the composition of ρ for dislocation-induced softening effect and incorporated σ_d in the plastic constitutive model of electrodes [113], which based on an assumption that dislocations should reduce strain energy (i.e., diffusion-induced stress). With this assumption and the traditional dislocation-induced stress model (i.e., Equations (2.2.1) and (2.2.2)), diffusion-induced stress was simulated to be reduced by σ_d in the electrodes with different geometries (Wei et al. [111], Li et al. [114], Liu et al. [30], Li et al. [31], Zhu et al. [32]), which is in contrast to our study about $\Delta\sigma_{hAVG}$ shown in Figure 2.6a. This contrary exists because the above assumption is effective for spontaneously generated dislocations only, rather than pre-existing engineered dislocations investigated in this study. This is the reason why the

dislocations in above contributions [111] [114] [30] [31] [32] were named diffusion-induced misfit dislocations. Unlike the spontaneously generated dislocations, the engineered dislocations have freedom of orientation. Therefore the stress induced by engineered dislocations should be described by Equation (2.1.1) instead of Equations (2.2.1) and (2.2.2). Furthermore, Equations (2.2.1) and (2.2.2) are based on continuous dislocation density field and isotropic material property, which is only valid for large electrode particles and polycrystal. In contrast, our study focuses on nano-sized electrode particles. Compared to large electrode particles, a nanoparticle has lower quantity of dislocations and shows stronger trend of single crystal, therefore should be described by an anisotropic discrete dislocation model (i.e., Equations (2.1.1) to (2.1.6)). The discrete dislocation model in this study reveals the singularity of stress fields at dislocation cores, as shown in Figure 2.1, Figure 2.2, and Figure 2.3, which indicates the influences of the distribution and orientation of dislocations. Although a smaller nanoparticle has less dislocations, the effect of the singularity of each dislocation core is relatively stronger on stress fields. Hence, it is more necessary to consider the discreteness of dislocations for smaller electrode particles.

2.3 Conclusion

Based on linear elastic mechanics and the superposition principle, we have modeled the stress and displacement field induced by the dislocations with arbitrary distribution and orientations in an electrode particle. The dislocation-induced stress is introduced into the electrochemical reaction on the particle surface using the modified Butler-Volmer equation which is a boundary condition of Fick's law used for governing the diffusion of lithium. The phase-fraction dependent anisotropic stiffness of electrode materials is incorporated in this study. The partial molar volume of lithium is considered as a function of the molar fraction of occupied Li^+ sites during (de)lithiation.

We reported the stress and displacement fields of a LiFePO_4 particle model for four groups of dislocations with different dislocation densities. Every group includes a dislocation with a variational dislocation orientation. The CV curves of the particle for all densities and orientations of dislocations under different scanning rates are numerically solved using the finite difference method coded with MATLAB. The peak current densities in the CV curves are utilized into the Randles-Sevcik equation to identify the effective diffusivities of lithium corresponding to different dislocation characteristics. The influences of dislocations on CV curves and the effective diffusivity are compared with that of the electrode particle without dislocations.

Compared to the electrode particle with no dislocations, increasing the dislocation density can add-up the average stress and the average plastic strain of the particle, which leads to higher electrical potential due to the coupling effect between the mechanical stress and the electrochemical reaction. The increased electrical potential indicates the increase of the electrical energy stored in the particle, which can be magnified by optimizing the dislocation orientation.

Increasing the dislocation density makes CV curves shift and distort, especially for a particular dislocation orientation, representing the improvements of electrical power and the effective diffusivity. Electrical power is improved dramatically when the particle is scanned at a higher rate. Thus, justified dislocations may improve the kinetic performance of electrodes, especially when the electrodes are under stronger non-equilibrium states. Based on the difference between the influences of dislocations on the two phases of LiFePO_4 , we infer that the capacity loss of the electrodes during (dis)charging may be alleviated by dislocations, especially for higher dislocation densities at certain dislocation orientations.

This study has demonstrated the influences of the density and orientation of dislocations on the mechanical and electrochemical response of a LiFePO_4 particle, which suggests the strategy of using engineered dislocations to further improve the performance of electrodes for lithium-ion batteries. Our methodology presents an insight to develop dislocation-involved mechanics and electrochemistry for battery systems.

CHAPTER 3

Paths of Energy Change for Electrodes of Lithium-ion Batteries under Non-equilibrium Process

3.1 Modeling Method

3.1.1 Free energy with multi-layered states and path factors

The electrodes of Li-ion batteries can be considered as a system of Li⁺ sites that is partially occupied by Li⁺. The free energy of the system includes the part of structural free energy and the part of entropy induced by Li⁺ fraction change, as shown below

$$a = a_s - Ts, \quad (3.1.1)$$

where, T is temperature, s is entropy, and a_s is the structural free energy that consists of the parts for occupied sites and unoccupied sites as below

$$a_s = a_A y_A + a_B y_B, \quad (3.1.2)$$

where, a_A is the free energy of occupied Li⁺ sites, y_A is the fraction of occupied Li⁺ sites, a_B is the free energy of unoccupied Li⁺ sites, and y_B is the fraction of unoccupied Li⁺ sites, with

$$y_A + y_B = 1. \quad (3.1.3)$$

The free energies for both occupied sites and unoccupied sites depend on the multi-layered states of material's structure and can be expressed as below series of nested equations,

$$a_X = \bar{a}_{X\alpha} f_\alpha^{\text{IV}} + \bar{a}_{X\beta} f_\beta^{\text{IV}} + a_X^{\text{PIV}}, \quad (3.1.4)$$

$$\bar{a}_{XK} = \bar{a}_{XK\alpha} f_\alpha^{\text{III}} + \bar{a}_{XK\beta} f_\beta^{\text{III}} + a_{XK}^{\text{PIII}}, \quad (3.1.5)$$

$$\bar{a}_{XKL} = \bar{a}_{XKL\alpha} f_\alpha^{\text{II}} + \bar{a}_{XKL\beta} f_\beta^{\text{II}} + a_{XKL}^{\text{PII}}, \quad (3.1.6)$$

$$\bar{a}_{XKLM} = \bar{a}_{XKLM\alpha} f_\alpha^{\text{I}} + \bar{a}_{XKLM\beta} f_\beta^{\text{I}} + a_{XKLM}^{\text{PI}}, \quad (3.1.7)$$

$$\bar{a}_{XKLMN} = \bar{a}_{XKLMN}^{\varepsilon} + \bar{a}_{XKLMN}^D + \bar{a}_{XKLMN}^R, \quad (3.1.8)$$

with $X \in \{A, B\}$ and $K, L, M, N \in \{\alpha, \beta\}$, where K, L, M, N are energy indices for different layers, α and β stand for two different states in every layer, f_{α}^{IV} and f_{β}^{IV} , f_{α}^{III} and f_{β}^{III} , f_{α}^{II} and f_{β}^{II} , f_{α}^{I} and f_{β}^{I} are called path factors of states α and β for layers IV, III, II, and I respectively, which control the path of energy change during (de)lithiation. The path factors are determined by a series of order parameters ζ^{χ} of the system and satisfy the identity below

$$f_{\alpha}^{\chi}(\zeta^{\chi}) + f_{\beta}^{\chi}(\zeta^{\chi}) = 1, \quad (3.1.9)$$

with $\chi \in \{\text{I, II, III, IV}\}$. ζ^{χ} is a continuous variable, of which the value change reflects the continuous variation between states α and β for every layer. The physical meaning of the multi-layered states and their corresponding values of ζ^{χ} are listed in Table 3.1. a_X^{PIV} , a_{XK}^{PIII} , a_{XKL}^{PII} , and a_{XKLM}^{PI} are the free energies determined by order parameters ζ^{IV} , ζ^{III} , ζ^{II} , and ζ^{I} respectively. $\bar{a}_{XKLMN}^{\varepsilon}$ is the free energy depending on the deformation of electrodes. \bar{a}_{XKLMN}^D is the free energy influenced by dislocations, and \bar{a}_{XKLMN}^R is the reference free energy of each state.

Table 3.1 Physical meaning of order parameters.

	1 (α)	0 (β)
ζ^I	Li-rich	Li-poor
ζ^{II}	Delithiation	Lithiation
ζ^{III}	Equilibrium	Non-equilibrium
ζ^{IV}	Crystal	Amorphous

The number of layers is generally arbitrary and can be chosen based on the phenomena to be described. In this research, 4 layers' structure have $3 \times 2^5 + 30$ individual energy terms. To decrease the complexity of modeling, we assume below energy relation between α and β states for layer IV,

$$\bar{a}_{X\beta} = r_X^{IV} \bar{a}_{X\alpha} + a_X^{RS} , \quad (3.1.10)$$

where, r_X^{IV} is the relation coefficient between two energies, a_X^{RS} is the reference energy for the relation. Furthermore, some differences between occupied and unoccupied Li^+ sites can be assumed to be neglected for LiFePO_4 and layered oxides, as shown below,

$$r_A^{IV} = r_B^{IV} = r^{IV} , \quad (3.1.11)$$

$$a_A^{RS} = a_B^{RS} = a^{RS} , \quad (3.1.12)$$

$$a_A^{PIV} = a_B^{PIV} = a^{PIV} . \quad (3.1.13)$$

Above assumptions yield below expression for the structural free energy,

$$a_S = \bar{a}_\alpha f_\gamma^{IV} + a^{RS} f_\beta^{IV} + a^{PIV} , \quad (3.1.14)$$

with

$$\bar{a}_\alpha = \bar{a}_{A\alpha} y_A + \bar{a}_{B\alpha} y_B , \quad (3.1.15)$$

and

$$f_\gamma^{IV} = f_\alpha^{IV} + r^{IV} f_\beta^{IV} . \quad (3.1.16)$$

To further simplify the free energy, we set

$$a_{X\alpha}^{PIII} = a^{PIII} , \quad (3.1.17)$$

$$\bar{a}_{X\alpha\alpha\alpha} = \bar{a}_{X\alpha\alpha\beta} = a_{X\alpha} \quad (3.1.18)$$

and

$$a_{X\alpha L}^{PII} = a^{PII} . \quad (3.1.19)$$

Equations (3.1.6), (3.1.18), and (3.1.19) yield

$$\bar{a}_{X\alpha\alpha} = a_{X\alpha} + a^{PII} . \quad (3.1.20)$$

Since the free energy of β state for layer IV is substituted by that of α state using Equation (3.1.10), only notation α is shown for index K in free energy, as shown in Equation (3.1.14).

Hence index K can be deleted to simplify the expression of free energy terms as below,

$$\bar{a}_{X\alpha LMN}^{\varepsilon} = a_{XLMN}^{\varepsilon} , \quad (3.1.21)$$

$$\bar{a}_{X\alpha LMN}^D = a_{XLMN}^D , \quad (3.1.22)$$

$$\bar{a}_{X\alpha LMN}^R = a_{XLMN}^R , \quad (3.1.23)$$

$$\bar{a}_{X\alpha LMN} = a_{XLMN} . \quad (3.1.24)$$

We use square, cubic, and biquadratic polynomial functions shown below to model the path factors and the order parameters determined energies,

$$f^{(2)}(v, v^R) = (v - v^R)^2 , \quad (3.1.25)$$

$$f^{(3)}(v) = -v(2v^2 - 3v) , \quad (3.1.26)$$

$$f^{(4)}(v) = [(v - 1)v]^2 , \quad (3.1.27)$$

where v is an arbitrary variable with reference value v^R . The path factors are cubic with respect to order parameters as below,

$$f_{\alpha}^{\chi}(\zeta^{\chi}) = f^{(3)}(\zeta^{\chi}) , \quad (3.1.28)$$

$$f_{\beta}^{\chi}(\zeta^{\chi}) = 1 - f^{(3)}(\zeta^{\chi}) , \quad (3.1.29)$$

with $\chi \in \{\text{I, II, III, IV}\}$.

The free energy induced by dislocations consists of the strain energy from discrete dislocation cores, which has been studied in Chen et al. [10]. To simplify the modeling formulation, the dislocation-induced strain is considered intrinsic and excluded from the mechanical strain in the modeling formulation in this chapter. The free energy induced by

dislocations are modeled using homogenized dislocation density which includes the information of dislocation orientation. Like the mechanical strain, the dislocation density can affect the fraction of Li^+ , based on the mechanical-electrochemical coupling effect. We model the mechanical strain energy and dislocation induced free energy using the quadratic expression as below,

$$a^\varepsilon(\varepsilon, C, \varepsilon^R) = \frac{1}{2} C \cdot f^{(2)}(\varepsilon, \varepsilon^R) , \quad (3.1.30)$$

$$a^D(Y, H^D, Y^R) = H^D f^{(2)}(Y, Y^R) , \quad (3.1.31)$$

where, ε and Y are characteristic strain and characteristic dislocation density that respectively represent the changes of the mechanical strain and the homogenized dislocation density. In the paragraphs below we omit the adjective ‘‘characteristic’’ for convenience. We use 1-D modeling for simplicity, which does not include the tensor expression. Hence ε and Y are scalars in this study. C and H^D are material coefficients. ε^R and Y^R are reference strain and reference dislocation density. The terms of structural free energy for each state are yielded as below,

$$a_{X\alpha}(\varepsilon, Y) = a^\varepsilon(\varepsilon, C^E, \varepsilon_{X\alpha}^R) + a^D(Y, H_{X\alpha}^D, Y_{X\alpha}^R) + a_{X\alpha}^R , \quad (3.1.32)$$

$$a_{X\alpha}^{PI}(\zeta^1) = H_{X\alpha}^{PI} f^{(2)}(\zeta^1, \zeta_{X\alpha}^{IR}) , \quad (3.1.33)$$

$$a_{X\beta MN}(\varepsilon, Y) = a^\varepsilon(\varepsilon, C^N, \varepsilon_{X\beta MN}^R) + a^D(Y, H_{X\beta MN}^D, Y_{X\beta MN}^R) + a_{X\beta MN}^R , \quad (3.1.34)$$

$$a_{X\beta M}^{PI}(\zeta^1) = H_{X\beta M}^{PI(2)} f^{(2)}(\zeta^1, \zeta_{X\beta M}^{IR}) + H_{X\beta M}^{PI(4)} f^{(4)}(\zeta^1) , \quad (3.1.35)$$

$$a^{P\chi}(\zeta^\chi) = H^{P\chi(2)} f^{(2)}(\zeta^\chi, \zeta^{\chi R}) + H^{P\chi(4)} f^{(4)}(\zeta^\chi) , \quad (3.1.36)$$

with $\chi \in \{\text{II}, \text{III}, \text{IV}\}$, where C^E and C^N are the characteristic stiffness for equilibrium state and non-equilibrium state respectively, $H_{X\alpha}^{PI}$ is the structural parameter with respect to order parameter ζ^1 under equilibrium state. The order parameter determined free energy has square

and biquadratic terms for non-equilibrium state, where $H_{X\beta M}^{PI(2)}$ is the material coefficient for 2nd

power term and $H_{X\beta M}^{PI(4)}$ is for 4th power term. After substitute above free energy terms into

Equation (3.1.1), the total free energy of the system is below,

$$\begin{aligned}
 a(y_A, \varepsilon, Y, \zeta^I, \zeta^{II}, \zeta^{III}, \zeta^{IV}) = & \\
 & \left\{ \left(a_{A\alpha}(\varepsilon, Y) + a_{A\alpha}^{PI}(\zeta^I) \right) f_{\alpha}^{III}(\zeta^{III}) \right. \\
 & \left. + \left[\begin{aligned} & \left(a_{A\beta\alpha}(\varepsilon, Y) f_{\alpha}^I(\zeta^I) + a_{A\beta\alpha}(\varepsilon, Y) f_{\beta}^I(\zeta^I) + a_{A\beta\alpha}^{PI}(\zeta^I) \right) f_{\alpha}^{II}(\zeta^{II}) \\ & + \left(a_{A\beta\beta}(\varepsilon, Y) f_{\alpha}^I(\zeta^I) + a_{A\beta\beta}(\varepsilon, Y) f_{\beta}^I(\zeta^I) + a_{A\beta\beta}^{PI}(\zeta^I) \right) f_{\beta}^{II}(\zeta^{II}) \end{aligned} \right] f_{\beta}^{III}(\zeta^{III}) \right\} y_A \\
 & \left. + \left\{ \begin{aligned} & \left(a_{B\alpha}(\varepsilon, Y) + a_{B\alpha}^{PI}(\zeta^I) \right) f_{\alpha}^{III}(\zeta^{III}) \\ & + \left[\begin{aligned} & \left(a_{B\beta\alpha}(\varepsilon, Y) f_{\alpha}^I(\zeta^I) + a_{B\beta\alpha}(\varepsilon, Y) f_{\beta}^I(\zeta^I) + a_{B\beta\alpha}^{PI}(\zeta^I) \right) f_{\alpha}^{II}(\zeta^{II}) \\ & + \left(a_{B\beta\beta}(\varepsilon, Y) f_{\alpha}^I(\zeta^I) + a_{B\beta\beta}(\varepsilon, Y) f_{\beta}^I(\zeta^I) + a_{B\beta\beta}^{PI}(\zeta^I) \right) f_{\beta}^{II}(\zeta^{II}) \end{aligned} \right] f_{\beta}^{III}(\zeta^{III}) \end{aligned} \right\} y_B \right\} f_{\gamma}^{IV}(\zeta^{IV}) \\
 & + a^{RS} f_{\beta}^{IV}(\zeta^{IV}) + a^{PIV}(\zeta^{IV}) - Ts(y_A)
 \end{aligned} \tag{3.1.37}$$

where, the entropy term is $s(y_A) = -R(y_A \ln y_A + y_B \ln y_B)$, with gas constant R .

3.1.2 Governing equations for the kinetics of main parameters

The free energy function (Equation(3.1.37)) includes 7 independent variables, which is called main parameters describing the electrode system. Based on non-equilibrium thermodynamics [115][116][9], the driving force for the evolution of each main parameter is the partial derivative of free energy with respect to the corresponding main parameter, as listed below,

$$\mu_A = \frac{\partial a}{\partial y_A} - K_A \nabla^2 y_A, \tag{3.1.38}$$

$$\sigma = \frac{\partial a}{\partial \varepsilon} , \quad (3.1.39)$$

$$\mu_Y = \frac{\partial a}{\partial Y} , \quad (3.1.40)$$

$$\Phi^\chi = \frac{\partial a}{\partial \zeta^\chi} - K_\chi \nabla^2 \zeta^\chi , \quad (3.1.41)$$

where, μ_A is the chemical potential of Li^+ , σ is characteristic stress, μ_Y is the chemical potential of dislocations, Φ^χ is the potential of order parameter ζ^χ , K_A and K_χ are the phase field coefficients for Li^+ fraction and order parameter ζ^χ , and ∇^2 is the Laplacian operator. The kinetic equation for each main parameter is given by,

$$c_A \frac{\partial y_A}{\partial t} + \nabla \cdot J_A = 0 , \quad (3.1.42)$$

$$\frac{\partial \varepsilon}{\partial t} = -L_\varepsilon \sigma , \quad (3.1.43)$$

$$\frac{\partial \zeta^\chi}{\partial t} = -L_\chi \Phi^\chi , \quad (3.1.44)$$

$$J_A = -L_A f_A^L(y_A) \left\{ \exp(-\alpha^L A^L(\zeta^\chi) \nabla \mu_A) - \exp[-(\alpha^L + 1) A^L(\zeta^\chi) \nabla \mu_A] \right\} , \quad (3.1.45)$$

with $f_A^L(y_A) = y_A(1 - y_A) , \quad (3.1.46)$

and $A^L(\zeta^\Pi) = A_\alpha^L f_\alpha^\Pi(\zeta^\Pi) + A_\beta^L f_\beta^\Pi(\zeta^\Pi) , \quad (3.1.47)$

$$c_Y \frac{\partial Y}{\partial t} + \nabla \cdot J_Y = 0 , \quad (3.1.48)$$

$$J_Y = -L_Y f_Y^L(\zeta^{\text{IV}}) \nabla \mu_Y , \quad (3.1.49)$$

with $f_Y^L(\zeta^{\text{IV}}) = R_{Y\alpha}^L f_\alpha^{\text{IV}}(\zeta^{\text{IV}}) + R_{Y\beta}^L f_\beta^{\text{IV}}(\zeta^{\text{IV}}) , \quad (3.1.50)$

where, c_A is the concentration of Li^+ sites, J_A is the molar flux of Li^+ in electrodes, L_ε is the inverse of the solid viscosity of electrodes, L_χ is the mobility of order parameter ζ^χ , L_A is the diffusion coefficient of Li^+ , f_A^L reflects the interaction frequency between Li^+ and vacancies for diffusion, α^L is the symmetry factor for the diffusion of Li^+ , A^L is the driving force coefficient for diffusion, which is controlled by the path factor with respect to ζ^{II} , ∇ is the gradient operator, c_Y is the characteristic concentration of dislocations, J_Y is the flux of dislocations, and f_Y^L revealing the influence of crystalline, which is controlled by the path factor with respect to ζ^{IV} .

The diffusion of Li^+ can be considered as the interaction between Li^+ and the vacancies nearby. We introduce the transition-state theory to model the flux of Li^+ (Equation (3.1.45)). The transition-state model is mathematically equivalent to the classic linear diffusion model when A^L is small enough. A dislocation is generated by the movement of atoms in crystal. Based on the mass conservation of the moving atoms, dislocation density can be considered conserved [117]. The dislocation density Y in this chapter is a continuous homogenized quantity which describes the quantity of dislocations in a tiny region of the particle. It includes information about Burger's vectors and hence can be positive or negative. The mixture of positive dislocation and negative dislocation leads to their annihilation. We use Equation (3.1.48) and Equation (3.1.49) which is the kinetics for a conserved order parameter to govern the mobile dislocations in this chapter.

Dislocations can be generated and annihilated on particle surfaces [45], which is named dislocation reaction. We consider that the dislocation reaction and the electrochemical reaction of Li^+ are coupled together on particle surface. The reactions on the surface of particles are described as below,

$$I_N = \sum_k A_0 h_{RA} F J_{AI} , \quad (3.1.51)$$

$$J_{AI} = \frac{J_A}{h_{RA}} , \quad (3.1.52)$$

$$J_{YI} = \frac{J_Y}{h_{RY}} , \quad (3.1.53)$$

$$A_{AI} = \mu_A - \mu_I - r_A^F A_{AY} , \quad (3.1.54)$$

$$A_{YI} = \mu_Y + r_Y^F (\zeta^{IV}) A_{AY} , \quad (3.1.55)$$

$$\mu_I + F\phi = \mu_E , \quad (3.1.56)$$

$$J_{AI} = J_{AI0} f_{AI}(y_A) \left\{ \exp\left(-\frac{\alpha_{AI} A_{AI}}{RT}\right) - \exp\left[-\frac{(\alpha_{AI} + 1) A_{AI}}{RT}\right] \right\} , \quad (3.1.57)$$

$$J_{AY} = J_{AI} - r_A^{JY} J_{YI} = J_{AY0} \left\{ \exp\left(-\frac{\alpha_{AY} A_{AY}}{RT}\right) - \exp\left[-\frac{(\alpha_{AY} + 1) A_{AY}}{RT}\right] \right\} , \quad (3.1.58)$$

$$J_{YI} = J_{YI0} \left\{ \exp\left(-\frac{\alpha_{YI} A_{YI}}{RT}\right) - \exp\left[-\frac{(\alpha_{YI} + 1) A_{YI}}{RT}\right] \right\} , \quad (3.1.59)$$

$$f_{AI}(y_A) = y_A^{N_{AI}^A} y_B^{N_{AI}^B} , \quad (3.1.60)$$

$$r_Y^F (\zeta^{IV}) = r_{Y\alpha}^F f_{\alpha}^{IV} (\zeta^{IV}) + r_{Y\beta}^F f_{\beta}^{IV} (\zeta^{IV}) , \quad (3.1.61)$$

with the following meaning of symbols. I_N is the total electrical current of all particles. A_0 is the reaction surface area of every particle. h_{RA} is the reaction depth of electrochemical reaction. F is Faraday constant. J_{AI} is electrochemical reaction rate. J_{YI} is dislocation reaction rate. h_{RY} is the thickness of dislocation reaction. A_{AI} is the driving force of electrochemical reaction. μ_I is the chemical potential of Li^+ in electrolyte. A_{AY} is the coupling force between electrochemical

reaction and dislocation reaction. r_A^F is the coupling coefficient for electrochemical reaction. A_{YI} is the driving force of dislocation reaction. r_Y^F is the coupling coefficient for dislocation reaction, which is controlled by crystalline (ζ^{IV}). ϕ is electrical potential. μ_E is the equilibrium chemical potential of Li^+ in electrolyte, which can be considered as a constant. J_{AI0} is reference electrochemical reaction rate. f_{AI} reveals the activity of Li^+ in the reaction. α_{AI} is the symmetry factor for electrochemical reaction. J_{AY} is the coupling rate between electrochemical reaction and dislocation reaction. r_A^{JY} is the coupling coefficient between two reactions. J_{AY0} is reference coupling rate. α_{AY} is the symmetry factor of coupling reaction. J_{YI0} is reference dislocation reaction rate. α_{YI} is the symmetry factor for dislocation reaction. N_{AI}^A and N_{AI}^B are the activity powers for occupied sites and unoccupied sites respectively. $r_{Y\alpha}^F$ and $r_{Y\beta}^F$ are the coupling coefficients for crystal structure and amorphous structure respectively.

The characteristic strain ε is equivalent to the lattice parameters of electrode materials. We can compare the simulated X-ray diffraction (XRD) graphs yielded from ε with existing experimental observations [64] [77] to validate the path altering mechanism of energy changing during (de)lithiation. The model for generating XRD graphs is given by,

$$\kappa = 1 - \varepsilon \quad (3.1.62)$$

$$\psi_X = f_X^\psi(y_A) \psi_X^{REF} \exp\left\{-\left[A_X^\psi(\kappa_I - \kappa)\right]^2\right\}, \text{ with } X \in \{\alpha, \beta\} \quad (3.1.63)$$

$$f_\alpha^\psi(y_A) = \left(R_{H\alpha}^\psi - R_{L\alpha}^\psi\right) y_A^{N_\alpha^\psi} + R_{L\alpha}^\psi \quad (3.1.64)$$

$$f_\beta^\psi(y_B) = \left(R_{H\beta}^\psi - R_{L\beta}^\psi\right) y_B^{N_\beta^\psi} + R_{L\beta}^\psi \quad (3.1.65)$$

$$\psi = f_{IV}^\psi(\zeta^{IV}) \left(\psi_\alpha f_\alpha^1 + \psi_\beta f_\beta^1\right) \quad (3.1.66)$$

$$f_{IV}^{\psi}(\zeta^{IV}) = (R_{HIV}^{\psi} - R_{LIV}^{\psi})(\zeta^{IV})^{N_{IV}^{\psi}} + R_{LIV}^{\psi} \quad (3.1.67)$$

$$\Psi = \sum_k \int_V \psi dV \quad (3.1.68)$$

with symbols explained as blow. κ is the location of the XRD peak. ψ_X is the intensity density for phase X. f_X^{ψ} is the adapting factor depending on Li^+ fraction. ψ_X^{REF} is reference intensity density. A_X^{ψ} is accuracy coefficient. κ_l is input peak location. α stands for Li-rich phase and β represents Li-poor phase. R_{HX}^{ψ} is the higher adapting reference factor for X phase. R_{LX}^{ψ} is the lower adapting reference factor for X phase. ψ is intensity density. f_{IV}^{ψ} is the adapting factor controlled by crystalline. R_{HIV}^{ψ} is the higher adapting reference factor for crystalline change. R_{LIV}^{ψ} is the lower adapting reference factor for crystalline change. N_{IV}^{ψ} is the sensitivity coefficient for f_{IV}^{ψ} . Ψ is the total intensity of XRD. V stands for the integral with respect to the volume of particle. \sum_k represents the summation of intensity for all particles.

3.1.3 Numerical simulations

Based on the path altering mechanism mentioned above, the state evolutions of LiFePO_4 (LFP) and $\text{LiNi}_{1/3}\text{Mn}_{1/3}\text{Co}_{1/3}\text{O}_2$ (NMC111) systems are numerically simulated under different (de)lithiation conditions by solving the governing equations using finite difference method. The simulation includes two parts as follows,

- a. The diffusion limitation of Li^+ is neglected by directly inputting the change of Li^+ fraction in a LFP particle. This setting is equivalent to that the diffusivity of Li^+ is infinite, or the particle size is small enough to be neglected. This part can output the

curves of main parameters ($\varepsilon, Y, \zeta^I, \zeta^{II}, \zeta^{III}, \zeta^{IV}$) versus Li^+ fraction y_A , and directly display the path altering phenomenon during (de)lithiation under different C-rates.

This part is applied in Mathematica.

- b. The diffusion limitation of Li^+ is included. The results in this part include XRD graphs and phase field evolutions for LFP and NMC111, which are compared to existing experimental observations [64] [77] [66], and used for validating the path altering mechanism. This part is calculated using Matlab.

The particle sizes in the multi-particle systems simulated in this study obey the log-normal distribution. The mean size and standard deviation for LFP is 186 nm and 0.35 respectively. The mean size and standard deviation for NMC111 is 186 nm and 0.15 respectively. We calculated the XRD graphs and Li^+ fraction field evolutions for the multi-particle systems under galvanostatic cycling with different C-rates (5C, 10C, 20C for LFP and C/15, 4C for NMC111). 270 seconds open circuit relaxation after 90 seconds 10C partial delithiation is included for LFP. In addition, the potentiostatic delithiation of a single LFP particle with size 300nm is simulated for 4V vs Li/Li^+ , which displays the order-disorder structure transition for LFP under non-equilibrium process. Based on symmetry, only half of the particle is modeled for every particle in the system. The concentrations of Li^+ sites are $c_A = 2.2668 \times 10^4 \text{ mol} / \text{m}^3$ for LFP and $c_A = 5.1296 \times 10^4 \text{ mol} / \text{m}^3$ for NMC111. Other parameters for LFP and NMC111 used in the simulations are displayed in Table 3.2 and Table 3.3, where l_C is the characteristic length which is the half of the mean size of particles.

Table 3.2 Material parameters for LFP.

#Estimated value based on the results in Maxisch and Ceder[12]

Parameter	Value	Parameter	Value	Parameter	Value	Parameter	Value
$\frac{A_{\alpha}^L RT}{l_C}$	0.1	$\frac{A_{\beta}^L RT}{l_C}$	0.3	A_{α}^{ψ}	7	A_{β}^{ψ}	7
$\frac{a^{RS}}{RT}$	22.1824	$\frac{a_{A\alpha}^R}{RT}$	-2.3588	$\frac{a_{B\alpha}^R}{RT}$	-2.3588	$\frac{a_{B\beta\alpha}^R}{RT}$	-0.03
$\frac{a_{A\beta\alpha}^R}{RT}$	0	$\frac{a_{A\beta\beta\alpha}^R}{RT}$	-0.03	$\frac{a_{A\beta\beta\beta}^R}{RT}$	0	$\frac{a_{B\beta\alpha\alpha}^R}{RT}$	0
$\frac{a_{B\beta\alpha\beta}^R}{RT}$	-0.03	$\frac{a_{B\beta\beta\alpha}^R}{RT}$	0	$\frac{a_{B\beta\beta\beta}^R}{RT}$	-0.03	$\frac{C^E}{RT}$	2.28#
$\frac{C^N}{RT}$	0.01	c_Y	10	$\frac{H_{A\alpha}^D}{RT}$	10	$\frac{H_{B\alpha}^D}{RT}$	10
$\frac{H_{A\beta\alpha\alpha}^D}{RT}$	8.5	$\frac{H_{A\beta\alpha\beta}^D}{RT}$	8.5	$\frac{H_{A\beta\beta\alpha}^D}{RT}$	8.5	$\frac{H_{A\beta\beta\beta}^D}{RT}$	8.5
$\frac{H_{B\beta\alpha\alpha}^D}{RT}$	8.5	$\frac{H_{B\beta\alpha\beta}^D}{RT}$	8.5	$\frac{H_{B\beta\beta\alpha}^D}{RT}$	8.5	$\frac{H_{B\beta\beta\beta}^D}{RT}$	8.5
$\frac{H_{A\alpha}^{PI}}{RT}$	2.5	$\frac{H_{B\alpha}^{PI}}{RT}$	2.5	$\frac{H_{A\beta\alpha}^{PI(2)}}{RT}$	0.01	$\frac{H_{A\beta\alpha}^{PI(4)}}{RT}$	0.1
$\frac{H_{A\beta\beta}^{PI(2)}}{RT}$	0.01	$\frac{H_{A\beta\beta}^{PI(4)}}{RT}$	0.1	$\frac{H_{B\beta\alpha}^{PI(2)}}{RT}$	0.01	$\frac{H_{B\beta\alpha}^{PI(4)}}{RT}$	0.1
$\frac{H_{B\beta\beta}^{PI(2)}}{RT}$	0.01	$\frac{H_{B\beta\beta}^{PI(4)}}{RT}$	0.1	$\frac{H^{PII(2)}}{RT}$	0.1	$\frac{H^{PII(4)}}{RT}$	0.1
$\frac{H^{PIII(2)}}{RT}$	0.01	$\frac{H^{PIII(4)}}{RT}$	0.1	$\frac{H^{PIV(2)}}{RT}$	0.01	$\frac{H^{PIV(4)}}{RT}$	0.01
$\frac{h_{RA}}{l_C}$	7×10^{-3}	$\frac{h_{RY}}{l_C}$	7×10^{-3}	$\frac{J_{AI0} h_{RA}}{c_A l_C}$	3.088×10^{-4}	$\frac{J_{AY0} h_{RA}}{c_A l_C}$	9.3×10^{-6}
$\frac{J_{YI0} h_{RY}}{c_Y l_C}$	70	$\frac{K_A}{RT l_C^2}$	0.005	$\frac{K_I}{RT l_C^2}$	6×10^{-5}	$\frac{K_{II}}{RT l_C^2}$	0
$\frac{K_{III}}{RT l_C^2}$	0	$\frac{K_{IV}}{RT l_C^2}$	1×10^{-5}	$\frac{L_A}{c_A l_C}$	0.0112155	$L_{\epsilon} RT$	12.471
$\frac{L_Y RT}{c_Y l_C^2}$	0.01442	$L_I RT$	2.4942	$L_{II} RT$	0.1247	$L_{III} RT$	0.0748

Table 3.2 (continued).

$L_{IV}RT$	0.0249	N_{AI}^A	0.5	N_{AI}^B	0.5	$R_{Y\alpha}^L$	1
$R_{Y\beta}^L$	0	r^{IV}	0.7	r_A^F	0.5	$r_{Y\alpha}^F$	3.6859
$r_{Y\beta}^F$	6.5852	r_A^{JY}	1	T	300	$Y_{A\alpha}^R$	0
$Y_{B\alpha}^R$	0	$Y_{A\beta\alpha}^R$	-0.05	$Y_{A\beta\alpha\beta}^R$	-0.05	$Y_{A\beta\beta\alpha}^R$	0.05
$Y_{A\beta\beta\beta}^R$	0.05	$Y_{B\beta\alpha}^R$	-0.05	$Y_{B\beta\alpha\beta}^R$	-0.05	$Y_{B\beta\beta\alpha}^R$	0.05
$Y_{B\beta\beta\beta}^R$	0.05	α^L	-0.5	α_{AI}	-0.5	α_{AY}	-0.5
α_{YI}	-0.5	$\varepsilon_{A\alpha}^R$	1	$\varepsilon_{B\alpha}^R$	0	$\varepsilon_{A\beta\alpha}^R$	1
$\varepsilon_{A\beta\alpha\beta}^R$	0.5	$\varepsilon_{A\beta\beta\alpha}^R$	1	$\varepsilon_{A\beta\beta\beta}^R$	0.1	$\varepsilon_{B\beta\alpha\alpha}^R$	0.35
$\varepsilon_{B\beta\alpha\beta}^R$	0	$\varepsilon_{B\beta\beta\alpha}^R$	0.5	$\varepsilon_{B\beta\beta\beta}^R$	0.035	$\zeta_{A\alpha}^{IR}$	1
$\zeta_{B\alpha}^{IR}$	0	$\zeta_{A\beta\alpha}^{IR}$	1	$\zeta_{A\beta\beta}^{IR}$	1	$\zeta_{B\beta\alpha}^{IR}$	0
$\zeta_{B\beta\beta}^{IR}$	0	ζ^{IIR}	0.5	ζ^{IIIR}	0.5	ζ^{IVR}	0.5
ψ_{α}^{REF}	1	ψ_{β}^{REF}	2.5				

Table 3.3 Material parameters for NMC111.

Estimated value based on the results in Cheng et al. [118]

Parameter	Value	Parameter	Value	Parameter	Value	Parameter	Value
$\frac{A_\alpha^L RT}{l_C}$	0.1	$\frac{A_\beta^L RT}{l_C}$	0.1	A_α^ψ	10	A_β^ψ	10
$\frac{a^{RS}}{RT}$	3	$\frac{a_{A\alpha}^R}{RT}$	-2.3588	$\frac{a_{B\alpha}^R}{RT}$	-2.3588	$\frac{a_{A\beta\alpha}^R}{RT}$	-0.03
$\frac{a_{A\beta\alpha}^R}{RT}$	0	$\frac{a_{A\beta\beta\alpha}^R}{RT}$	-0.03	$\frac{a_{A\beta\beta\beta}^R}{RT}$	0	$\frac{a_{B\beta\alpha\alpha}^R}{RT}$	0
$\frac{a_{B\beta\alpha\beta}^R}{RT}$	-0.03	$\frac{a_{B\beta\beta\alpha}^R}{RT}$	0	$\frac{a_{B\beta\beta\beta}^R}{RT}$	-0.03	$\frac{C^E}{RT}$	1.245#
$\frac{C^N}{RT}$	1.245	c_Y	10	$\frac{H_{A\alpha}^D}{RT}$	10	$\frac{H_{B\alpha}^D}{RT}$	10
$\frac{H_{A\beta\alpha\alpha}^D}{RT}$	8.5	$\frac{H_{A\beta\alpha\beta}^D}{RT}$	8.5	$\frac{H_{A\beta\beta\alpha}^D}{RT}$	8.5	$\frac{H_{A\beta\beta\beta}^D}{RT}$	8.5
$\frac{H_{B\beta\alpha\alpha}^D}{RT}$	8.5	$\frac{H_{B\beta\alpha\beta}^D}{RT}$	8.5	$\frac{H_{B\beta\beta\alpha}^D}{RT}$	8.5	$\frac{H_{B\beta\beta\beta}^D}{RT}$	8.5
$\frac{H_{A\alpha}^{PI}}{RT}$	0.5	$\frac{H_{B\alpha}^{PI}}{RT}$	2	$\frac{H_{A\beta\alpha}^{PI(2)}}{RT}$	0.75	$\frac{H_{A\beta\alpha}^{PI(4)}}{RT}$	0
$\frac{H_{A\beta\beta}^{PI(2)}}{RT}$	0.25	$\frac{H_{A\beta\beta}^{PI(4)}}{RT}$	0	$\frac{H_{B\beta\alpha}^{PI(2)}}{RT}$	2	$\frac{H_{B\beta\alpha}^{PI(4)}}{RT}$	0
$\frac{H_{B\beta\beta}^{PI(2)}}{RT}$	0.5	$\frac{H_{B\beta\beta}^{PI(4)}}{RT}$	0	$\frac{H^{PII(2)}}{RT}$	0.1	$\frac{H^{PII(4)}}{RT}$	0.1
$\frac{H^{PIII(2)}}{RT}$	0.01	$\frac{H^{PIII(4)}}{RT}$	0.1	$\frac{H^{PIV(2)}}{RT}$	0.01	$\frac{H^{PIV(4)}}{RT}$	0.01
$\frac{h_{RA}}{l_C}$	7×10^{-3}	$\frac{h_{RY}}{l_C}$	7×10^{-3}	$\frac{J_{AI0} h_{RA}}{c_A l_C}$	1.365×10^{-4}	$\frac{J_{AY0} h_{RA}}{c_A l_C}$	3.69×10^{-5}
$\frac{J_{YI0} h_{RY}}{c_Y l_C}$	70	$\frac{K_A}{RT l_C^2}$	0.005	$\frac{K_I}{RT l_C^2}$	0	$\frac{K_{II}}{RT l_C^2}$	0
$\frac{K_{III}}{RT l_C^2}$	0	$\frac{K_{IV}}{RT l_C^2}$	0	$\frac{L_A}{c_A l_C}$	0.5	$L_\epsilon RT$	12.471
$\frac{L_Y RT}{c_Y l_C^2}$	0.02884	$L_I RT$	2.4942	$L_{II} RT$	0.1247	$L_{III} RT$	0.0748

Table 3.3 (continued).

$L_{IV}RT$	0.0249	N_{AI}^A	0.5	N_{AI}^B	0.5	$R_{Y\alpha}^L$	1
$R_{Y\beta}^L$	0	r^{IV}	1	r_A^F	0.2	$r_{Y\alpha}^F$	5
$r_{Y\beta}^F$	5	r_A^{JY}	1	T	300	$Y_{A\alpha}^R$	0
$Y_{B\alpha}^R$	0	$Y_{A\beta\alpha}^R$	-0.05	$Y_{A\beta\alpha\beta}^R$	-0.05	$Y_{A\beta\beta\alpha}^R$	0.05
$Y_{A\beta\beta}^R$	0.05	$Y_{B\beta\alpha}^R$	-0.05	$Y_{B\beta\alpha\beta}^R$	-0.05	$Y_{B\beta\beta\alpha}^R$	0.05
$Y_{B\beta\beta}^R$	0.05	α^L	-0.5	α_{AI}	-0.5	α_{AY}	-0.5
α_{YI}	-0.5	$\varepsilon_{A\alpha}^R$	1	$\varepsilon_{B\alpha}^R$	0	$\varepsilon_{A\beta\alpha\alpha}^R$	1
$\varepsilon_{A\beta\alpha\beta}^R$	1	$\varepsilon_{A\beta\beta\alpha}^R$	1	$\varepsilon_{A\beta\beta\beta}^R$	1	$\varepsilon_{B\beta\alpha\alpha}^R$	0
$\varepsilon_{B\beta\alpha\beta}^R$	0	$\varepsilon_{B\beta\beta\alpha}^R$	0	$\varepsilon_{B\beta\beta\beta}^R$	0	$\zeta_{A\alpha}^{IR}$	1
$\zeta_{B\alpha}^{IR}$	0	$\zeta_{A\beta\alpha}^{IR}$	1	$\zeta_{A\beta\beta}^{IR}$	1	$\zeta_{B\beta\alpha}^{IR}$	0
$\zeta_{B\beta\beta}^{IR}$	0	ζ^{IIR}	0.5	ζ^{IIIR}	0.5	ζ^{IVR}	0.5
ψ_{α}^{REF}	1	ψ_{β}^{REF}	1				

3.2 Results and Discussion

Figure 3.1a-c displays the free energy of LFP for different dislocation densities. The lowest free energy locates on $(\zeta^{\text{III}}, \zeta^{\text{IV}}) = (1,1)$, $(\zeta^{\text{III}}, \zeta^{\text{IV}}) = (0,1)$, and $(\zeta^{\text{III}}, \zeta^{\text{IV}}) = (0,0)$, when $Y = 0$, $Y = -2$, and $Y = -4$ respectively. With the physical meaning of order parameters listed in Table 3.1, LFP adopts the following paths to minimize the free energy. (1) LFP shows equilibrium state and crystal structure when there are no dislocations. (2) When dislocations are introduced with small quantity, LFP transfers to non-equilibrium state while keeping the crystal structure. (3) When the quantity of dislocations is large enough, LFP displays the amorphous structure with the non-equilibrium state.

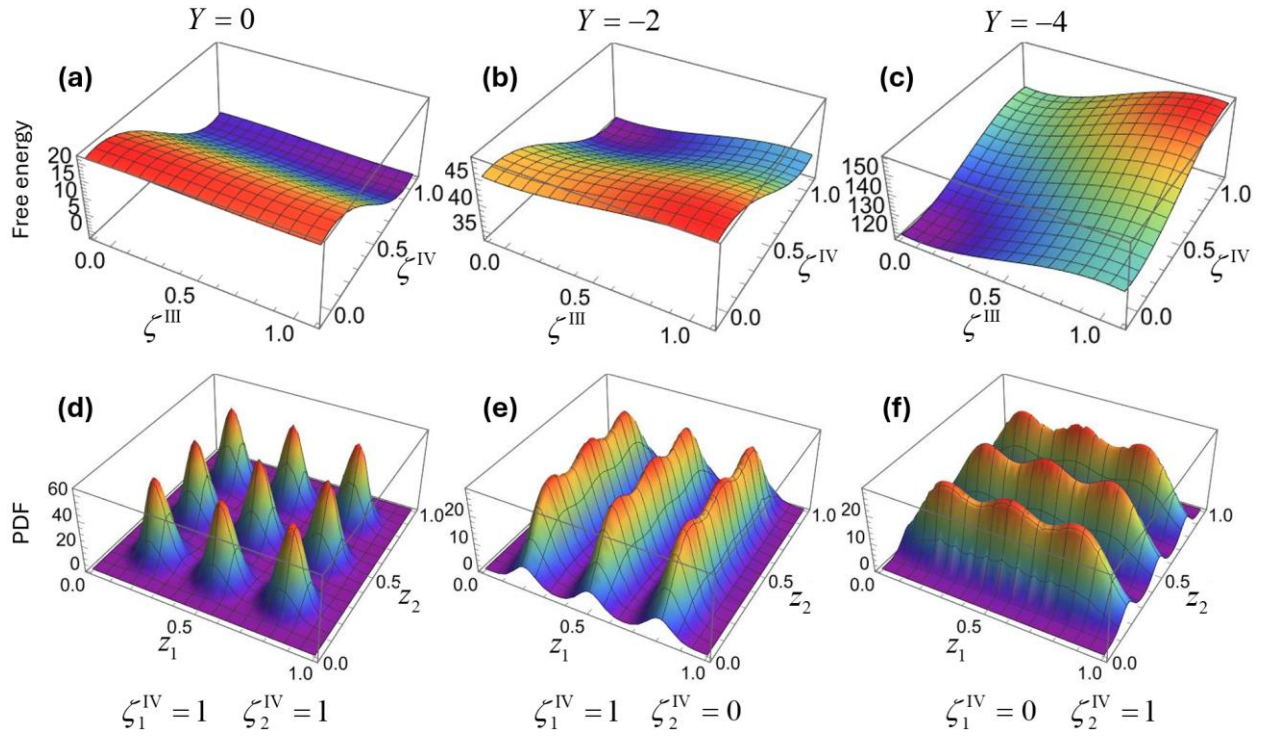


Figure 3.1 Free energy of LFP vs. order parameters ζ^{III} and ζ^{IV} when dislocation density (a) $Y = 0$, (b) $Y = -2$, and (c) $Y = -4$. For 2-dimensional LFP model, the component of ζ^{IV} tensor, ζ_1^{IV} and ζ_2^{IV} , independently affect the probability density function (PDF) of Li^+ sites' location in (z_1, z_2) space. LFP shows crystal structure for (d) both directions when $\zeta_1^{\text{IV}} = 1$ and $\zeta_2^{\text{IV}} = 1$, and only one direction when (e) $\zeta_1^{\text{IV}} = 1$, $\zeta_2^{\text{IV}} = 0$ or (f) $\zeta_1^{\text{IV}} = 0$ and $\zeta_2^{\text{IV}} = 1$.

The crystalline parameter ζ^{IV} is a 2nd order tensor. For the dimension larger than 1, the components of ζ^{IV} is more than 1 and can independently represent the structural order on different directions. As the 2-D space shown in **Figure 3.1d-f**, the probability density function (PDF) of Li^+ sites' location indicates the crystal structure on (1) both directions when the tensor components $\zeta_1^{\text{IV}} = 1$ and $\zeta_2^{\text{IV}} = 1$, (2) only one direction and the amorphous structure on the other direction when either ζ_1^{IV} or ζ_2^{IV} is 0. This feature explains the phenomenon shown in the in-situ transmission electron microscopy (TEM) graphs in Niu et al. [66] that the crystalline of LFP is different on different directions during relaxation (cf. Figure 2c in Niu et al. [66]).

The path altering mechanism for LFP is clearly shown in **Figure 3.2**. For quasi-equilibrium delithiation (0.1C), the chemical potential curve in **Figure 3.2a** shows the normal non-monotone shape for LFP. Although ε and ζ^{I} change linearly with respect to Li^+ fraction in **Figure 3.2d**, the non-monotone chemical potential leads to the phase separation of Li^+ fraction which makes both ε and ζ^{I} have two phases coexistence in the particle. Meanwhile, $\zeta^{\text{IV}} = 1$, $\zeta^{\text{III}} = 1$, and $\zeta^{\text{II}} = 0.5$ during the whole delithiation in **Figure 3.2d** respectively indicate the stable crystal structure, equilibrium state, and the intermediate state between delithiation state and lithiation state throughout the low C-rate delithiation process. Compared to other main parameters, dislocation density dominates the change of free energy. Increased electrical current leads to increased dislocations due to the coupling between the electrochemical reaction and the dislocation reaction on particle surfaces, and hence alters the path of energy changing. For 10C (delithiation) and -10C (lithiation), ζ^{III} goes to zero at the very beginning of the processes (**Figure 3.2e-f**), which indicates that the non-equilibrium state of LFP appears instantly. Compared to 0.1C, the chemical potential of Li^+ changes to monotone mode for 10C and -10C in

Figure 3.2b and **c**, which suggests the solid solution state of LFP throughout the (de)lithiation. The steep changes of ζ^I and ε in **Figure 3.2e-i** imply the rapid structure transition between Li-rich state and Li-poor state for the whole particle during non-equilibrium process. The transition has hysteresis between delithiation and lithiation, which is caused by the energy barrier between $\zeta^I = 1$ and $\zeta^I = 0$. Because of the kinetic limitation of ζ^I , the hysteresis is stronger under higher C-rates. In addition, it is only the feature under high C-rates that $\zeta^{II} = 1$ for delithiation and $\zeta^{II} = 0$ for lithiation (ζ^{II} lines are covered by ζ^{IV} , ζ^{III} , and ζ^{IV} in **Figure 3.2e**, **Figure 3.2f**, and **Figure 3.2i** respectively), which implies that the structure of LFP is different between delithiation and lithiation during non-equilibrium process. When electrical current increases to 30C, the structure of LFP transfers to be amorphous, as ζ^{IV} going to zero shown in **Figure 3.2g**. Compared to 30C, **Figure 3.2h** and **Figure 3.2i** display faster changes of ζ^{IV} for 50C and -50C, which suggests that the order-disorder transition can be expedited by increasing current. In the above phenomena, dislocation is the core for the variation of phase transition. Besides the electrical current, other external factors or approaches that impact the dislocation density on particle surface can alter the path of free energy change for the whole particle, which supplies potential strategies of improving or optimizing the performance of electrodes for Li-ion batteries.

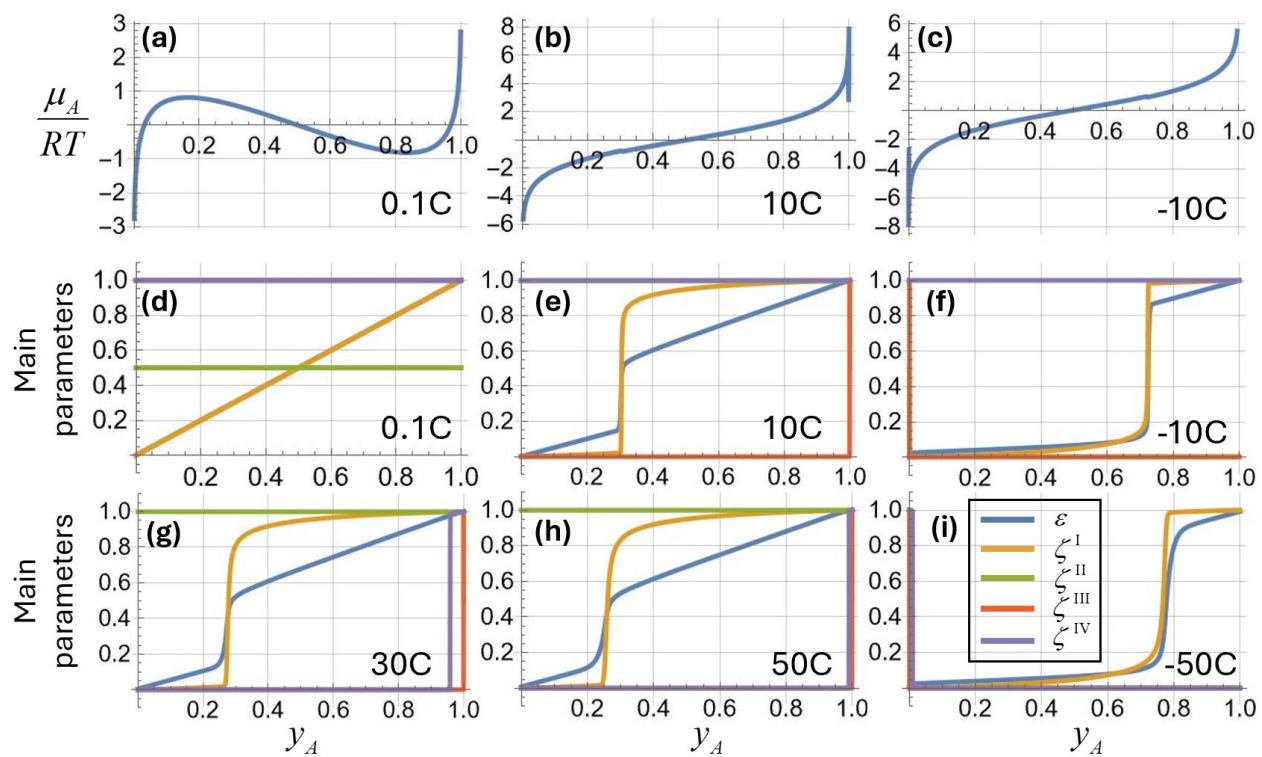


Figure 3.2 Scaled chemical potential of Li^+ in LFP at different fraction for (a) 0.1C delithiation, (b) 10C delithiation, and (c) 10C lithiation. The evolutions of main parameters with the same C-rates are recorded in (d-f) respectively. The order-disorder phase transition is revealed under (g) 30C delithiation, (h) 50C delithiation, and (i) 50C lithiation.

Figure 3.3a-c displays the XRD graphs of LFP under non-equilibrium cycling with 5C, 10C, and 20C, in which the peak locations move continuously with little overlap between Li-rich phase and Li-poor phase. LFP changes its lattice parameters rapidly throughout the whole particle, which is consistent with **Figure 3.2e-i**. The displacement of the XRD peak for Li-rich phase is much larger than that for Li-poor phase. For 10C (de)lithiation, the XRD peak's transition hysteresis between Li-rich phase and Li-poor phase is basically consistent with the hysteresis of ζ^1 and ε shown in **Figure 3.2e-f**. For the cycle with a higher C-rate, the XRD peak hysteresis and the overlap between two phases are respectively weaker and larger than those under a lower C-rate. This tendency contrasts with what is displayed in **Figure 3.2** because of the diffusion limitation included in the simulation for XRD graphs. With C-rate increased, following phenomena are shown in **Figure 3.3a-c**, (1) the intensity of Li-poor phase is decreased, (2) the maximum intensity is decreased, (3) the difference of maximal intensities between Li-rich phase and Li-poor phase changes from negative to positive, (4) the displacement of Li-rich peak is decreased, (5) the XRD pattern shows more symmetry between delithiation and lithiation, i.e., the hysteresis is weaker, and (6) the accuracy of XRD wave is decreased, especially for Li-rich phase. (7) the capacity for 5C, 10C, and 20C cycling are 0.7929, 0.7073, and 0.6109 respectively. **Figure 3.3d** shows 90 seconds delithiation with 10C rate followed by 270 seconds open circuit relaxation, which is repeated by an extra cycle. Once the current is applied, the XRD peak during the delithiation part shows the non-equilibrium path for free energy change since the peak location is changed. In the relaxation part, LFP gradually transfers to two-phase separation, which represents the equilibrium state. The intensity of the Li-poor phase after second relaxation is higher than that after first relaxation because a higher fraction of Li^+ sites has been delithiated. All above phenomena in our simulated XRD graphs in **Figure 3.3**

well agree with the experimental XRD graphs reported in Liu et al. [64], which validates the path altering mechanism for LFP under non-equilibrium process. Besides the main solid solution phases for LFP, the experimental XRD graphs in Liu et al. [64] display a slight background phase between Li-rich and Li-poor, which is relatively more noticeable for higher C-rates. The background phase may be a solid solution phase or the combination of multiple single phases with different lattice parameters spanning from Li-rich to Li-poor. Including the description of the background phase in the simulation needs to introduce more order parameters, which is omitted in this study for simplification.

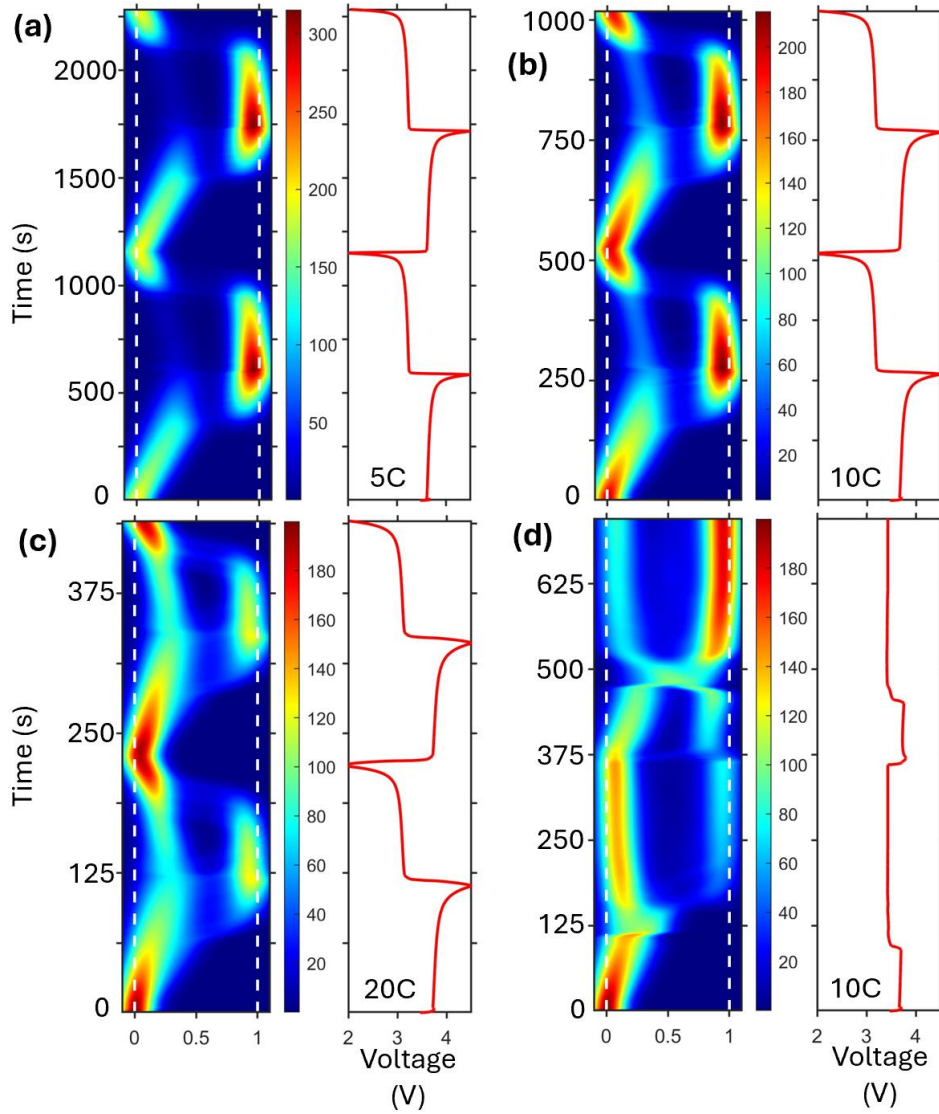


Figure 3.3 Simulated XRD graphs and electrical potentials for LFP under (a) 5C, (b) 10C, (c) 20C cycling, and (d) 90 seconds 10C delithiation followed by 270 seconds open circuit relaxation. The XRD peak location 0 and 1 indicate the lattice parameters of Li-rich phase and Li-poor phase under equilibrium state, respectively. The diffusional driving force coefficient A^L satisfies $A_\alpha^L RT / l_c = 0.1$ and $A_\beta^L RT / l_c = 0.3$.

Figure 3.4a, b, and c show the Li^+ fraction profiles in ten LFP particles respectively for 5C, 20C, and 90 seconds 10C delithiation followed by 270 seconds open circuit relaxation. Because of the size difference between particles, smaller particles will be consumed faster than larger particles, which is a feature of the population effect. The particle sizes adopted in the simulation obey the log-normal distribution. The mean size and the standard deviation are 186nm and 0.35 respectively, based on the experimental sample in Liu et al. [64]. Every particle is scaled to the same nondimensionalized size and simulated in half with symmetry. The left end and the right end of every particle are the center and the surface respectively. The Li^+ fractions in **Figure 3.4a** and **Figure 3.4b** show gradual changes throughout the particles instead of sharp changes, which indicates the solid solution without phase separation. By comparing **Figure 3.4a** with **Figure 3.4b**, the fraction gradient of Li^+ for 5C is less than that for 20C, because of the diffusion limitation. The differences of the Li^+ fraction gradient between large particles and small particles keeps similar between 5C and 20C, which means that the population effect is so weak that should not be the reason of generating the solid solution state during non-equilibrium process. The altering between the solid solution path during delithiation and the phase separation path during relaxation displayed in **Figure 3.4c** is consistent to the feature revealed in **Figure 3.2** and **Figure 3.3**. **Figure 3.3d** and **Figure 3.4c** show that re-applying the electrical current under the phase separated state after the first relaxation makes LFP re-entering the solid solution state, which implies that the solid solution of LFP is a stable state instead of a transient kinetic state during (de)lithiation.

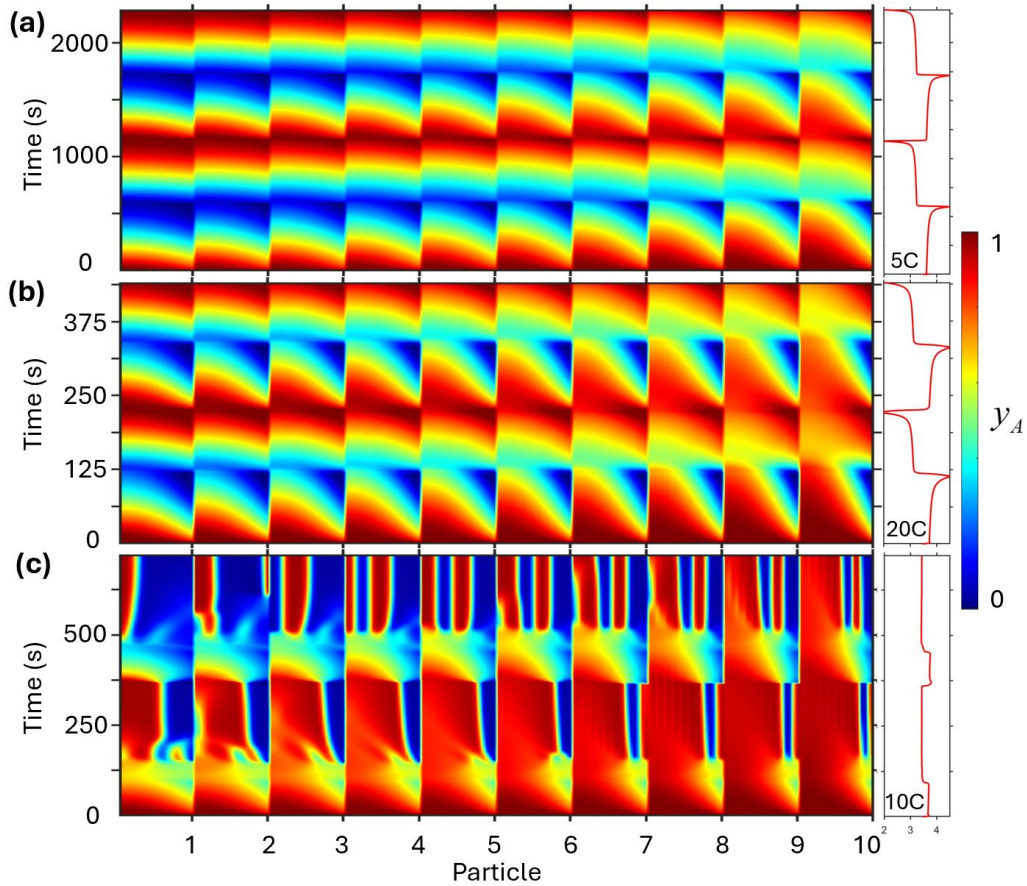


Figure 3.4 Li^+ fraction profiles in ten LFP particles with different sizes that obey the log-normal distribution (mean size 186nm, standard deviation 0.35) during **(a)** 5C and **(b)** 20C cycling, and **(c)** 90 seconds 10C delithiation followed by 270 seconds open circuit relaxation. All particles are scaled to the same nondimensionalized size. Larger particles are marked by larger numbers. Based on the symmetry, all particles are simulated in half. The left end and the right end are respectively the center and the surface of every particle.

The solid solution phenomenon of LFP in Zhao et al. [119] is explained by the population effect and modeled using Fokker-Planck equation. Compared to our path altering mechanism, the modeling with Fokker-Planck equation lacks information about material properties and cannot clearly explain the variation for phase transition in detail. Based on the measured and calculated miscibility gaps between Li-rich and Li-poor phases for the LFP particles with different sizes[57][59], the partial delithiated particle of size 186nm should clearly show the sharp phase interface of the two phases coexistence with $\text{Li}_{0.95}\text{FePO}_4$ for Li-rich and $\text{Li}_{0.05}\text{FePO}_4$ for Li-poor in the particle under equilibrium. Therefore, the XRD intensity in the relaxation process shown in Liu et al. [64] (cf. Figure 2D) is dominated by the phase separation in particles instead of the single-phase particles of Li-rich or Li-poor. However, the phase separation is not revealed in the simulation based on Fokker-Planck equation in Zhao et al. [119], as the field information is not included. In addition, the simulation about relaxation and re-(dis)charging for the partial delithiated LFP is important since it can indicate the stability of the solid solution state, which is not validated with the Fokker-Planck equation in Zhao et al. [119]. In contrast to the phase transitions in **Figure 3.3** in our study, the symmetry between delithiation and lithiation for phase transition in the simulation of Zhao et al. [119] does not agree with the observed symmetry of XRD graphs for LFP in Liu et al. [64]. Therefore, the solid solution phenomenon for LFP under non-equilibrium process is caused by the dislocation-induced path altering for free energy change rather than the population effect of electrode particles.

In **Figure 3.3**, the intensities of Li -rich phase for delithiation and lithiation are like each other, which agrees with the experimental XRD graphs in Liu et al. [64]. This result is simulated based on unsymmetric diffusional driving force coefficient A^L , with $A_\alpha^L RT / l_c = 0.1$ for delithiation ($\zeta^{\text{II}} = 1$) and $A_\beta^L RT / l_c = 0.3$ for lithiation ($\zeta^{\text{II}} = 0$). If A^L is a constant and has no

difference between lithiation and delithiation, simulated XRD graphs will mismatch the experimental XRD graphs, which is shown in **Figure 3.5** below. The intensity of the Li-rich phase in delithiation process is much larger than that in lithiation process. This comparison represents the necessary asymmetry for A^L , which reveals that the structure of LFP is different between delithiation and lithiation.

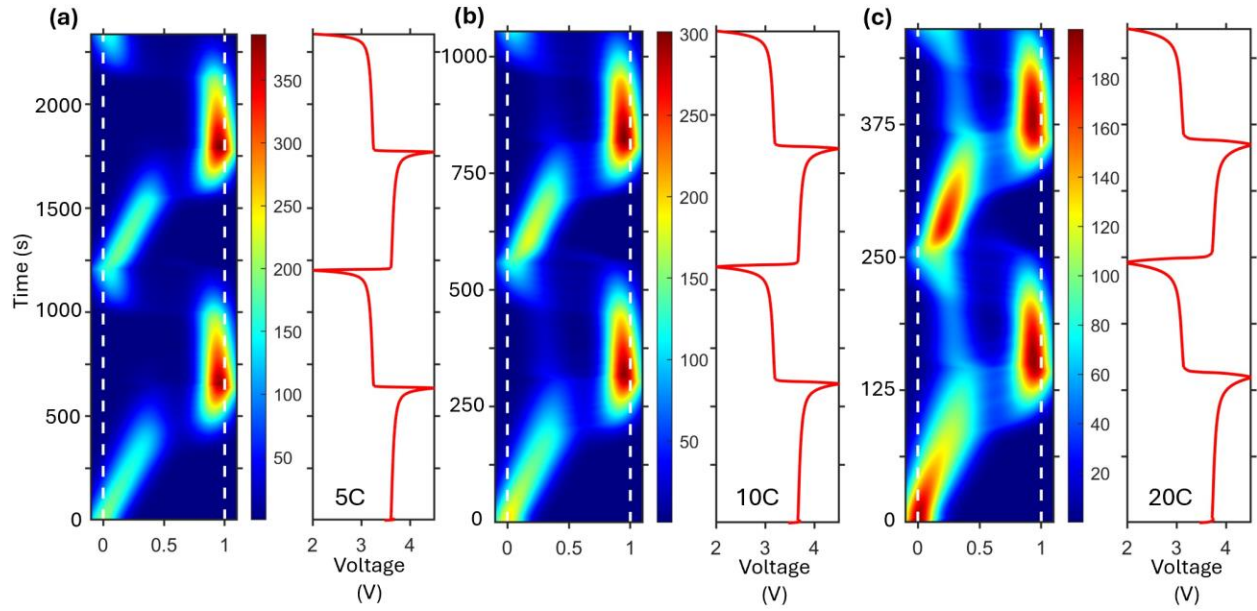


Figure 3.5 Simulated XRD graphs and electrical potentials for LFP under (a) 5C, (b) 10C, and (c) 20C cycling. The XRD peak location 0 and 1 indicate the lattice parameters of Li-rich phase and Li-poor phase under equilibrium state, respectively. The diffusional driving force coefficient

$$A^L \text{ is a constant that satisfies } A_{\alpha}^L RT / l_C = A_{\beta}^L RT / l_C = 0.15 .$$

Besides the change of lattice parameters, the order-disorder coexistence for LFP during non-equilibrium process reported in Niu et al. [66] can be simulated based on our formulation of the free energy with multi-layered states. **Figure 3.6** shows the evolution of order parameter ζ^{IV} and the electrical current during the potentiostatic delithiation of 4V vs Li/Li⁺ for a single LFP particle with size 300nm, which includes following phenomena, (1) ζ^{IV} near the surface of the LFP particle decreases to 0 rapidly right after 4V voltage is applied, (2) the depth of the amorphous zone is about 30nm, (3) the amorphous zone keeps unchanged until around 300 seconds, (4) most of the amorphous zone recovered back to crystal structure after 300 seconds, but there is still a small part keeps amorphous stably, (5) The electrical current decreases to around 1C when LFP is recovered to crystal structure (300 seconds). The above phenomena all agree with the experimental observations of the in-situ TEM in Niu et al. [66], which validates the path altering mechanism in this study.

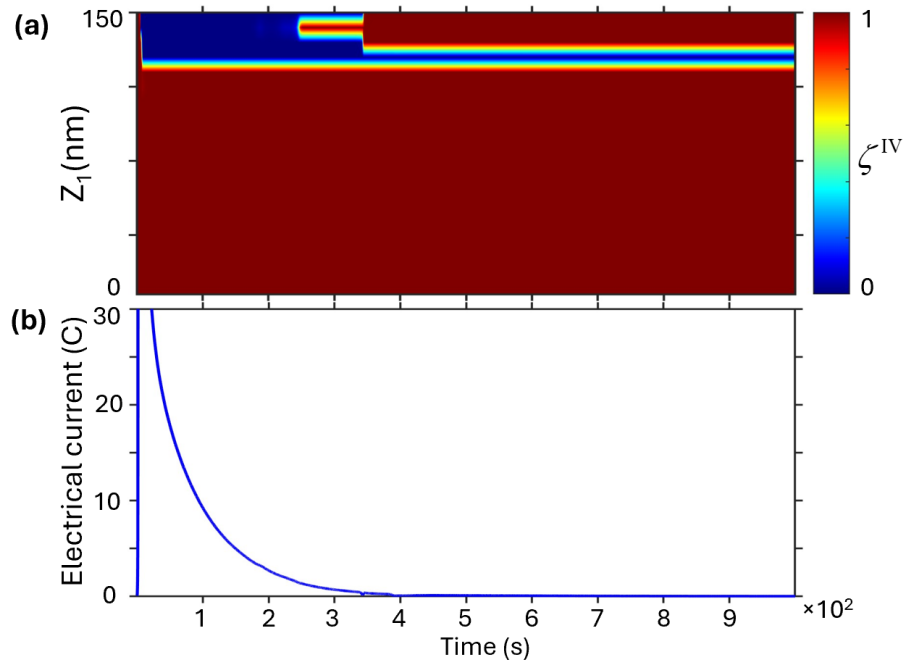


Figure 3.6 Profiles of (a) crystalline (ζ^{IV}) and (b) electrical current for a single LFP particle with size 300 nm during 4V vs Li/Li⁺ potentiostatic delithiation, where z_1 is the spatial coordinate of the particle. Only half of the particle is simulated due to symmetry.

Figure 3.7a and **Figure 3.7b** display the simulated XRD graphs for NMC111 multi-particles under C/15 and 4C cycles respectively. Under C/15 cycle, NMC111 keeps equilibrium with the normal solid solution phase, whose lattice parameter shows roughly linear change between lithiated state and delithiated state. The simulation for 4C displays the non-equilibrium process, in which NMC111 alters to phase separation path. Unlike the path altering for LFP shown in **Figure 3.3**, the variation of phase transitions for NMC111 is not symmetric between delithiation and lithiation since the change of the structural energy coefficient $H_{XLM}^{PI(2)}$ between delithiation and lithiation for occupied sites is different from that for unoccupied sites. The above simulated phenomena for NMC111 well agree with the experimental XRD graphs reported by Park et al. [77]. The profiles of Li^+ fraction in ten particles are presented in **Figure 3.7c** and **Figure 3.7d**, where the particles are scaled to the same nondimensionalized size. With symmetry, all particles are simulated in half. The sizes of the particles obey the log-normal distribution with mean size 186nm and standard deviation 0.15. Compared to the even distributed Li^+ fraction for C/15 in **Figure 3.7c**, Li^+ fraction shows phase separation under 4C delithiation in **Figure 3.7d**. Meanwhile, the difference of the changing rate of Li^+ fraction is so small between large particles and small particles that no population effect is shown. Therefore, the reason for the variation of phase transition for NMC111 should be the path altering induced by dislocations instead of the population effect. In Park et al. [77], the phase separation for NMC111 is explained to be fictitious and modeled based on exponentially changed diffusivity upon Li^+ fraction. However, the capacity loss between charging and discharging in the diffusion limited case and mixed-controlled case (cf. Figure S12a in Park et al. [77]) is much larger than the experiment measurement (cf. Figure 1e in Park et al. [77]). It also does not agree with the smaller capacity loss between charging and discharging in Pathak et al. [120]. Although the

strong diffusivity change can lead to the step distribution of Li^+ fraction in particles during delithiation, it can also lead to strong capacity asymmetry between delithiation and lithiation, i.e., large capacity loss in a cycle, based on the reason below. Under high C-rate, an electrode particle can only be partially lithiated if Li^+ diffusivity rapidly decreases upon the increase of Li^+ fraction, because rapidly increased Li^+ near the surface of the particle can blocked the migration of Li^+ outside the particle. In contrast, the simulation of our path altering mechanism does not show the large capacity loss between delithiation and lithiation, which is a better explanation for the variation of phase transition for NMC111.

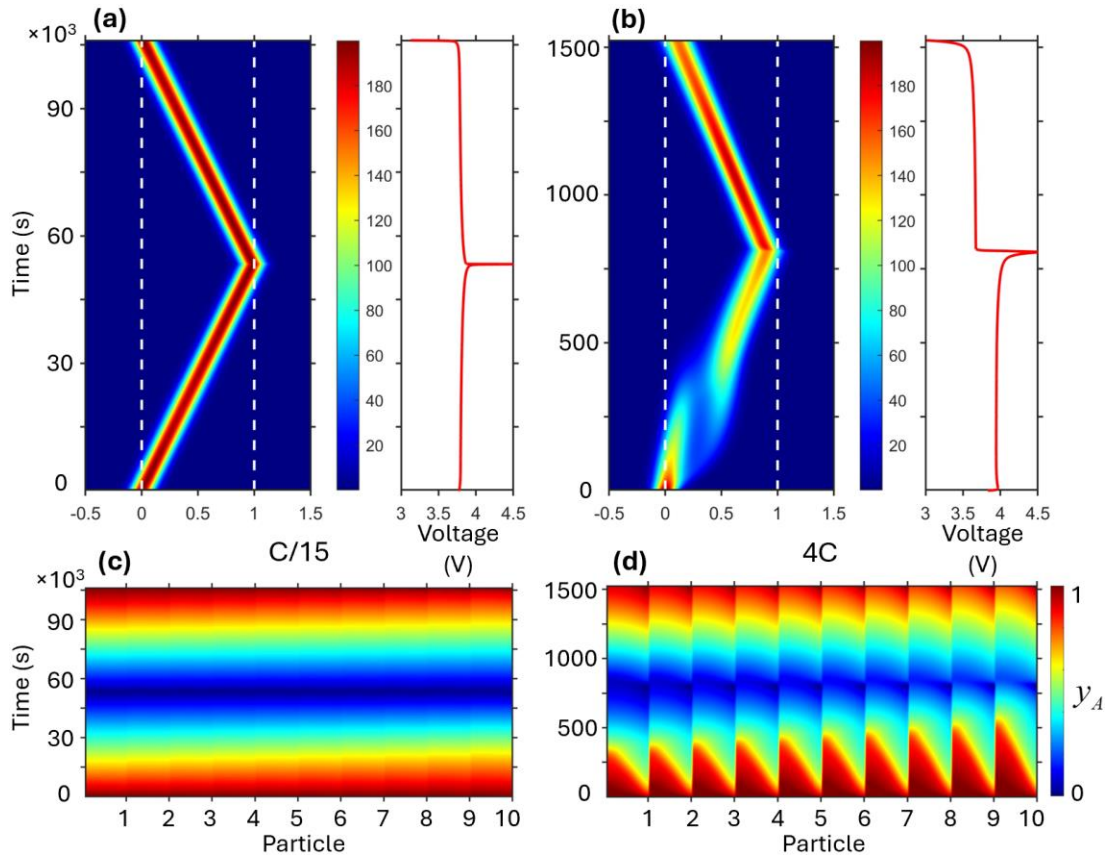


Figure 3.7 Simulated XRD graphs and electrical potentials for NMC111 multi-particles under (a) C/15 and (b) 4C cycles. The XRD peak location 0 and 1 indicate the lattice parameters of fully lithiated and fully delithiated equilibrium state, respectively. The Li⁺ fraction profiles in ten particles with different sizes that obey the log-normal distribution (mean size 186nm, standard deviation 0.15) are shown in (c) for C/15 and (d) for 4C cycles. All particles are scaled to the same nondimensionalized size. Larger particles are marked by larger numbers. Based on the symmetry, all particles are simulated in half. The left end and the right end are respectively the center and the surface of every particle.

3.3 Conclusion

In this study, we have presented a mechanism to explain the variations of phase transition for LFP and layered oxides systems under non-equilibrium process. The core of the mechanism are the factors that alter the paths of free energy change during (de)lithiation, which are called path factors. Path factors assemble the terms of free energy within a multi-layered structure. The path factors in every layer are determined by states α and β whose physical meaning are different for different layers. The multi-layered states include Li-rich/Li-poor, delithiation/lithiation, equilibrium/non-equilibrium, and order/disorder structure, which are described using a series of order parameters. The total free energy of the systems includes different terms upon Li^+ fraction, mechanical strain, dislocation density, and the order parameters, which are called main parameters. The dislocation density is a conserved quantity that includes the information of dislocation orientation. The process of generation or annihilation of dislocations on the particle surface is called dislocation reaction, which is coupled with the electrochemical reaction. Increased electrochemical reaction rate results in increased dislocation reaction rate and then increases the free energy of the system. To minimize the total free energy of particles, the path factors spontaneously alter the path of energy change for (de)lithiation, during which the fields of main parameters change continuously. Compared to other main parameters, dislocation density plays the most significant role in selecting the path since it dominates the free energy change. The governing equations for the kinetics of main parameters are solved using finite difference method. Our simulation includes the parts of neglecting and including the diffusion limit of Li^+ . Without the influence of diffusion limit, the path altering for (de)lithiation is clearly displayed in the evolution curves of main parameters versus Li^+ fraction. To validate the path altering mechanism for the variation of phase transition, the simulations

with the diffusion limit of Li^+ are compared to existing experimental observations. For LFP multi-particles, XRD graphs and Li^+ fraction phase fields are simulated for the galvanostatic cycles with 5C/10C/20C, and the 90 seconds 10C delithiation followed by 270 seconds open circuit relaxation. The order-disorder coexistence for LFP is simulated for a single LFP particle under the potentiostatic delithiation with 4V vs Li/Li^+ . For NMC111, we simulated the XRD graphs and the Li^+ fraction phase fields for C/15 and 4C cycles. All above simulation results for LFP and NMC111 well agree with the existing experimental observations, which validate our path altering mechanism for the variations of phase transitions. The dislocation induced path altering supplies potential strategies to improve or optimize the performance of Li-ion batteries. For example, the coefficients for the coupling between dislocation reaction and electrochemical reaction, or the initial dislocation density may be adjusted or optimized by using surface engineering methods. The development of defect engineering [35] [36] [37] may supply more potential approaches to control the dislocations in electrode particles and then adjust the layered material states following the path altering mechanism. Besides the four layers of states modeled in this study, the nested energy formulation can be expanded to an arbitrary number of layers for revealing more details or different phenomena. Our path altering mechanism is a generalized method that clarifies the variations of state changes for electrode materials.

CHAPTER 4

Modeling and Simulation of the Non-equilibrium Process for a Continuous Solid Solution System in Lithium-ion Batteries

This chapter considers the electrode of a Li-ion battery as a solid solution system. Based on continuum mechanics, non-equilibrium thermodynamics and variational theory, we develop a generalized theory to describe the variations of stress distribution, electrode material deformation and lithium-ion fractions of the solid solution system over a non-equilibrium process. The finite deformation, mass transfer, phase transformation, chemical reaction and electrical potential of the system are coupled with each other in a fully self-consistent formulation. We apply the developed theory to numerically simulate a Sn anode particle using the finite difference method. Our results compare the influences of different C-rates on the non-equilibrium process of the anode particle.

The contents in this chapter are reproduced based on the published work below,
Hongjiang Chen, Hsiao-Ying Shadow Huang, “Modeling and simulation of the non-equilibrium process for a continuous solid solution system in lithium-ion batteries”, *International Journal of Solids and Structures*, Volume 212, 2021, Pages 124-142, ISSN 0020-7683,
<https://doi.org/10.1016/j.ijsolstr.2020.11.014>.

4.1 Modeling Method

4.1.1 General theory

The electrodes of Li-ion batteries can be considered as continuous solid solution systems, in which every component has finite deformation due to the volume change and mass transfer during (dis)charging. In this chapter, the finite deformation of an electrode system is formulated based on metric tensor [94] instead of deformation gradient tensor. The deformed configurations of the solution components in the electrode are considered as deformed metric spaces with curvilinear coordinate frames, where the components of tensors generally could be covariant or contravariant. The concepts of metric tensor and covariant/contravariant components of tensors are briefly introduced in APPENDIX B.1. Some terminologies and tensor indices are defined below: Reference space is used to refer to a metric space selected for describing the components and basis of tensors. The operators and the tensor components are for the reference space unless otherwise specified. Lab space is used to refer to an inertial Euclidean space with a static metric. Moreover, lowercase English letters, uppercase English or Greek letters are used in superscripts/subscripts in this chapter, and details are as follows:

- a. Lowercase English letters. If there is no bracket, these items are the tensors' spatial indices, and they obey Einstein's summation convention. Superscripts indicate contravariant components, and subscripts indicate covariant components.
- b. Uppercase English or Greek letters. Normal superscripts/subscripts of a variable. They are not indices and do not obey Einstein's summation convention.
- c. Within brackets. Indices that do not obey Einstein's summation convention.

4.1.1.1 Mass conservation and kinematics of continuums for solution systems

A solution system is composed of different matter components k . Every component corresponds to an individual continuous metric space, which can move and deform following the movement of a corresponding component relative to a static space. In general, due to the movement of the components, the coordinate frames of the corresponding spaces are curvilinear. We may select the metric space corresponding to any component as the reference space, in which the Lagrangian coordinate is used for the selected component and the Eulerian coordinate is used for all other components. In this chapter, the term “velocity” is the velocity relative to the selected reference space unless otherwise specified. In addition, the lab space is necessary for describing the deformation of a solution system.

Based on mass conservation, the divergence theorem and the chain rule yield Equation (4.1.1) used for the density change in component k . The derivation steps are shown in APPENDIX B.2. As shown in Equation (4.1.1), the local change rate in the density for component k is caused by the convective change rate of the density $\nabla \cdot (\rho_{(k)} \mathbf{v}_{(k)})$, the deformation of the reference space $\nabla \cdot \mathbf{y}$, and local chemical reactions $\sum_j \xi_{(k)}^{(j)} J^{(j)}$.

$$\frac{\partial \rho_{(k)}}{\partial t} + \nabla \cdot (\rho_{(k)} \mathbf{v}_{(k)}) + \rho_{(k)} \nabla \cdot \mathbf{y} = \sum_j \xi_{(k)}^{(j)} J^{(j)}, \quad (4.1.1)$$

where $\rho_{(k)}$ is the mass density of component k , $\mathbf{v}_{(k)}$ is the velocity of component k in the solution system, $\nabla \cdot$ is divergence operator, \mathbf{y} is the velocity of the reference space relative to the lab space, $\xi_{(k)}^{(j)}$ is the mass stoichiometric ratio of component k in chemical reaction j , which

is less than zero for the components on the left of the chemical equation, and $J^{(j)}$ is the chemical reaction mass rate of reaction j .

To describe the diffusion of components in a solution system, we introduce a mass center continuum for the solution system, in which the density and velocity are defined as follows:

$$\rho = \sum_k \rho_{(k)} \quad \text{and} \quad (4.1.2)$$

$$\rho \mathbf{v} = \sum_k \rho_{(k)} \mathbf{v}_{(k)}, \quad (4.1.3)$$

where ρ and \mathbf{v} are the density and the velocity of the mass center continuum, which are called the mass center density and the mass center velocity, respectively [94].

The diffusion flux and the mass fraction of component k are defined as follows:

$$\mathbf{J}_{(k)} = \rho_{(k)} (\mathbf{v}_{(k)} - \mathbf{v}) \quad \text{and} \quad (4.1.4)$$

$$x_{(k)} = \rho_{(k)} / \rho, \quad (4.1.5)$$

where $\mathbf{J}_{(k)}$ and $x_{(k)}$ are the flux and the mass fraction of component k , respectively [94].

With Equations (4.1.2) and (4.1.3), summing (4.1.1) for all the k components yields Equation (4.1.6), which describes the density change of the mass center continuum. Because all the components satisfy the conditions for mass conservation, the mass center continuum is also mass conserved. The chemical reactions are mass-conserved, and hence are canceled by the summation, as shown in Equation (4.1.6):

$$\frac{\partial \rho}{\partial t} + \nabla \cdot (\rho \mathbf{v}) + \rho \nabla \cdot \mathbf{z} = 0. \quad (4.1.6)$$

Combining Equations (4.1.6) and (4.1.1) yields Equation (4.1.7) with Equation (4.1.8) below for the changing rate of the mass fraction:

$$\rho \dot{\mathbf{x}}_{(k)} + \nabla \cdot \mathbf{J}_{(k)} = \sum_j \xi_{(k)}^{(j)} \mathbf{J}^{(j)} \quad \text{and} \quad (4.1.7)$$

$$\dot{\mathbf{x}}_{(k)} = \frac{d\mathbf{x}_{(k)}}{dt}, \quad (4.1.8)$$

where $\dot{}$ is the operator of rate, and $\frac{d}{dt}$ is the total derivative operator over time of a tensor's components for fixed mass center coordinates. In the selected reference space, the total derivatives for functions of coordinate z^i and time t are calculated by the Equation (4.1.9) below,

$$\frac{d}{dt} = \frac{\partial}{\partial t} + v^i \frac{\partial}{\partial z^i} \quad (4.1.9)$$

where v^i is the contravariant component of the mass center velocity and z^i is the contravariant coordinate of the selected reference space.

The covariant component of the strain tensor for a continuum is defined as half of the change in the covariant component of the metric for the corresponding space [94]. Equation (4.1.10) shows the strain of the mass center continuum:

$$\hat{\varepsilon}_{ij} = \frac{1}{2} (\hat{g}_{ij} - g^{\circ}_{ij}), \quad (4.1.10)$$

where $\hat{\varepsilon}_{ij}$ is the covariant component of the strain tensor for the mass center continuum. $\hat{}$ indicates that the component corresponds to the mass center space, \hat{g}_{ij} is the covariant component of the metric tensor of the deformed mass center space, and g°_{ij} is the covariant component of the metric tensor for the initial mass center space. Above metric-based definition of strain for the finite deformation can be applied to the strains in different categories [94]:

elastic strain, thermal strain, plastic strain, concentration strain, etc. As proved in APPENDIX B.1, the strain tensor defined by Equation (4.1.10) is equivalent to the Green strain tensor.

The total strain may be composed of multiple strains with different categories, which can be elastic, plastic, creep, etc. For the mass center continuum, within the mass center space, the covariant component of the total strain is the summation of the covariant components of the strains in all categories [94], as shown in Equation (4.1.11):

$$\hat{\varepsilon}_{ij} = \sum_l \hat{\varepsilon}_{ij}^{(l)}, \quad (4.1.11)$$

where $\hat{\varepsilon}_{ij}^{(l)}$ is the component of the strain for the mass center space with category l , and the category may be elastic, plastic, creep, etc. Based on the metric-based definition of strain demonstrated by Equation (4.1.10), the additive decomposition of strain component shown by Equation (4.1.11) is valid for the finite deformation and consistent with the multiplicative decomposition of deformation gradient, which is proved in APPENDIX B.1. Please note that only the covariant components in Lagrangian coordinates satisfy the additive decomposition of strain component [94].

4.1.1.2 Momentum equation and energy equation

The Cauchy stress in a solution system represents the statistical average of the atom interaction in the system [87]. As the atoms of all the components are indistinguishable on continuous scale, the Cauchy stress is related to the acceleration of the mass center continuum using the momentum equation as shown below [96],

$$\rho \mathbf{a}^L = \nabla \cdot \mathbf{p} + \sum_k \rho_{(k)} \mathbf{F}_{(k)}^L, \quad (4.1.12)$$

where \mathbf{a}^L is the acceleration of the mass center continuum relative to the lab space, \mathbf{p} is the Cauchy's stress tensor of the solution system, and $\mathbf{F}_{(k)}^L$ is the specific body force of component k in the lab space.

In the reference space, \mathbf{a}^L is calculated using Equation (4.1.13):

$$\mathbf{a}^{Li} = \frac{\partial v^{Li}}{\partial t} + v^{Lk} \nabla_k v^{Li}, \quad (4.1.13)$$

where a^{Li} is the contravariant component of \mathbf{a}^L , v^{Li} is the contravariant component of \mathbf{v}^L , which is the velocity of the mass center continuum relative to the lab space, and ∇_k is the operator of the covariant derivative.

The evolution of the solution system obeys the 1st law of thermodynamics. The energy equation of the system is formulated using the generalized D'Alembert principle below:

$$\delta \int_V u \rho dV = \int_V \delta q \rho dV + \int_V \sum_k \rho_{(k)} \mathbf{F}_{(k)}^L \cdot \delta \mathbf{r}_{(k)}^L dV + \delta W_a + \int_A \mathbf{p} \cdot \mathbf{n} \cdot \delta \mathbf{r}^L dA, \quad (4.1.14)$$

where u is the specific internal energy of the mass center continuum, V is the volume of the solution system, q is the specific heat of the mass center continuum, $\delta \mathbf{r}_{(k)}^L$ is the variational of the radius vector for component k in the lab space, δW_a is the total virtual work of inertia force in the system, \mathbf{n} is the normal vector for the surface of the solution system, $\delta \mathbf{r}^L$ is the variational of the radius vector for the mass center continuum in the lab space, and A is the surface area of the solution system.

On the continuous scale, we use the mass center continuum to represent the entire solution system. The mass center density and the mass center velocity are considered as the density and the velocity of the system, respectively. Hence, we use the mass center continuum to calculate the virtual work of the inertia force in Equation (4.1.14), as shown below:

$$\delta W_a = \int_V -\rho \mathbf{a}^L \cdot \delta \mathbf{r}^L dV . \quad (4.1.15)$$

4.1.1.3 Equation of the entropy production rate

The evolution of a solution system satisfies the 2nd law of thermodynamics. Under nonequilibrium thermodynamics, the entropy production rate is composed of a series of generalized thermodynamic flows and forces that describe the system at non-equilibrium [96]. The derivation of the entropy production rate is based on the description of the internal energy. The solution system is represented by its mass center continuum, of which the total internal energy is a functional of the specific internal energy, which is shown in Equation (4.1.16):

$$U = \int_m u \left(s, \hat{\boldsymbol{\varepsilon}}_{ij}^{(l)}, \hat{\nabla}_k \hat{\boldsymbol{\varepsilon}}_{ij}^{(l)}, x_{(k)}, \hat{\nabla}_i x_{(k)} \right) dm , \quad (4.1.16)$$

where U is the total internal energy of the solution system, s is specific entropy, $\hat{\nabla}_i$ is the operator of the covariant derivative in the mass center space, and m is the mass of the solution system.

The intensive thermodynamic functions of the solution system are defined as the functional derivatives of the total internal energy. With the mathematical relation between the functional derivatives and the partial derivatives, we define the homogeneous functions and inhomogeneous functions as shown below:

Temperature T is defined as follows:

$$T = \left(\frac{\delta U}{\delta s} \right)_{\boldsymbol{\varepsilon}, x} = \left(\frac{\partial u}{\partial s} \right)_{\boldsymbol{\varepsilon}, \nabla \boldsymbol{\varepsilon}, x, \nabla x} . \quad (4.1.17)$$

Stress with category l , $\boldsymbol{\sigma}^{(l)}$, is defined as follows:

$$\frac{1}{\rho} \hat{\sigma}^{(l)ij} = \left(\frac{\delta U}{\delta \hat{\epsilon}_{ij}^{(l)}} \right)_{s, \mathbf{e}^{(l \neq i)}, x} = \frac{1}{\rho} \hat{\sigma}_{HOM}^{(l)ij} - \hat{\nabla}_k \frac{1}{\rho} \hat{\sigma}_{INH}^{(l)ijk}. \quad (4.1.18)$$

With category l , the homogeneous stress $\hat{\sigma}_{HOM}^{(l)}$ and the inhomogeneous stress $\hat{\sigma}_{INH}^{(l)}$ are defined below, respectively:

$$\frac{1}{\rho} \hat{\sigma}_{HOM}^{(l)ij} = \left(\frac{\partial u}{\partial \hat{\epsilon}_{ij}^{(l)}} \right)_{s, \mathbf{e}^{(l \neq i)}, \nabla \mathbf{e}, x, \nabla x} \quad \text{and} \quad (4.1.19)$$

$$\frac{1}{\rho} \hat{\sigma}_{INH}^{(l)ijk} = \left(\frac{\partial u}{\partial \hat{\nabla}_k \hat{\epsilon}_{ij}^{(l)}} \right)_{s, \mathbf{e}, \nabla \mathbf{e}^{(l \neq i)}, x, \nabla x}. \quad (4.1.20)$$

The category l can be elastic, plastic, creep, etc. The chemical potential of component k relative to component K is defined by

$$\mu_{(kK)} = \left(\frac{\delta U}{\delta x_{(k)}} \right)_{s, \mathbf{e}, x_{(k' \neq k)}} = \mu_{HOM(kK)} - \hat{\nabla}_i \hat{\mu}_{INH(kK)}^i, \quad (4.1.21)$$

where the homogeneous relative chemical potential $\mu_{HOM(kK)}$ and inhomogeneous relative chemical potential $\hat{\mu}_{INH(kK)}$ are respectively defined by:

$$\mu_{HOM(kK)} = \left(\frac{\partial u}{\partial x_{(k)}} \right)_{s, \mathbf{e}, \nabla \mathbf{e}, x_{(k' \neq k)}, \nabla x} \quad \text{and} \quad (4.1.22)$$

$$\hat{\mu}_{INH(kK)}^i = \left(\frac{\partial u}{\partial \hat{\nabla}_i x_{(k)}} \right)_{s, \mathbf{e}, \nabla \mathbf{e}, x, \nabla x_{(k' \neq k)}}. \quad (4.1.23)$$

Based on the definitions of the intensive functions above, we find Equations (4.1.24), (4.1.25), (4.1.26), (4.1.27), and (4.1.28) for the entropy production rate by combining the conservation Equation (4.1.7), the energy Equation (4.1.14), and the divergence theorem. The derivation steps are shown in APPENDIX B.3. With Equation (4.1.24), we have the generalized

thermodynamic flows \mathbf{J}_s , $\boldsymbol{\tau}^{(l)}$, $\mathbf{J}_{(k)}$, and $J^{(j)}$, and generalized thermodynamic forces ∇T , $\dot{\boldsymbol{\epsilon}}^{(l)}$, $\nabla\Psi_{(kK)}^L$, and $A_C^{(j)}$ [96]. The generalized thermodynamic flows can be expressed as functions of the generalized thermodynamic forces. Their models for a simplified case are shown in Section 4.1.2.2.

$$T\theta = -\mathbf{J}_s \cdot \nabla T + \sum_l \boldsymbol{\tau}^{(l)} : \dot{\boldsymbol{\epsilon}}^{(l)} - \sum_k^{K-1} \mathbf{J}_{(k)} \cdot \nabla \Psi_{(kK)}^L + \sum_j J^{(j)} A_C^{(j)} \quad (4.1.24)$$

$$\boldsymbol{\tau}^{(l)} = \mathbf{p} - \boldsymbol{\sigma}^{(l)} \quad (4.1.25)$$

$$\Psi_{(kK)}^L = \mu_{(kK)} + \varphi_{(kK)}^L \quad (4.1.26)$$

$$\mathbf{F}_{(kK)}^L = \mathbf{F}_{(k)}^L - \mathbf{F}_{(K)}^L = -\nabla \varphi_{(kK)}^L, \text{ and} \quad (4.1.27)$$

$$A_C^{(j)} = -\sum_k^{K-1} \mu_{(kK)} \xi_{(k)}^{(j)}, \quad (4.1.28)$$

where θ is entropy production rate, \mathbf{J}_s is entropy flux, $\boldsymbol{\tau}^{(l)}$ is the dissipation stress with category l , $\dot{\boldsymbol{\epsilon}}^{(l)}$ is the strain rate with category l of the mass center continuum, $\mathbf{J}_{(k)}$ is the diffusion flux of component k , $\Psi_{(kK)}^L$ is the potential energy of component k relative to component K in the lab space, $A_C^{(j)}$ is the specific chemical affinity of reaction j , and $\varphi_{(kK)}^L$ is the potential energy corresponding to the body force in the lab space.

4.1.1.4 Constitutive relations of state functions

We selected T , $\boldsymbol{\epsilon}^{(l)}$, $\nabla \boldsymbol{\epsilon}^{(l)}$, $x_{(k)}$, and $\nabla x_{(k)}$ as the basic independent parameters to determine the status of a solution system. The other state functions of the solution system depend on these five parameters. To replace the specific entropy with the temperature as an independent

parameter of the state functions in Section 4.1.1.3, specific free energy a_F is introduced by

Equations (4.1.29) and (4.1.30):

$$a_F = u - Ts \quad (4.1.29)$$

and

$$da_F = -sdT + \sum_l \frac{1}{\rho} \hat{\sigma}_{HOM}^{(l)ij} d\hat{\varepsilon}_{ij}^{(l)} + \sum_l \frac{1}{\rho} \hat{\sigma}_{INH}^{(l)ijk} d\hat{\nabla}_k \hat{\varepsilon}_{ij}^{(l)} + \sum_k \mu_{HOM(kK)} dx_{(k)} + \sum_k \hat{\mu}_{INH(kK)}^i d\hat{\nabla}_i x_{(k)}. \quad (4.1.30)$$

We assume that the 2nd order partial derivatives of a_F is continuous. The homogeneous and inhomogeneous stresses are therefore a continuous function of T , $\boldsymbol{\varepsilon}^{(l)}$, $\nabla \boldsymbol{\varepsilon}^{(l)}$, $x_{(k)}$, and $\nabla x_{(k)}$.

It is assumed that there is no crossed coupling between different categories of the

(in)homogeneous stresses, i.e., $\left(\frac{\partial(\hat{\sigma}_{HOM}^{(l)ij} / \rho)}{\partial \hat{\varepsilon}_{kl}^{(h)}} \right)_{l \neq h} = 0$, $\left(\frac{\partial(\hat{\sigma}_{HOM}^{(l)ij} / \rho)}{\partial \hat{\nabla}_m \hat{\varepsilon}_{pq}^{(h)}} \right)_{l \neq h} = 0$,

$\left(\frac{\partial(\hat{\sigma}_{INH}^{(l)ijk} / \rho)}{\partial \hat{\varepsilon}_{pq}^{(h)}} \right)_{l \neq h} = 0$, and $\left(\frac{\partial(\hat{\sigma}_{INH}^{(l)ijk} / \rho)}{\partial \hat{\nabla}_m \hat{\varepsilon}_{pq}^{(h)}} \right)_{l \neq h} = 0$. The homogeneous and inhomogeneous

stresses with category l satisfy Equations (4.1.31) and (4.1.32):

$$d \left(\frac{\hat{\sigma}_{HOM}^{(l)ij}}{\rho} \right) = \hat{C}_{\rho}^{(l)ijkl} d\hat{\varepsilon}_{kl}^{(l)} + \hat{C}_{\rho \nabla}^{(l)ijrsp} d\hat{\nabla}_p \hat{\varepsilon}_{rs}^{(l)} + \sum_k \hat{\kappa}_{(kK)}^{(l)ij} dx_{(k)} + \sum_k \hat{\kappa}_{\nabla(kK)}^{(l)ijq} d\hat{\nabla}_q x_{(k)} + \hat{\gamma}^{(l)ij} dT \quad (4.1.31)$$

and

$$d \left(\frac{\hat{\sigma}_{INH}^{(l)ijk}}{\rho} \right) = \hat{\Lambda}^{(l)ijklm} d\hat{\varepsilon}_{lm}^{(l)} + \hat{\Lambda}_{\nabla}^{(l)ijklmp} d\hat{\nabla}_p \hat{\varepsilon}_{lm}^{(l)} + \sum_k \hat{\omega}_{(kK)}^{(l)ijk} dx_{(k)} + \sum_k \hat{\omega}_{\nabla(kK)}^{(l)ijkq} d\hat{\nabla}_q x_{(k)} + \hat{\chi}^{(l)ijk} dT, \quad (4.1.32)$$

where $\hat{C}_{\rho}^{(l)ijkl}$, $\hat{C}_{\rho \nabla}^{(l)ijrsp}$, $\hat{\kappa}_{(kK)}^{(l)ij}$, $\hat{\kappa}_{\nabla(kK)}^{(l)ijq}$, $\hat{\gamma}^{(l)ij}$, $\hat{\Lambda}^{(l)ijklm}$, $\hat{\Lambda}_{\nabla}^{(l)ijklmp}$, $\hat{\omega}_{(kK)}^{(l)ijk}$, $\hat{\omega}_{\nabla(kK)}^{(l)ijkq}$, and $\hat{\chi}^{(l)ijk}$ are the

components of the coefficient tensors.

Similarly, the relative chemical potentials are continuous functions of T , $\boldsymbol{\varepsilon}^{(l)}$, $\nabla\boldsymbol{\varepsilon}^{(l)}$, $\boldsymbol{x}_{(k)}$, and $\nabla\boldsymbol{x}_{(k)}$. They satisfy Equations (4.1.33) and (4.1.34):

$$d\mu_{HOM(kK)} = -\left(\frac{\partial s}{\partial \boldsymbol{x}_{(k)}}\right)_{T,\dots} dT + \sum_l \hat{\boldsymbol{\kappa}}_{(kK)}^{(l)ij} d\hat{\boldsymbol{\varepsilon}}_{ij}^{(l)} + \sum_l \hat{\boldsymbol{\omega}}_{(kK)}^{(l)ijk} d\hat{\nabla}_k \hat{\boldsymbol{\varepsilon}}_{ij}^{(l)} + \sum_h^{K-1} \Xi^{(kh)} dx_{(h)} + \sum_h^{K-1} \hat{l}_{(kKh)}^i d\hat{\nabla}_i x_{(h)} \quad (4.1.33)$$

and

$$d\hat{\mu}_{INH(kK)}^i = -\left(\frac{\partial s}{\partial \hat{\nabla}_i \boldsymbol{x}_{(k)}}\right)_{T,\dots} dT + \sum_l \hat{\boldsymbol{\kappa}}_{\nabla(kK)}^{(l)rsi} d\hat{\boldsymbol{\varepsilon}}_{rs}^{(l)} + \sum_l \hat{\boldsymbol{\omega}}_{\nabla(kK)}^{(l)rspi} d\hat{\nabla}_p \hat{\boldsymbol{\varepsilon}}_{rs}^{(l)} + \sum_{h=1}^{K-1} \left[\hat{l}_{(kKh)}^i dx_{(h)} + \frac{\partial^2 a_F}{\partial \hat{\nabla}_i \boldsymbol{x}_{(k)} \partial \hat{\nabla}_q \boldsymbol{x}_{(h)}} d\hat{\nabla}_q x_{(h)} \right], \quad (4.1.34)$$

where $\Xi^{(kh)}$ and $\hat{l}_{(kKh)}^i$ are the components of coefficient tensors.

Because of the symmetry of the 2nd order derivatives of a_F , coefficients $\hat{\boldsymbol{\kappa}}_{(kK)}^{(l)ij}$, $\hat{\boldsymbol{\omega}}_{(kK)}^{(l)ijk}$, $\hat{\boldsymbol{\kappa}}_{\nabla(kK)}^{(l)rsi}$, and $\hat{\boldsymbol{\omega}}_{\nabla(kK)}^{(l)rspi}$ appear in both expressions of $\boldsymbol{\sigma}^{(l)}$ and $\mu_{(kK)}$. The coefficients $\hat{\boldsymbol{\kappa}}_{(kK)}^{(l)ij}$, $\hat{\boldsymbol{\omega}}_{(kK)}^{(l)ijk}$, $\hat{\boldsymbol{\kappa}}_{\nabla(kK)}^{(l)rsi}$, and $\hat{\boldsymbol{\omega}}_{\nabla(kK)}^{(l)rspi}$ are named coupling coefficients of the mechanical-chemical coupling effect.

4.1.2 Simplification and application

The general theory in Section 4.1.1 may be applied to a simplified solution system that represents the tin anode particle in Li-ion batteries, based on the assumptions below: (1) This solution system is a binary system with isotropic materials. (2) The temperature of the system is constant and evenly distributed. (3) The body force is neglected. (4) The materials of the system have no memory effect. (5) Only the interstitial diffusion of Li^+ in the Sn anode is considered.

(6) The electrochemical reaction of the Sn anode occurs only on the surface of the solution system. (7) The electrical potential is evenly distributed on the particle.

In the tin anode, Li^+ diffuse through the sites around Sn atoms. The solution system has two components, Li^+ and Sn. We define three continuums: the Li^+ continuum, Sn continuum and the mass center continuum. All three continuums have their corresponding deformed spaces. Li^+ is defined as component 1 and Sn is defined as component 2. If there is no index of components marked in a function, that function is for the mass center continuum.

4.1.2.1 Mass conservation and kinematics

The boundary of the anode is determined by the boundary of the Sn continuum. For the convenience of setting the boundary conditions, we select the space of the Sn (component 2) as the reference space, of which the independent variables for the functions are (z^1, z^2, z^3, t) , where z^i is the Eulerian coordinate of the mass center continuum and the Lagrangian coordinate of the Sn continuum.

Selecting the Sn space as the reference space means that $\mathbf{v}_{(2)} = \mathbf{0}$. The solution system is assumed to be a binary system. This system yields a simplified form of Equation (4.1.4), as shown in Equation (4.1.35) below,

$$\mathbf{J}_{(1)} = \rho_{(2)} \mathbf{v}. \quad (4.1.35)$$

Substituting Equation (4.1.35) into Equation (4.1.7), with the assumption that there is no chemical reaction inside the system, yields the mass conservation equation:

$$\rho \dot{x}_{(1)} + \nabla \cdot (\rho_{(2)} \mathbf{v}) = 0. \quad (4.1.36)$$

For the binary system, the molar fraction and the mass fraction are related by Equation (4.1.37):

$$y'_{(1)} = \frac{M_{(2)} x_{(1)}}{N_B M_{(1)} x_{(2)}}, \quad (4.1.37)$$

where $y'_{(1)}$ is the molar fraction of the occupied Li^+ sites, $M_{(1)}$ is the molar mass of Li^+ , $M_{(2)}$ is the molar mass of Sn, and N_B is the average number of Li^+ per Sn when the anode is fully lithiated.

We define the current density of lithiation as positive. The total current of the anode particle is as follows:

$$I = -F \int_A \frac{1}{M_{(1)}} \rho \mathbf{v} \cdot \mathbf{n} dA, \quad (4.1.38)$$

where \mathbf{n} is the normal vector of the surface.

Since only the interstitial diffusion is considered, we assume that the elastic strain and plastic strain rate of the anode particle are contributed from the Sn atoms, as shown in Equations (4.1.39) and (4.1.40):

$$\boldsymbol{\varepsilon}^{(e)} = \boldsymbol{\varepsilon}_{(2)}^{(e)} \quad (4.1.39)$$

and

$$\dot{\boldsymbol{\varepsilon}}^{(p)} = \dot{\boldsymbol{\varepsilon}}_{(2)}^{(p)}, \quad (4.1.40)$$

where $\boldsymbol{\varepsilon}^{(e)}$ is the elastic strain of the mass center continuum, $\boldsymbol{\varepsilon}_{(2)}^{(e)}$ is the elastic strain of the Sn continuum, $\dot{\boldsymbol{\varepsilon}}^{(p)}$ is the plastic strain rate of the mass center continuum, and $\dot{\boldsymbol{\varepsilon}}_{(2)}^{(p)}$ is the plastic strain rate of the Sn continuum. In addition, we assume that the Sn continuum has only elastic deformation and plastic deformation. Since the reference space is the Lagrangian space of the Sn continuum, the additive decomposition of strain component demonstrated by Equation (4.1.11)

yields three kinematic relations for the Sn continuum, as shown in Equations (4.1.41), (4.1.42), and (4.1.43):

$$\varepsilon_{(2)ij} = \varepsilon_{(2)ij}^{(e)} + \varepsilon_{(2)ij}^{(p)} \quad (4.1.41)$$

$$\dot{\varepsilon}_{(2)ij} = \frac{1}{2} \left(\nabla_i v_{(2)j}^L + \nabla_j v_{(2)i}^L \right) = \frac{\partial \varepsilon_{(2)ij}}{\partial t} = \frac{1}{2} \frac{\partial g_{(2)ij}}{\partial t} \quad (4.1.42)$$

$$\dot{\varepsilon}_{(2)ij}^{(p)} = \frac{\partial \varepsilon_{(2)ij}^{(p)}}{\partial t}, \quad (4.1.43)$$

where $\varepsilon_{(2)ij}$ is the covariant component for the total strain of the Sn continuum, $\varepsilon_{(2)ij}^{(e)}$ is the covariant component for the elastic strain of the Sn continuum, $\varepsilon_{(2)ij}^{(p)}$ is the covariant component for the plastic strain of the Sn continuum, $\dot{\varepsilon}_{(2)ij}$ is the covariant component for the total strain rate of the Sn continuum, $v_{(2)j}^L$ is the covariant component for the velocity of the Sn continuum relative to the lab space, $g_{(2)ij}$ is the metric of the Sn space, and $\dot{\varepsilon}_{(2)ij}^{(p)}$ is the covariant component for the plastic strain rate of the Sn continuum. By substituting Equations (4.1.39), (4.1.40), and (4.1.41) into Equation (4.1.42), we have the relations between the deformation of the mass center continuum and the deformation of the Sn continuum as shown below,

$$\frac{\partial \varepsilon_{ij}^{(e)}}{\partial t} + \dot{\varepsilon}_{ij}^{(p)} = \frac{1}{2} \left(\nabla_i v_{(2)j}^L + \nabla_j v_{(2)i}^L \right) \quad (4.1.44)$$

and

$$\frac{\partial \varepsilon_{ij}^{(e)}}{\partial t} + \dot{\varepsilon}_{ij}^{(p)} = \frac{1}{2} \frac{\partial g_{(2)ij}}{\partial t}. \quad (4.1.45)$$

The constitutive equations for the finite deformation should be formulated based on rate functions. For the mass center continuum, the elastic strain rate is connected to its elastic strain by Equation (4.1.46) [94]:

$$\dot{\epsilon}_{ij}^{(e)} = \frac{\partial \epsilon_{ij}^{(e)}}{\partial t} + \epsilon_{kj}^{(e)} \frac{\partial v^k}{\partial z^i} + \epsilon_{il}^{(e)} \frac{\partial v^l}{\partial z^j} + v^k \frac{\partial \epsilon_{ij}^{(e)}}{\partial z^k}, \quad (4.1.46)$$

where $\dot{\epsilon}_{ij}^{(e)}$ is the covariant component for the elastic strain rate of the mass center continuum and v^i is the contravariant component of the mass center velocity. The total strain rate of the mass center continuum depends on the mass center velocity relative to the lab space, which is equal to the mass center velocity relative to the reference space plus the velocity of the reference space relative to the lab space. It yields Equation (4.1.47):

$$\dot{\epsilon} = \frac{1}{2} \left[\nabla \mathbf{v} + (\nabla \mathbf{v})^T \right] + \frac{1}{2} \left[\nabla \mathbf{v}_{(2)}^L + (\nabla \mathbf{v}_{(2)}^L)^T \right], \quad (4.1.47)$$

where the first part $\frac{1}{2} \left[\nabla \mathbf{v} + (\nabla \mathbf{v})^T \right]$ is the mass center strain rate induced by diffusion, called diffusion-induced creep rate, and the second part is the mass center strain rate induced by the Sn continuum.

4.1.2.2 Dissipation models of non-equilibrium process

Equation (4.1.24) for the entropy production rate reveals 4 parts for the dissipation of the solution system: thermal, mechanical, diffusional, and chemical reactions. For the system with an evenly distributed temperature, thermal dissipation is canceled. The other three dissipations are modeled in this section.

Because there is no memory effect, $\sigma^{(p)} = \mathbf{0}$. The elastic stress is marked as σ . It yields as follows:

$$\tau^{(p)} = \mathbf{p} = \tau^{(e)} + \sigma. \quad (4.1.48)$$

The mechanical dissipation is assumed to be related to $\dot{\mathbf{e}}^{(p)}$ and $\dot{\mathbf{e}}^{(e)}$. Substituting Equation (4.1.48) into Equation (4.1.24) yields as follows:

$$T\theta_M = \boldsymbol{\sigma} : \dot{\mathbf{e}}^{(p)} + \boldsymbol{\tau}^{(e)} : (\dot{\mathbf{e}}^{(e)} + \dot{\mathbf{e}}^{(p)}), \quad (4.1.49)$$

where θ_M is the mechanical entropy production rate. For the term $\boldsymbol{\sigma} : \dot{\mathbf{e}}^{(p)}$, we describe the plastic strain rate with the classic form of the plasticity flow as follows:

$$\dot{\mathbf{e}}^{(p)} = 2\lambda^{(p)}\mathbf{S}^{(e)}, \quad (4.1.50)$$

where $\lambda^{(p)}$ is the coefficient of the plastic strain rate, which is called the plasticity rate in this chapter, and $\mathbf{S}^{(e)}$ is the deviatoric tensor of $\boldsymbol{\sigma}$.

Substituting Equation (4.1.50) into Equation (4.1.49) yields as follows:

$$T\theta_M = 2\lambda^{(p)}\psi + \boldsymbol{\tau}^{(e)} : (\dot{\mathbf{e}}^{(e)} + \dot{\mathbf{e}}^{(p)}) \quad (4.1.51)$$

with

$$\psi = \boldsymbol{\sigma} : \mathbf{S}^{(e)} = \mathbf{S}^{(e)} : \mathbf{S}^{(e)}. \quad (4.1.52)$$

Equation (4.1.51) reveals that ψ may be considered as a generalized force of the generalized flow $\lambda^{(p)}$. The function $\lambda^{(p)} = \lambda^{(p)}(\psi)$ is modeled by introducing the transition-state theory into the plasticity. Atoms should pass the transition state for causing plastic deformation. This mechanism is named kinetic plasticity and is shown below:

$$\lambda^{(p)} = \lambda^{(p)+} - \lambda^{(p)-}, \quad (4.1.53)$$

$$\lambda^{(p)\pm} = C^{(p)\pm} \exp\left(-\frac{E_A^{(p)\pm}}{RT}\right), \quad (4.1.54)$$

$$E_A^{(p)+} = a^{(p)}K_\psi\psi + E_{A0}^{(p)}, \text{ and} \quad (4.1.55)$$

$$E_A^{(p)-} = (a^{(p)} + 1)K_\psi\psi + E_{A0}^{(p)}, \quad (4.1.56)$$

where $\lambda^{(p)\pm}$ is forward/backward plasticity rate, $C^{(p)\pm}$ are pre-exponential factors of the forward/backward plasticity rate, $a^{(p)}$ is a symmetry coefficient of the plasticity rate, K_ψ is the stress-activation energy coefficient, and $E_{A0}^{(p)}$ is the reference activation energy of the plasticity rate.

During plastic deformation, when some atoms are passing the transition state from the old state to the new one, that event corresponds to the forward plasticity rate. Additionally, some atoms may go back to the old state from the new one. This event corresponds to the backward plasticity rate. The net plasticity rate is the difference between the forward plasticity rate and the backward plasticity rate. The probability of passing the transition state obeys the Boltzmann distribution with forward/backward activation energy. The forward/backward activation energy is assumed to be linear with the ψ .

The dissipation stress $\tau^{(e)}$ in Equation (4.1.51) is known as viscous stress. We assume it as follows:

$$\tau^{(e)} = \eta^{(e)} : \dot{\mathbf{e}}^{(e)} + \eta^{(p)} : \dot{\mathbf{e}}^{(p)}, \quad (4.1.57)$$

where $\eta^{(e)}$ and $\eta^{(p)}$ are the coefficients of viscosity related to elastic strain rate and plastic strain rate respectively. The existence of viscosities makes the non-equilibrium process stable. Solving the equations of the system may give divergent results if the coefficients of the viscosity are not carefully chosen.

The material is assumed to be isotropic. Hence, $\eta^{(e)}$ and $\eta^{(p)}$ have simplified forms related to the metric as follows:

$$\eta^{(e)ijkl} = \eta_H^{(e)} g_{(2)}^{ij} g_{(2)}^{kl} + \eta_D^{(e)} g_{(2)}^{ik} g_{(2)}^{jl} + \eta_D^{(e)} g_{(2)}^{il} g_{(2)}^{jk} \quad (4.1.58)$$

and

$$\eta^{(p)ijkl} = \eta_H^{(p)} g_{(2)}^{ij} g_{(2)}^{kl} + \eta_D^{(p)} g_{(2)}^{ik} g_{(2)}^{jl} + \eta_D^{(p)} g_{(2)}^{il} g_{(2)}^{jk}, \quad (4.1.59)$$

where $g_{(2)}^{ij}$ is the contravariant component of the metric tensor for the reference space, and $\eta_H^{(e)}$, $\eta_D^{(e)}$, $\eta_H^{(p)}$, and $\eta_D^{(p)}$ are material parameters.

Substituting Equation (4.1.50) into Equation (4.1.57) yields a simplified form of $\boldsymbol{\tau}^{(e)}$ by cancelling the $\eta_H^{(p)}$:

$$\boldsymbol{\tau}^{(e)} = \boldsymbol{\eta}^{(e)} : \dot{\mathbf{e}}^{(e)} + 4\eta_D^{(p)} \lambda^{(p)} \mathbf{S}^{(e)}. \quad (4.1.60)$$

For isotropic materials, the parameters are zero for the 1st and the 3rd order coefficient tensors [94]. Hence, for the diffusional dissipation, there should be no coupling between $\mathbf{J}_{(1)}$ and $A_C^{(j)}$, or between $\mathbf{J}_{(1)}$ and $\dot{\mathbf{e}}^{(l)}$. The body force is neglected. It yields as follows:

$$T\theta_{(1)} = -\mathbf{J}_{(1)} \cdot \nabla \mu_{(12)}, \quad (4.1.61)$$

where $\theta_{(1)}$ is the diffusional entropy production rate of the simplified system. The relation between $\mathbf{J}_{(1)}$ and $\nabla \mu_{(12)}$ is expressed as follow:

$$J_{(1)}^i = -\frac{L}{T} g_{(2)}^{ij} \nabla_j \mu_{(12)} \quad (4.1.62)$$

with

$$L = L_0 f_L(x_{(1)}), \quad (4.1.63)$$

where $J_{(1)}^i$ is the contravariant component of Li⁺ flux, L is the thermodynamic coefficient of diffusion, and L_0 is the reference thermodynamic coefficient of diffusion. Coefficient L depends on the mass fraction of Li⁺. According to Equations (4.1.4) and (4.1.5), $\mathbf{J}_{(1)}$ is zero when $x_{(1)}$ is

zero. Hence, L should be zero when $x_{(1)}$ is zero. Moreover, we assume that L is zero when the anode is fully lithiated.

We set lithiation as the forward reaction. The chemical reaction on the surface is as follows:



where Li^+ is the Li-ion from the electrolyte, e^- is the electron from the anode, and S^A indicates the site of Li^+ in the anode. The surface region may not be considered as the binary system since there are more than two components on the surface. We define the Li^+ from electrolyte as component 3.

The molar electrochemical potential of the Li^+ in the electrolyte is expressed as follows:

$$\mu_{(30)M} = \mu_{(32)}M_{(1)} + F\phi, \quad (4.1.65)$$

where $\mu_{(30)M}$ is the molar electrochemical potential of the Li-ion in the electrolyte, F is the Faraday's constant, and ϕ is the electrical potential based on the location of Li-ion. If the diffusivity of the Li-ion in the electrolyte is much higher than the diffusivity of Li^+ in the anode, we may consider the electrolyte to always be in equilibrium relative to the anode. Hence, $\mu_{(30)M}$ should be constant and evenly distributed in the electrolyte. Substituting Equation (4.1.65) into Equation (4.1.28) yields as follows:

$$A_{CM} = \mu_{(30)M} - (F\phi + \mu_{(12)}M_{(1)}), \quad (4.1.66)$$

where A_{CM} is the molar chemical affinity.

We define the molar reaction rate J_M with $J_M = J / M_{(1)}$. Based on the transition-state theory, the function $J_M = J_M(A_{CM})$ is modeled by Equations (4.1.67), (4.1.68), (4.1.69), and (4.1.70):

$$J_M = J_M^+ - J_M^-, \quad (4.1.67)$$

$$J_M^\pm = C^{(R)\pm} \exp\left(-\frac{E_A^{(R)\pm}}{RT}\right), \quad (4.1.68)$$

$$E_A^{(R)+} = a^{(R)} A_{CM} + E_{A0}^{(R)}, \text{ and} \quad (4.1.69)$$

$$E_A^{(R)-} = (a^{(R)} + 1) A_{CM} + E_{A0}^{(R)}, \quad (4.1.70)$$

where J_M^\pm is the forward/backward molar reaction rate, $C^{(R)\pm}$ is pre-exponential factors of the forward/backward molar reaction rate, $a^{(R)}$ is the symmetry coefficient of the molar reaction rate, and $E_{A0}^{(R)}$ is the reference activation energy of the molar reaction rate.

4.1.2.3 Models of state functions

For isotropic materials, \hat{C}_ρ^{ijkl} and $\hat{\kappa}_{(kK)}^{(l)ij}$ have simplified forms related to the metric tensor.

It yields as follows:

$$\hat{C}_\rho^{ijkl} = \lambda_\rho \hat{g}^{ij} \hat{g}^{kl} + G_\rho \hat{g}^{ik} \hat{g}^{jl} + G_\rho \hat{g}^{il} \hat{g}^{jk} \quad (4.1.71)$$

and

$$\hat{\kappa}_{(12)}^{ij} = \kappa \hat{g}^{ij}, \quad (4.1.72)$$

where κ is related to the expansion ratio defined by $\alpha_{ij} = \alpha \hat{g}_{ij} = \left(\frac{\partial \hat{\mathcal{E}}_{ij}^{(e)}}{\partial x_{(1)}} \right)_{\frac{\sigma_{HOM}}{\rho}}$. The chain rule

$$\frac{\partial}{\partial x_{(1)}} \left(\frac{\hat{\sigma}_{HOM}^{ij}}{\rho} \right)_{\hat{\mathcal{E}}_{kl}^{(e)}} = - \frac{\partial}{\partial \hat{\mathcal{E}}_{kl}^{(e)}} \left(\frac{\hat{\sigma}_{HOM}^{ij}}{\rho} \right)_{x_{(1)}} \left(\frac{\partial \hat{\mathcal{E}}_{kl}^{(e)}}{\partial x_{(1)}} \right)_{\frac{\sigma_{HOM}}{\rho}}$$
 yields the connection between κ and α :

$$\kappa = -(3\lambda_\rho + 2G_\rho)\alpha, \quad (4.1.73)$$

where α is related to the partial molar volume V_{PM} by

$$\alpha = \frac{1}{3} \frac{\rho V_{PM}}{M_{(1)} x_{(2)}}. \quad (4.1.74)$$

Since for isotropic materials, the parameters are zero for the 3rd and 5th order coefficient tensors [94], we can cancel the $\hat{C}_{\rho\nabla}^{(l)ijrsp}$, $\hat{K}_{\nabla(kK)}^{(l)ijq}$, $\hat{\Lambda}^{(l)ijklm}$, $\hat{\omega}_{(kK)}^{(l)ijk}$, and $\hat{\chi}^{(l)ijk}$ in Equations (4.1.31) and (4.1.32). There are 15 independent components for 6th order isotropic tensors [121]. With considering the symmetries of stress tensor and strain tensor, the number of the independent components for Λ_∇ decreases to six: $\Lambda_{\nabla(1)} \hat{g}^{ij} \hat{g}^{kp} \hat{g}^{lm}$, $\Lambda_{\nabla(2)} \hat{g}^{ij} \hat{g}^{kl} \hat{g}^{mp}$, $\Lambda_{\nabla(3)} \hat{g}^{ik} \hat{g}^{jl} \hat{g}^{mp}$, $\Lambda_{\nabla(4)} \hat{g}^{ik} \hat{g}^{jp} \hat{g}^{lm}$, $\Lambda_{\nabla(5)} \hat{g}^{il} \hat{g}^{jm} \hat{g}^{kp}$, and $\Lambda_{\nabla(6)} \hat{g}^{il} \hat{g}^{jp} \hat{g}^{km}$. For simplicity, $\hat{\Lambda}_{\nabla}^{ijklmp}$ and $\hat{\omega}_{\nabla(12)}^{ijkq}$ are expressed in only one component of them. Hence, we assume

$$\hat{\Lambda}_{\nabla}^{ijklmp} = \Lambda_\nabla \hat{g}^{ij} \hat{g}^{kp} \hat{g}^{lm} \quad \text{and} \quad (4.1.75)$$

$$\hat{\omega}_{\nabla(12)}^{ijkq} = \omega_\nabla \hat{g}^{ij} \hat{g}^{kq}. \quad (4.1.76)$$

By substituting Equations (4.1.75) and (4.1.76) into Equations (4.1.31) and (4.1.32),

Equation (4.1.18) yields the model of the objective elastic stress rate $\dot{\mathbf{\Omega}}$ as shown below,

$$\dot{\Omega}^{ij} = C_{\rho}^{ijkl} \rho \dot{\mathcal{E}}_{kl}^{(e)} - \sigma^{ij} \dot{e}_m^m + \kappa g_{(2)}^{ij} \rho \dot{x}_{(1)} + 2\rho (\nabla^2 f_{ex}) \dot{e}^{ij} - \rho g_{(2)}^{ij} \frac{d(\nabla^2 f_{ex})}{dt} \quad (4.1.77)$$

with

$$f_{\varepsilon x} = \Lambda_{\nabla} \varepsilon_m^{(e)m} + \omega_l x_{(1)}. \quad (4.1.78)$$

The relation between the objective elastic stress rate and the elastic stress is as follows

[94]:

$$\dot{\Omega}^{ij} = \frac{\partial \sigma^{ij}}{\partial t} - \sigma^{pj} \frac{\partial v^i}{\partial z^p} - \sigma^{iq} \frac{\partial v^j}{\partial z^q} + v^k \frac{\partial \sigma^{ij}}{\partial z^k}. \quad (4.1.79)$$

The relative chemical potential $\mu_{(12)}$ is divided into an ideal part and an excess part. The entropy of the ideal part obeys the ideal solution model [122]. We assume that specific entropy s is independent of $\nabla x_{(1)}$ and $\nabla \varepsilon^{(l)}$. Hence, combining Equations (4.1.21), (4.1.29), (4.1.30), (4.1.31), (4.1.33), and (4.1.34) yields the relative chemical potential model below. The derivation steps are shown in APPENDIX B.4.

$$\frac{\partial \mu_{EX(12)}}{\partial t} + v^k \frac{\partial \mu_{EX(12)}}{\partial z^k} = K_D \dot{\varepsilon}_m^{(e)m} + h \dot{x}_{(1)}, \quad (4.1.80)$$

$$\mu_{(12)} = RT \left[\frac{1}{M_{(1)}} \ln \frac{y'_{(1)}}{y'_{(2)}} - \frac{N_B}{M_{(2)}} \ln y'_{(2)} \right] - \omega_l \nabla^2 \varepsilon_m^{(e)m} - K_{(12)} \nabla^2 x_{(1)} + \mu_{EX(12)}, \quad (4.1.81)$$

$$K_D = \kappa - \frac{T}{x_{(2)}} \gamma, \text{ and} \quad (4.1.82)$$

$$\gamma = -(3\lambda_{\rho} + 2G_{\rho}) \alpha_T, \quad (4.1.83)$$

where $\mu_{EX(12)}$ is the excess relative chemical potential, h is the material parameter of the relative chemical potential, calculated by $h = k_{hRT} RT / M_{(2)}$, R is gas constant, $y'_{(2)}$ is the molar fraction of unoccupied Li^+ sites, $K_{(12)}$ is the material parameter of the relative chemical potential, and α_T is the thermal expansion ratio.

4.1.3 Numerical simulation

4.1.3.1 Transformation of equations and numerical method

For the convenience of simulating Sn anode particles, we transform the following equations into conducive forms for linearization: Equation (4.1.36) for mass conservation, the momentum Equation (4.1.12), the diffusion Equation (4.1.62), Equation (4.1.54) for the plasticity rate, Equation (4.1.68) for the chemical reaction rate, and Equation (4.1.81) for the relative chemical potential. The derivation steps of the transformation are shown in APPENDIX B.5. The transformed equations are shown below:

The equation for mass conservation is transformed into:

$$\begin{aligned} & \rho \dot{x}_{(1)} - \frac{L_0 R}{M_{(1)}} \left[f_{L1} \nabla^2 x_{(1)} + g_{(2)}^{ij} (\nabla_i f_{L1}) (\nabla_j x_{(1)}) \right] \\ & - \frac{L_0}{T} \left[f_L \nabla^2 \mu_{IE(12)} + g_{(2)}^{ij} (\nabla_i f_L) (\nabla_j \mu_{IE(12)}) \right] = 0 \end{aligned} \quad (4.1.84)$$

$$\text{with } f_L(x_{(1)}) = A_L (x_{(1)})^{N_1} (1 - x_{(1)})^{N_2} \left[1 - \left(\frac{M_{(2)}}{N_B M_{(1)}} + 1 \right) x_{(1)} \right]^{N_3}, \quad (4.1.85)$$

and

$$f_{L1}(x_{(1)}) = A_L (x_{(1)})^{N_1 - 1} (1 - x_{(1)})^{N_2 - 1} \left[1 - \left(\frac{M_{(2)}}{N_B M_{(1)}} + 1 \right) x_{(1)} \right]^{N_3 - 1}, \quad (4.1.86)$$

where $\mu_{IE(12)}$ is inhomogeneous and an excess part of the relative chemical potential and A_L , N_1 ,

N_2 , N_3 are material parameters related to f_L .

The momentum equation is transformed into:

$$\nabla_j p^{ij} = \rho \left(\frac{\partial v^i}{\partial t} + v^k \nabla_k v^i + \frac{\partial v_{(2)j}^L g_{(2)}^{ij}}{\partial t} + v_{(2)j}^L \nabla_k v_{(2)m}^L g_{(2)}^{kj} g_{(2)}^{mi} \right) \quad (4.1.87)$$

$$\text{with } p^{ij} = \sigma^{ij} + \left(\eta_H g_{(2)}^{ij} g_{(2)}^{kl} + 2\eta_D g_{(2)}^{ik} g_{(2)}^{jl} \right) \dot{e}_{kl}^{(e)} + 4\eta_D^{(p)} \lambda^{(p)} S^{(e)ij} . \quad (4.1.88)$$

The diffusion equation is transformed into:

$$\rho_{(2)} v^i = -L_0 g_{(2)}^{ij} \left[\frac{R}{M_{(1)}} f_{L1} \nabla_j x_{(1)} + \frac{f_L}{T} \nabla_j \mu_{IE(12)} \right] . \quad (4.1.89)$$

The equation for the plasticity rate is transformed into:

$$\frac{\partial \lambda^{(p)+}}{\partial t} = -\frac{a^{(p)} K_\psi}{RT} \lambda^{(p)+} \frac{\partial \psi}{\partial t} \quad \text{and} \quad (4.1.90)$$

$$\frac{\partial \lambda^{(p)-}}{\partial t} = -\frac{(a^{(p)} + 1) K_\psi}{RT} \lambda^{(p)-} \frac{\partial \psi}{\partial t} , \quad (4.1.91)$$

$$\text{with } \frac{\partial \psi}{\partial t} = 2 \left(S_{ij}^{(e)} \frac{\partial \sigma^{ij}}{\partial t} + S^{(e)ij} \sigma^{uv} \frac{\partial g_{(2)ui}}{\partial t} g_{(2)vj} \right) . \quad (4.1.92)$$

The equation for the chemical reaction rate is transformed into:

$$\frac{\partial J_M^+}{\partial t} = -\frac{a^{(R)}}{RT} J_M^+ \frac{\partial A_{CM}}{\partial t} \quad \text{and} \quad (4.1.93)$$

$$\frac{\partial J_M^-}{\partial t} = -\frac{a^{(R)} + 1}{RT} J_M^- \frac{\partial A_{CM}}{\partial t} , \quad (4.1.94)$$

$$\text{with } \frac{\partial A_{CM}}{\partial t} = - \left[F \frac{\partial \phi}{\partial t} + M_{(1)} \left(\frac{\partial \mu_{HL(12)}}{\partial x_{(1)}} \frac{\partial x_{(1)}}{\partial t} + \frac{\partial \mu_{IE(12)}}{\partial t} \right) \right] , \quad (4.1.95)$$

$$\frac{\partial \mu_{HL(12)}}{\partial x_{(1)}} = \frac{RT N_B}{M_{(2)}} \left[\frac{k}{x_{(1)}} - \frac{1}{x_{(2)}} + \frac{(k+1)^2}{1 - (k+1)x_{(1)}} \right] , \quad \text{and} \quad (4.1.96)$$

$$k = \frac{M_{(2)}}{N_B M_{(1)}} , \quad (4.1.97)$$

where $\mu_{HL(12)}$ is the homogeneous-logarithm relative chemical potential.

The equation for the relative chemical potential is transformed into:

$$\mu_{IE(12)} = -\omega_l \nabla^2 \varepsilon_m^{(e)m} - K_{(12)} \nabla^2 x_{(1)} + \mu_{EX(12)} . \quad (4.1.98)$$

For the numerical simulations, we have Equations (4.1.77), (4.1.73), (4.1.74), (4.1.78), (4.1.87), (4.1.88), (4.1.47), (4.1.53), (4.1.90), (4.1.91), (4.1.92), (4.1.44), (4.1.84), (4.1.85), (4.1.86), (4.1.8), (4.1.79), (4.1.46), (4.1.89), (4.1.80), (4.1.82), (4.1.98), (4.1.45), and (4.1.5). To make the number of variables equal to the number of equations, the four additional equations shown below are necessary:

$$\frac{\partial \rho_{(2)}}{\partial t} + \rho_{(2)} \nabla \cdot \mathbf{v}_{(2)}^{(L)} = 0 , \quad (4.1.99)$$

$$\left[g_{(2)ij} \right] = \left[g_{(2)}^{ij} \right]^{-1} , \quad (4.1.100)$$

$$\lambda_\rho = \lambda / \rho , \text{ and} \quad (4.1.101)$$

$$G_\rho = G / \rho , \quad (4.1.102)$$

where λ and G are Lamé constants.

We have 28 equations above with 28 variables below to numerically solve the non-equilibrium process of the Sn anode particle, namely, $\dot{\mathbf{Q}}, \kappa, \alpha, f_{\varepsilon x}, \mathbf{v}_{(2)}^L, \mathbf{p}, \dot{\mathbf{e}}, \lambda^{(P)}, \lambda^{(P)+}, \lambda^{(P)-}, \psi, \dot{\mathbf{e}}^{(e)}, \dot{x}_{(1)}, f_L, f_{L1}, x_{(1)}, \boldsymbol{\sigma}, \boldsymbol{\varepsilon}^{(e)}, \mathbf{v}, \mu_{EX(12)}, K_D, \mu_{IE(12)}, g_{(2)ij}, \rho, \rho_{(2)}, g_{(2)}^{ij}, \lambda_\rho,$ and G_ρ .

We apply the finite difference method coded with MATLAB to solve the equation set of the solution system numerically. We use a mesh generator program from Persson and Strang [123] to generate the grid of the discretized anode particle. The derivative matrices of the finite difference are built based on the method from Perrone and Kao [124]. We use the implicit method of finite difference scheme to keep the system numerically stable and convergent. System equations are solved in every time step. The equations of the solution system are

nonlinear. To reduce the computational cost, Newton's iteration is avoided at every time step. The equations are simply linearized by setting the variables as input coefficients for every time step if the variables are integrated over time in the simulation.

4.1.3.2 Geometry and material parameters of the particle

Figure 4.1a shows the initial spherical cap geometry of the anode particle bonded on a flat current collector, based on the size of the Sn particle observed in Takeuchi et al. [125]. To prevent stress concentration, the fillet is set on the connection between the current collector and the particle. We use the cylindrical coordinate frame (z^1, z^2, z^3) on the initial Sn space, where z^2 is the angle coordinate. The origin of the coordinate frame coincides with the spherical center of the spherical cap.

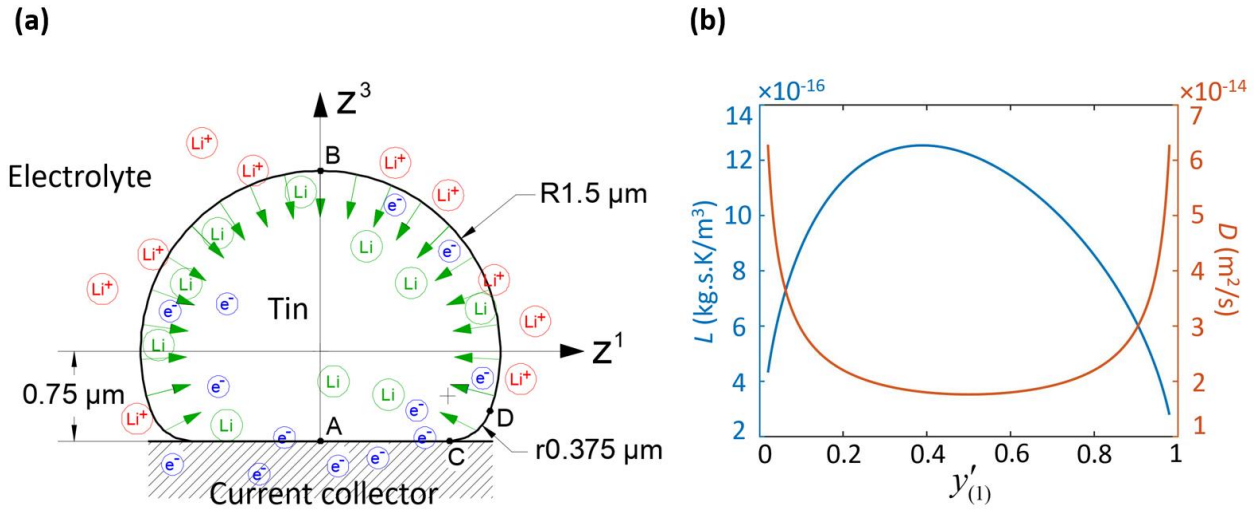


Figure 4.1 (a) A representative Sn anode particle used in the simulation. Initially, the particle is a spherical cap with a fillet. The radius of the spherical cap is $1.5 \mu\text{m}$. The radius of the fillet between points C and D is $0.375 \mu\text{m}$. The distance between the spherical center and the current collector is $0.75 \mu\text{m}$. **(b)** The curves of the thermodynamic coefficient of diffusion L and the diffusivity D serve as functions of the molar fraction of occupied Li^+ sites $y'_{(1)}$.

For simplicity, the numerical simulation of phase separation and the inhomogeneous stress are neglected in this chapter. Hence, we set $\Lambda_{\nabla} = 0$, $\omega_I = 0$, $K_{(12)} = 0$. Other material parameters used for the computation are shown in Table 4.1. $\eta_H^{(e)}$, $\eta_D^{(e)}$ and $\eta_D^{(p)}$ are assigned by referring the viscosity of glass at transition state [126]. Because the stiffness of electrodes may change during charging/discharging [12] [127] [128], the Lamé constants are multiplied by factors $\lambda = k_{\lambda G} \lambda_0$ and $G = k_{\lambda G} G_0$, where λ_0 and G_0 are Lamé constants of pure Sn [78]. The partial molar volume V_{PM} is determined by $V_{PM} = \frac{M_{(2)} R_v}{\rho_0 N_B}$, where R_v is the ratio of the expanded volume of the anode particle after it is fully lithiated by the ideal process that is stress-free and possesses quasi-equilibrium, and ρ_0 is the density of pure Sn. To save on the computation cost, we set $R_v = 1$ which is half of the ratio of a real Sn anode [78].

Table 4.1 Material parameters used in the simulation.

#Estimated value fit to results shown in Figure 4.3. †Estimated value fit to curves shown in Figure 4.1b. ‡Estimated value fit to results shown in Figure 4.7.

Parameter	Unit	Value	Ref.	Parameter	Unit	Value	Ref.
$M_{(1)}$	kg / mol	6.94×10^{-3}	[129]	T	K	300	
$M_{(2)}$	kg / mol	0.119	[129]	L_0	$kg \cdot s \cdot K / m^3$	$1 \times 10^{-15} \dagger$	
N_B	-	4.4	[125]	R_V	-	1	[78]
ρ_0	kg / m^3	7.265×10^3	[129]	N_1	-	$0.5 \dagger$	
λ_0	GPa	40.4384	[78]	N_2	-	$1 \dagger$	
G_0	GPa	19.0299	[78]	N_3	-	$0.5 \dagger$	
α_T	K^{-1}	2.2×10^{-5}	[129]	$k_{\lambda G}$	-	0.7	[127]
$\eta_H^{(e)}$	$GPa \cdot s$	2000	[126]	k_{hRT}	-	$4000 \ddagger$	
$\eta_D^{(e)}$	$GPa \cdot s$	1000	[126]	h_R	nm	1.05	[130]
$\eta_D^{(p)}$	$GPa \cdot s$	1000	[126]	ϕ_0	V	$1 \ddagger$	
$\lambda_0^{(p)}$	$(Pa \cdot s)^{-1}$	$1 \times 10^{-14} \#$		$\Delta\phi_{RIC}$	V	$-0.1 \ddagger$	
$a^{(p)}$	-	-0.5		Δt_I	s	5	
K_ψ	J / Pa^2	$3 \times 10^{-10} \#$		$y'_{(1)0}$	-	5×10^{-4}	
$a^{(R)}$	-	-0.5		J_{M0}	$mol / (m^3 \cdot s)$	5.9011×10^3 \ddagger	

The thermodynamic coefficient of diffusion L in Equation (4.1.62) can be connected to the diffusivity D in Fick's law. With the values of N_1 , N_2 , and N_3 in Table 4.1, Equation (4.1.63) and Equation (4.1.85) yield the curve of L . Comparing Equation (4.1.62) with Fick's 1st law yields the corresponding D of L as shown in Figure 4.1b. The derivation steps are shown in APPENDIX B.6. The shape of D is basically consistent with the results in Ding et al. [131]. The value of D agrees the range between 8×10^{-20} m²/s and 5.9×10^{-11} m²/s mentioned in Shi et al. [132].

4.1.3.3 Boundary conditions, initial conditions and deformation

Due to symmetry, we calculate the right half of the particle. In Figure 4.1a, the segment from point A to point C is designated the bottom, and the segment from point C to point B is called an arc.

The mechanical boundary condition is

$$k_{BAM}^{(i)} p^{ij} n_j + \eta_{BA} (1 - k_{BAM}^{(i)}) v_{(2)j}^L g_{(2)}^{ij} = 0 \quad (4.1.103)$$

with

$$k_{BAM}^{(i)} = \frac{2}{\pi} \arctan \left\{ (l)^{a_{(i)}} \left[1 - (l)^{b_{(i)}} \right]^{-c_{(i)}} \right\}, \quad (4.1.104)$$

where $k_{BAM}^{(i)}$ is the bottom-arc mixing coefficient for the mechanical boundary condition. $k_{BAM}^{(i)}$ helps to prevent singularity by making the mechanical boundary condition change continuously from the bottom to the arc. $k_{BAM}^{(i)}$ is a monotone-increasing function of l with value settings of $a_{(i)}$, $b_{(i)}$ and $c_{(i)}$. l represents the location along the boundary passing through points A, C, D, and B in Figure 4.1a. $l = 0$ at point A and $l = 1$ at point B. For both $i = 1$ and $i = 3$, we set

$k_{BAM}^{(i)} = 0.1$ at point C, $k_{BAM}^{(i)} = 0.9$ at point D, and $k_{BAM}^{(i)} = 0.5$ at the midpoint of the boundary segment between points C point D in Figure 4.1a.

The kinetic boundary condition is composed of the following equations: Equation (4.1.7) for mass conservation, Equations (4.1.67), (4.1.93), (4.1.94), (4.1.95), and (4.1.96) for chemical reaction, and Equation (4.1.38) for the total electric current. The reaction region is very thin compared to the whole particle. The mass conservation equation can be simplified as

$$\rho \mathbf{v} \cdot \mathbf{n} = -J_M M_{(1)} h_R \quad (4.1.105)$$

where h_R is the thickness of the reaction region. In Table 4.1, h_R is assigned by referring the thickness of electrical double layer [133].

Ideally, the chemical affinity on the segment will be zero where the particle contacts the current collector, i.e., only the surface where the particle contacts the electrolyte has the chemical reaction. Like the mechanical boundary condition, to avoid singularity, we set the kinetic boundary condition changes continuously along the surface. A coefficient k_{BAk} with the same mathematical form as Equation (4.1.104) is multiplied on the right side of Equation (4.1.95).

The surface area of the particle changes during (de)lithiation. Based on the particle symmetry with respect to z^2 , the dA of the integral in Equation (4.1.38) changes according to Equation (4.1.106) as shown below:

$$\left(\frac{dA}{dA_0} \right)^2 = \frac{g_{(2)11} - 2g_{(2)13} \left(z^1 / z^3 \right) + g_{(2)33} \left(z^1 / z^3 \right)^2}{1 + \left(z^1 / z^3 \right)^2} \left[\frac{g_{(2)22}}{\left(z^1 \right)^2} \right]. \quad (4.1.106)$$

The derivation steps are shown in APPENDIX B.7. With the kinetic boundary condition, J_M , J_M^+ , J_M^- , A_{CM} , $\mu_{HL(12)}$, and ϕ are added into the equation set for the anode particle in the galvanostatic mode of lithiation.

To make the simulation more stable, we set the total electric current in the collector to change continuously between zero and the maximum. The duration of the change is Δt_f . When the time is zero, the nonzero initial conditions of the system are

$$y'_{(1)} = y'_{(1)0} , \quad (4.1.107)$$

$$\lambda^{(P)+} = \lambda^{(P)-} = \lambda_0^{(P)} , \quad (4.1.108)$$

$$J_M^+ = J_M^- = J_{M0} , \quad (4.1.109)$$

$$\phi = \phi_0 , \quad (4.1.110)$$

$$g_{(2)ij} = \delta_{ij} , \text{ and} \quad (4.1.111)$$

$$\rho_{(2)} = \rho_0 , \quad (4.1.112)$$

where $y'_{(1)0}$ is used for avoiding the negative infinity of the relative chemical potential, the reference chemical reaction rate J_{M0} can be calculated by setting the overpotential $\Delta\phi_{R1C}$ for the 1C electric current under the ideal situation, i.e., $\mu_{(12)} = 0$, ϕ_0 is the reference electrical potential, and δ_{ij} is the Kronecker delta. Initially, the particle is assumed to be stress free, strain free and static, hence the initial values of the following variables are zero: $\boldsymbol{\sigma}$, $\boldsymbol{\varepsilon}^{(e)}$, \mathbf{v} , $\mathbf{v}_{(2)}^L$, and $\mu_{EX(12)}$.

To display the deformation of the particle directly, we need to calculate Z^i , which gives the coordinates of Sn in the lab space. The solved $v_{(2)i}^L$ should be transformed into the component in the lab space with the below equations. The derivation steps are shown in APPENDIX B.8.

The boundary condition for solving Z^i is $v_{(2)L1}^L(z^1 = 0) = 0$.

$$Z^1 = \sqrt{g_{(2)22}} , \quad (4.1.113)$$

$$\frac{\partial Z^3}{\partial z^1} = -\sqrt{g_{(2)11} - \left(\frac{\partial Z^1}{\partial z^1}\right)^2}, \quad (4.1.114)$$

$$\frac{\partial Z^3}{\partial z^3} = \sqrt{g_{(2)33} - \left(\frac{\partial Z^1}{\partial z^3}\right)^2}, \quad (4.1.115)$$

$$v_{(2)i}^L = v_{(2)Lj}^L \frac{\partial Z^j}{\partial z^i}, \text{ and} \quad (4.1.116)$$

$$\frac{\partial Z^i}{\partial t} = v_{(2)Li}^L. \quad (4.1.117)$$

4.2 Results and Discussions

In this chapter, some material parameters of the Li-Sn system currently serve as placeholders for future simulation versatility for different lithium-ion battery binary systems. For example, the reference thermodynamic diffusion coefficient L_0 , viscosities $\eta_H^{(e)}$, $\eta_D^{(e)}$, and $\eta_D^{(p)}$, symmetry factors $a^{(p)}$ and $a^{(R)}$, etc. Compared to the numerical error, the chosen material parameters may dominate the overall error in final results. Hence, analyzing the numerical error in the current simulations lacks practical significance and is neglected in the present theoretical study.

We simulate anode particles at three different C-rates: C-rate=3, C-rate=1.5 and C-rate=0.75. The particles with all three C-rates are lithiated until their states of charge (SOC) are equal to 0.5. Once the SOC reaches 0.5, the particles start to relax, and the electric current decreases to zero within 5 seconds. The initial times of the relaxation ($t_R = 0$) are set when the SOC reaches 0.5. We have presented several key phenomena during the evolution in our simulations, namely molar fraction of occupied sites of Li^+ ($y'_{(1)}$), velocity of Li^+ continuum relative to Sn space ($\mathbf{v}_{(1)}$), mass center velocity relative to lab space ($\mathbf{v}^L = \mathbf{v} + \mathbf{v}_{(2)}^L$), hydrostatic elastic strain ($\varepsilon_H^{(e)} = \varepsilon_m^{(e)}/3$), relative chemical potential ($\mu_{(12)}$), plasticity rate ($\lambda^{(p)}$), hydrostatic elastic stress ($\sigma_H = \sigma_m^m/3$), hydrostatic viscous stress ($\tau_H^{(e)} = \tau_m^{(e)}/3$), hydrostatic Cauchy stress ($p_H = p_m^m/3$), and the evolution of whole cell voltage change as induced by anode $\Delta\phi = \phi_0 - \phi$. Please note that all the components are for the lab space and the values in the results are nondimensionalized if no unit is specified.

During lithiation, $y'_{(1)}$ and $\mu_{(12)}$ increase with a nonuniform distribution as displayed in Figure 4.2. The higher $\mu_{(12)}$ near the arc makes Li^+ move from the arc into the particle. The velocity of Li^+ relative to the Sn space keeps decreasing during lithiation (Figure 4.2) since the fraction of Li^+ is increased. Equation (4.1.4) yields $\mathbf{J}_{(1)} = \rho_{(2)} x_{(1)} \mathbf{v}_{(1)}$, where $x_{(1)}$ increases from zero. Although $\rho_{(2)}$ decreases due to the volume expansion, $\mathbf{v}_{(1)}$ decreases from infinity with the constant lithiation rate. The distribution of \mathbf{v}^L in Figure 4.2 shows that the particle moves relatively faster on the connection region between the bottom and the arc. While the arc moves outward, the \mathbf{v}^L on a portion of the arc points to the interior of the particle. This phenomenon indicates that the deformation of the particle boundary is combined of (1) the movement of the mass center continuum and (2) the generation of the mass center continuum by the chemical reaction on the surface.

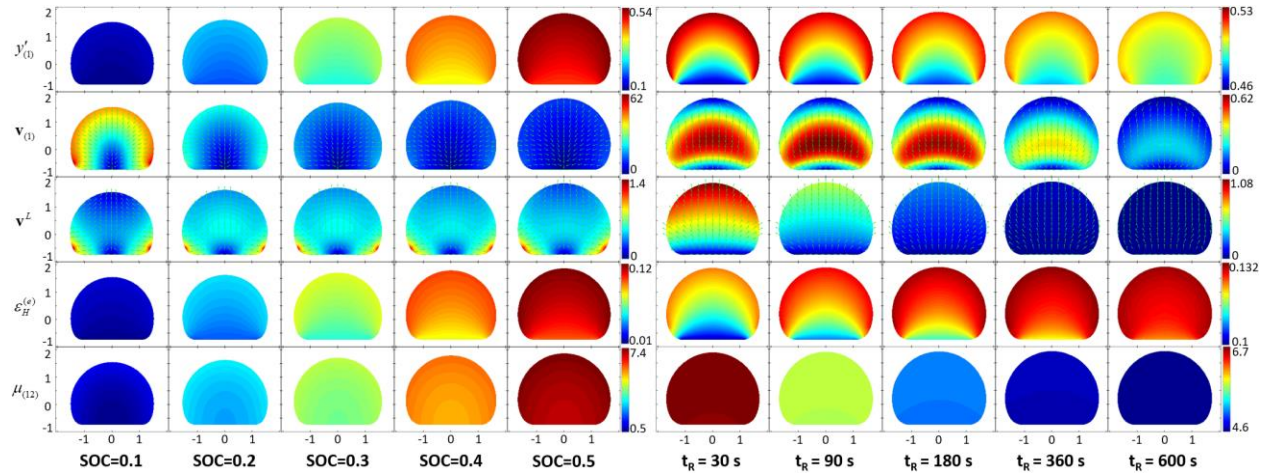


Figure 4.2 A representative evolution of several key parameters in Sn particle: Molar fraction of occupied Li^+ sites $y'_{(1)}$, velocity of Li^+ continuum relative to the Sn space $\mathbf{v}_{(1)}$, mass center velocity relative to lab space \mathbf{v}^L , hydrostatic elastic strain $\epsilon_H^{(e)}$, and relative chemical potential $\mu_{(12)}$ during lithiation (C-rate=3) and relaxation. $y'_{(1)}$ and $\mu_{(12)}$ increase with uneven distributions during lithiation, which indicates the non-equilibrium state of the system. During relaxation, the distributions of all parameters are gradually even, which represents the gradually weakened non-equilibrium state. The particle volume continues to increase during whole process because $\epsilon_H^{(e)}$ increases during both lithiation and relaxation.

In contrast to the increase and the nonuniform distribution of $\mu_{(12)}$ during lithiation, $\mu_{(12)}$ decreases with a tiny gradient during the relaxation, as displayed in Figure 4.2. This observation indicates that the system approaches equilibrium. During relaxation, $\mathbf{v}_{(1)}$ in Figure 4.2 shows that Li^+ keeps diffusing towards the bottom. Hence, $y'_{(1)}$ increases near the bottom and decreases near the arc, as displayed in Figure 4.2. The $\mathbf{v}_{(1)}$ on the arc is mostly tangential during relaxation, which makes $y'_{(1)}$ symmetric along the arc at the end of relaxation. The direction of $\mathbf{v}_{(1)}$ near the top of the particle points outward during relaxation. This result indicates that some Li^+ may move out while the total electric current is zero. The particle volume keeps increasing during relaxation since $\varepsilon_H^{(e)}$ is increased.

With the increase of particle volume, $\lambda^{(p)}$ concentrates around the bottom as displayed in Figure 4.3a. This trend indicates that the failure of the particle may initiate near the bottom because of the stronger plastic deformation occurring there. The particle lithiated at a higher C-rate shows a higher plasticity rate, suggesting a higher probability of failure. Figure 4.3b shows that the maximum $\lambda^{(p)}$ in the particles of all three C-rates reach stable values during lithiation and decrease during relaxation, which means that the corresponding generalized driving force ψ are constrained to stable values by plastic deformation. This phenomenon is consistent with the yield stress in the ideal plasticity model.

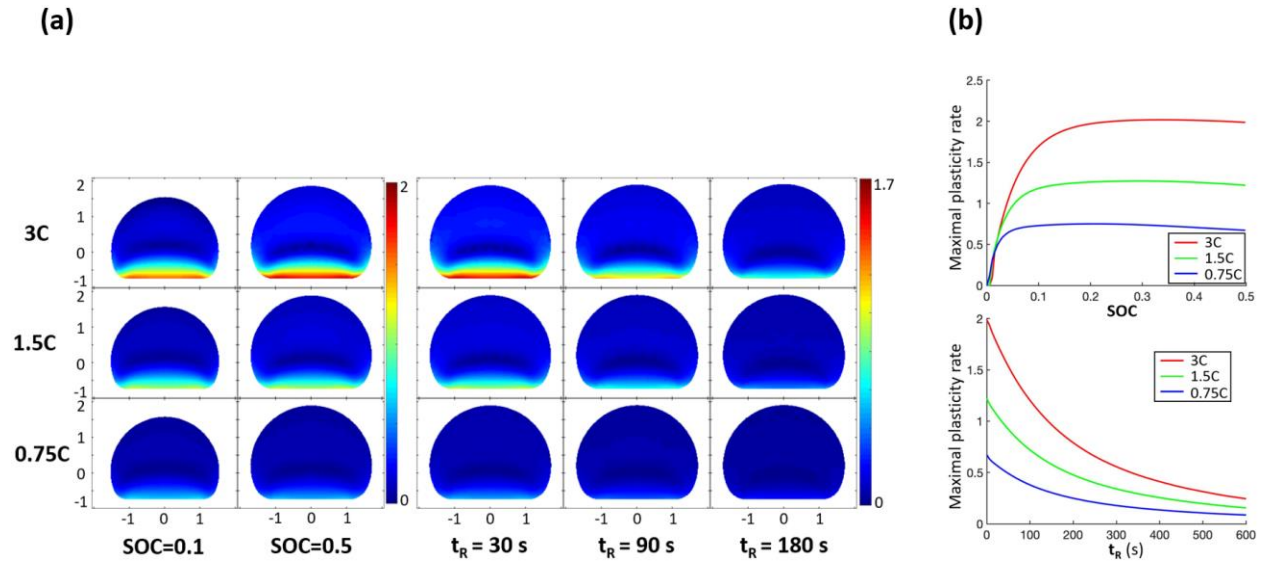


Figure 4.3 (a) Plasticity rate $\lambda^{(p)}$ at SOC 0.1 and 0.5, followed by the relaxation until $t_R = 180$ s.

The maximum plasticity rate locates near the bottom region of the particle. **(b)** Maximum plasticity rate in the particle during lithiation and relaxation with three different C-rates. During lithiation, the maximum $\lambda^{(p)}$ of every particle initially increases and till reaching to a constant value. A higher C-rate indicates a higher maximum $\lambda^{(p)}$.

The spontaneous increase of particle volume indicates the lower free energy at a larger volume. Then Equation (4.1.30) yields $\sigma_H < 0$, which is demonstrated by Figure 4.4 for all three C-rates. During the lithiation, the σ_H with a higher C-rate is more negative than that with a lower C-rate, which implies a faster decrease of free energy and a faster volume expansion. With increased SOC and C-rates, σ_H displays stronger nonuniform distribution. The most negative σ_H concentrates near the bottom of the particle. During relaxation, the distributions of σ_H in Figure 4.4 appears more uniform with increases in t_R . σ_H approaches zero at the end of relaxation, which indicates the slowdown of free energy change.

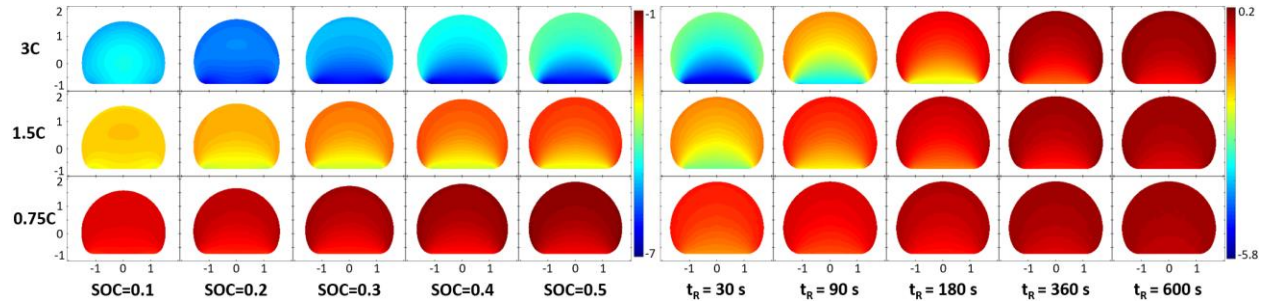


Figure 4.4 Hydrostatic elastic stress σ_H during lithiation (SOC = 0.1 – 0.5) and relaxation (t_R = 30-600 seconds) at three different C-rates (3C, 1.5C, and 0.75C). σ_H becomes negative during lithiation at all C-rates. $\sigma_H < 0$ means that free energy is decreased when particle volume is increased. Volume expansion is hence a spontaneous behavior of the particle. A higher C-rate corresponds, σ_H becomes more negative, which implies a faster decrease of free energy and a faster volume expansion of the particle. During relaxation, σ_H with all C-rates get close to zero with gradually even distributions, which indicate the slowdown of free energy change.

Figure 4.5 shows the evolution of $\tau_H^{(e)}$ during lithiation and relaxation. A higher C-rate leads to a higher strain rate, and hence a higher $\tau_H^{(e)}$. With an increased SOC, $\tau_H^{(e)}$ slightly decreases. This decrease may occur because the enlarged particle volume decreases the volume expansion rate. During relaxation, $\tau_H^{(e)}$ decreases because the strain rate decreases when the system approaches equilibrium.

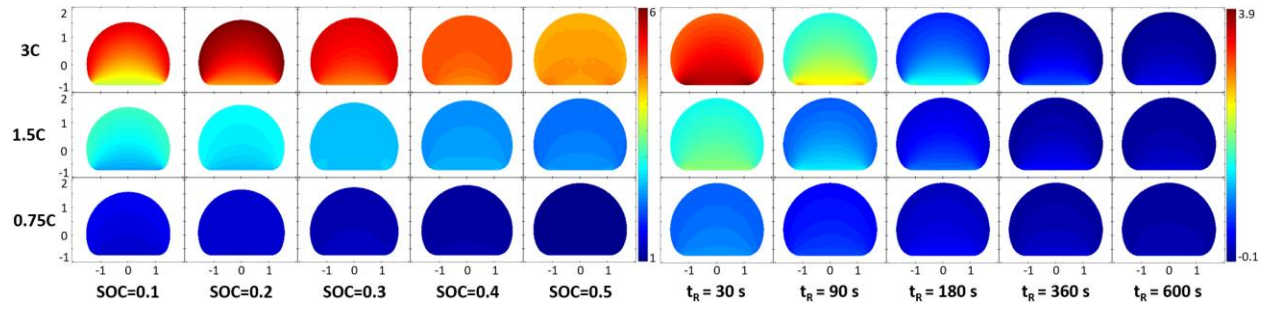


Figure 4.5 Hydrostatic viscous stress $\tau_H^{(e)}$ during lithiation (SOC = 0.1 – 0.5) and relaxation ($t_R = 30$ -600 seconds) at three different C-rates (3C, 1.5C, and 0.75C). A higher C-rate indicates a higher $\tau_H^{(e)}$ which slightly decreases with increased SOC. During relaxation, $\tau_H^{(e)}$ with all C-rates are close to zero with gradually even distributions, which indicate that particles approach to the equilibrium state.

The evolution of p_H is shown in Figure 4.6. The particle is mostly in compression. p_H presents a more negative value when the C-rate is higher. The region around the bottom has stronger compression than the bulk of the particle, due to bonding with the current collector. The p_H with a higher C-rate shows more noticeable nonuniform distribution. During relaxation, the nonuniform distribution gradually disappears and p_H approaches zero, which suggests a gradually weakened non-equilibrium state.

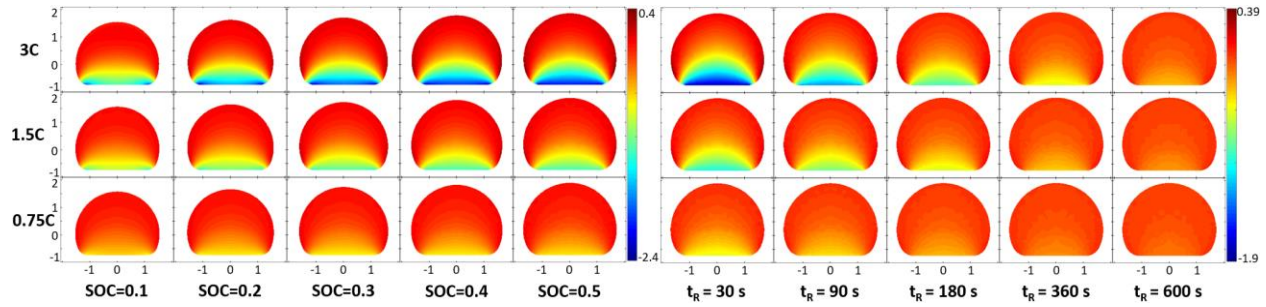


Figure 4.6 Hydrostatic Cauchy stress p_H during lithiation (SOC = 0.1 – 0.5) and relaxation (t_R = 30-600 seconds) at three different C-rates (3C, 1.5C, and 0.75C). The negative value of p_H indicates that the particle is mostly in compression. The bottom region shows stronger compression than the bulk region due to the bonding between the particle and current collector. A higher C-rate and a higher SOC indicate a stronger uneven-distribution of p_H . The uneven distribution gradually disappears during relaxation, which indicates the particles approach to the equilibrium state.

Figure 4.7 displays the voltage change for an entire cell as induced by the anode particle. Three anode particles are lithiated with 3C, 1.5C, and 0.75C. The time equals zero at the beginning of lithiation. Anode particles with 3 different C-rates reach 0.5 SOC when $t=600s$, $1200s$, and $2400s$, respectively. During the lithiation, the $\Delta\phi$ with the higher C-rate increases faster than the $\Delta\phi$ with a lower C-rate since more electrical energy is dissipated. All the particles relax to $t=3000s$ once their SOC reaches 0.5. During relaxation, for all three C-rates, $\Delta\phi$ at first decreases steeply, then approaches stable values after gentle decreases. The steep decreases correspond to the relaxation of the chemical reaction. The gentle decreases correspond to diffusional relaxation. The particle with the higher C-rate needs longer time to relax in the polarizations induced by both chemical reaction and diffusion, due to the stronger non-equilibrium effects of the higher C-rate. The particle with the lower C-rate has a relatively higher final $\Delta\phi$. This finding suggests that the battery charged by the lower C-rate may supply more electrical energy, even though it has the same charge capacity.

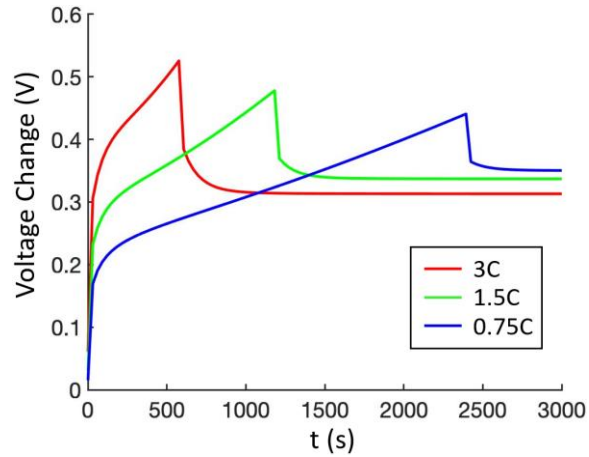


Figure 4.7 The evolution of whole cell voltage change $\Delta\phi$ induced by the anode during charging/relaxation at three different C-rates. A higher C-rate indicates a higher $\Delta\phi$ during lithiation. The relaxation stage of $\Delta\phi$ for every C-rate includes a steep decrease followed by a gentle decrease. A higher C-rate corresponds to a lower final voltage change $\Delta\phi$. Thus, the cell charged by a lower C-rate results in a higher voltage at the end of relaxation.

Although the bonding between the particle and the current collector restricts the deformation of the bottom region, the plasticity flow releases the elastic deformation of the particle. The maximum $\lambda^{(p)}$ locates around the bottom, as displayed in Figure 4.3a. For 3C lithiation, Figure 4.3b shows that the $\lambda^{(p)}$ around the bottom has not reached the stable value yet when SOC=0.1. This observation suggests that the plasticity deformation may not be enough to release the elastic deformation when SOC=0.1. It is consistent with the distribution of $\tau_H^{(e)}$ in Figure 4.5, by using Equation (4.1.60). The particle with 3C lithiation has a noticeable nonuniform distribution of $\tau_H^{(e)}$ when SOC=0.1. This occurs because the elastic strain rate around the bottom is restricted by bonding, while the $\lambda^{(p)}$ is not yet sufficient to release the volume expansion there. With the increased SOC during lithiation, $\lambda^{(p)}$ reaches the stable value as displayed in Figure 4.3b, and the elastic strain rate is sufficiently released around the bottom. Hence, the distribution of $\tau_H^{(e)}$ in Figure 4.5 appears more uniform during lithiation. During relaxation, the plasticity flow continues to release the elastic deformation and results in $\varepsilon_H^{(e)}$ and σ_H more uniformly distributed, as shown in Figure 4.2 and Figure 4.4. σ_H is related to $\varepsilon_H^{(e)}$ and $y'_{(1)}$. During relaxation, the uniformization of $\varepsilon_H^{(e)}$ and σ_H suggests the decrease of the gradient of $y'_{(1)}$, as shown in Figure 4.2. When approaching to the equilibrium, $\lambda^{(p)}$ gets close to zero (Figure 4.3b) since the driving force of $\lambda^{(p)}$ nearly vanishes, and σ_H is nearly zero and is uniformly distributed (Figure 4.4).

The driving force of the plasticity flow depends on the elastic stress, as depicted in Equation (4.1.52). To ensure $\lambda^{(p)}$ being higher around the bottom of the particle in lithiation/relaxation as displayed in Figure 4.3a, ψ should be higher around the bottom.

Maintaining this nonuniform distribution of ψ leads to the nonuniform distribution of σ_H between the bulk and the bottom, as shown in Figure 4.4. σ_H and $\tau_H^{(e)}$ satisfy the equation $\sigma_H + \tau_H^{(e)} = p_H$ which is derived from Equation (4.1.48). Since $\tau_H^{(e)}$ shows relatively uniform distribution in Figure 4.5, the distribution of p_H in Figure 4.6 looks similar to the distribution of σ_H in Figure 4.4. Thus, the nonuniformly distributed p_H should be a necessary condition of the mechanical non-equilibrium process. During the lithiation, the distribution of both σ_H and p_H approach steady states as shown in Figure 4.4 and Figure 4.6 respectively. The steady states indicate the mechanical minimum entropy production in the particle, based on the principle of minimum entropy production in non-equilibrium thermodynamics [96]. Minimizing the mechanical entropy production of the particle should be the essential reason why $\tau_H^{(e)}$ approaches a uniform distribution during lithiation in Figure 4.5.

Compared with the higher C-rate, a lower C-rate leads to a slower volume expansion. The elastic strain rate with the lower C-rate is hence lower. This relation indicates that the necessary $\lambda^{(p)}$ for releasing the elastic deformation around the bottom is lower. This trend is consistent with the results in Figure 4.3b. The particle requires a shorter process to reach the lower stable value of $\lambda^{(p)}$. This is the reason why the $\tau_H^{(e)}$ with the lower C-rate approaches the uniform distribution earlier than that with the higher C-rate, as displayed in Figure 4.5. The lower $\lambda^{(p)}$ corresponds to the lower driving force ψ , which leads to a less nonuniform distribution of σ_H , as shown in Figure 4.4. Hence, Figure 4.6 shows that the p_H with the lower C-rate has a less nonuniform distribution.

The different C-rate corresponds to the different chemical reaction rate J_M , which depends on the $\Delta\phi$ and $\mu_{(12)}$ on the arc of the particle. For the 3C lithiation, Figure 4.2 shows that $\mu_{(12)}$ keeps increasing on the arc. With the chemical reaction model in Section 4.1.2.2, Figure 4.7 shows a consistent result that $\Delta\phi$ increases with the increased SOC during lithiation. During relaxation, the Li^+ on the arc continues to diffuse into the interior of the particle, and the $\mu_{(12)}$ on the arc decreases due to the diffusion of Li^+ , as displayed in Figure 4.2. Based on the model of the chemical reaction, $\Delta\phi$ hence decreases with the $\mu_{(12)}$ during diffusional relaxation, as indicated in Figure 4.7. This process is attributed to approaching an equilibrium state of the solution system. Figure 4.7 suggests that particles for 3C, 1.5C and 0.75C are close to their equilibrium state at $t=1200\text{s}/t_R=600\text{s}$, $t=1550\text{s}/t_R=350\text{s}$ and $t=2600\text{s}/t_R=200\text{s}$, respectively, where t_R is the relaxation time. We thus expect that other state functions, i.e., σ_H , $\tau_H^{(e)}$, and p_H , show similar distributions with respect to different C-rates near these time points. Figure 4.4 shows that the distributions of σ_H on $t_R=600\text{s}/3\text{C}$ are similar to the distribution of σ_H on $t_R=360\text{s}/1.5\text{C}$ and $t_R=180\text{s}/0.75\text{C}$. Figure 4.5 and Figure 4.6 also show the same phenomenon for $\tau_H^{(e)}$ and p_H at the same time points. This consistency implies a coupling between the mechanics and electrochemistry of electrodes.

Some modeling studies [82] [93] [134] for the mechanical-diffusional coupling effects of electrodes specialized their formulations for the spherical particle with traction-free boundary condition, of which simulations were simplified to 1D. The equations in this study, by contrast, are suitable for generalized geometry. Leo et al. [27] contributed the 2D finite element simulation for a spheroid electrode particle based on the finite deformation framework, but the plastic deformation was not included. Compared to the 1D simulations for traction-free spherical

particles, the 2D simulation for the spherical cap particle bonded on current collector in this study illuminates the effect of plastic flow in a more realistic scenario: plastic flow can release the stress concentrated by the boundary constraint, as discussed above, and weaken the nonuniform distribution of Li^+ in the particle, and finally help increase the effective capacity of the electrode. This effect agrees with the finite element simulation of a hollow double-walled Si nanotube anode by Leo et al. [81]: Li-ion concentration is uniformly distributed in the whole nanotube, and the plastic deformation induced by the tangential constraint concentrates at the interior surface of the nanotube (cf. Figure 6 in Leo et al. [81]). The effective capacity of the nanotube with plasticity is much higher than that without plasticity (cf. Figure 9 in Leo et al. [81]).

Because of the geometry differences, the Li-ion concentration in this study is noticeably nonuniform distributed than that in Leo et al. [81]. At the end of relaxation, the particle approaches its equilibrium state: $y'_{(1)}$ in Figure 4.2 shows (1) a relatively higher value that evenly distributes along the arc section of the particle boundary, and (2) the sharp change at the connection between the arc and the bottom of the particle boundary (point C in Figure 4.1a). These two phenomena were also displayed in the cross-section image of a Sn particle captured by the field emission scanning electron microscope (FESEM) in the study of Takeuchi et al. [125], in which the Sn particle was bonded on current collector and slowly lithiated (C-rate = 0.0146) by Li focused ion beams (Li-FIB). In addition, the FESEM image for the cross-section of the Sn particle (cf. Figure 1d in Takeuchi et al. [125]) shows a band of contrast in the bulk region near the implantation area of Li-FIB, which is not revealed in our simulation (Figure 4.2). This difference may be attributed to the different boundary conditions of Li^+ flux on particle surface: The localized Li-FIB had been shown to generate complicated local plastic deformation

on the implantation area (cf. Figure 1c in Takeuchi et al. [125]), which leads to the local unforeseen distribution of Li^+ concentration due to the mechanical-diffusional coupling effect.

The mechanical-diffusional-electromechanical coupling effect in this study is formulated based on the continuity of state functions, as shown in Section 4.1.1, which yields the spatial continuity of θ and $\nabla\theta$ during the non-equilibrium process. Hence $\lambda^{(p)}$ and $\nabla\lambda^{(p)}$ should be continuous over space. This requirement is satisfied by the kinetic plasticity model $\lambda^{(p)} = \lambda^{(p)}(\psi)$ in Section 4.1.2.2, which is a continuous function without involving a specific yielding strength. When ψ is relatively tiny, $\lambda^{(p)}$ represents the stress-induced creep. The kinetic plasticity model shows the similar response of plastic strain to the ideal plasticity model [135] when K_ψ in Equations (4.1.55) and (4.1.56) is large enough. The smooth transition between the elastic region and plastic region of electrodes has been formulated using the piecewise power functions in Bower et al. [26] [82], Cui et al. [134] [93], and Leo et al. [81]. Compared to the piecewise plasticity models, the kinetic plasticity model helps simplify the procedure of solving the system equations by excluding the radial return algorithm [136] [137] used for locating the plastic region in the system.

The chemical potential model that includes the finite deformation of electrodes has been studied by Cui et al. [134] [93], in which the mechanical part of the chemical potential model has a coefficient term $\left(\frac{\partial \mathbf{F}^*}{\partial c}\right)_{\mathbf{F}, \mathbf{C}}$ that represents the deformation change induced by the concentration change for the intermediate state under the fixed total deformation and the fixed stiffness.

However, $\left(\frac{\partial \mathbf{F}^*}{\partial c}\right)_{\mathbf{F}, \mathbf{C}}$ relates to not only the material property (i.e., the expansion ratio) but also the change of elastic state, which is implicit and needs to be solved. In contrast, the relative

chemical potential model in this study uses the material property K_D only to explicitly show the mechanical part. In some other studies of modeling the finite deformation of electrodes, e.g., Bower et al. [26], Dal and Miehe [83], Leo et al. [27] [81], and Bucci et al. [84], the chemical potential are modeled based on the Larche-Cahn model [29] shown in Equation (1.1.1). However, the Larche-Cahn model [29] is based on the assumptions that (1) the deformation of the system is small and thermodynamically reversible and (2) the molar mass of Li-ion is much less than the molar mass of site component, $M_{(1)} \ll M_{(2)}$. The assumption of small deformation would result in the metric change negligible. Thermodynamic reversibility would result in the integral to be path independent. $M_{(1)} \ll M_{(2)}$ indicates constant density and $\mathbf{v} = \mathbf{0}$, which linearize the rate Equations (4.1.46), (4.1.79), and (4.1.80). Then directly integrating the rate equations yields the Larche-Cahn model, which is a special case of the non-equilibrium model in this study. Using the Larche-Cahn model suggests the acceptance of above two assumptions. However, the assumption (1) is limited in the infinitesimal deformation and an equilibrium process. The assumption (2) oversimplifies the diffusion of Li^+ since the molar mass of Li^+ should not be negligible for most electrode materials. Therefore, it is not plausible to adopt the Larche-Cahn model to describe the chemical potential of electrodes with finite deformation or non-equilibrium process.

As Li^+ should share the stress of electrodes, we consider the movement of lithium as a part of the deformation of the mixture system represented by the mass center continuum. The deformation of the mixture system should be formulated based on the mass-conserved infinitesimal element instead of the mole-number-conserved infinitesimal element, because the different molar mass of components make the mass conservation conflicted with the mole-number-conservation in the infinitesimal element of mass center continuum. Thus, we use the

mass fractions of components instead of the concentration of components, and the specific free energy instead of the free energy density to formulate the mixture system. In the existing studies for modeling the finite deformation of electrodes [26] [27] [81] [83] [84] [93] [134], by contrast, the concentration of components and the free energy density are used in the formulations based on the mole-number-conservation, suggesting that the movement of Li^+ are not considered as a part of the deformation of the mixture.

The mass-conserved infinitesimal element of the mixture system is introduced by using multi metric spaces, in which every space reveals the deformation of every corresponding component in the mixture. The method of multi metric spaces helps distribute the strains of the mixture system conveniently: the Li-Sn system includes three metric spaces (i.e., mass center space, Sn space, and lab space), in which the Sn space is selected as the reference space because (1) the elastic strain and the plastic strain rate of the mixture are assigned to the Sn continuum due to the interstitial mixing of the Li-Sn system, and (2) the Sn space is the Lagrangian space of the Sn continuum, which satisfies the requirement of the additive decomposition of strain component (Equation (4.1.11)) derived from the metric-based definition of the finite strain (Equation (4.1.10)). Compared to the multiplicative decomposition of deformation gradient used in the other modeling works for finite deformation of electrodes [26] [27] [81] [84] [93] [134], the additive decomposition of strain component is linear, simpler and also valid for the finite deformation of electrodes.

The method of multi metric spaces in this study reveals the diffusion-induced creep of electrodes. In the Li-Sn system described in the Sn space (i.e., reference space), the influences of diffusion-induced creep on the mixture (i.e., mass center continuum) are represented by the diffusion-induced convective effects, which are indicated by the terms including \mathbf{v} (i.e., the

mass center velocity relative to the reference space) in rate Equations (4.1.46), (4.1.79) and (4.1.80). In the relation between the electrical potential and Li^+ concentration of a Si film electrode measured by Pharr et al. [89], the electrical potential showed transient trend reversal with each change of C-rate during lithiation, and the rate of the trend reversal is higher when the change of C-rate is larger (cf. Figure 1 in Pharr et al. [89]). This phenomenon may be explained by the influence of diffusion-induced creep: At the moment of instantly increasing the C-rate of the Si film electrode during lithiation, in the region of chemical reaction, $\varepsilon_{kj}^{(e)} \frac{\partial v^k}{\partial z^i}$ and $v^k \frac{\partial \varepsilon_{ij}^{(e)}}{\partial z^k}$ in Equation (4.1.46) increase instantly, while the change of $\frac{\partial \varepsilon_{ij}^{(e)}}{\partial t}$ may keep negligible because of the viscosity of the electrode. Then increased $\dot{\varepsilon}_{ij}^{(e)}$ may decrease $d\mu_{(12)}/dt$ by Equations (4.1.80) and (4.1.81) since $K_D < 0$. Finally, the slope $\partial\phi/\partial t$ is increased by Equation (4.1.66). ϕ hence transiently increases after each instant decrease induced by increasing the C-rate, and vice versa. When the change of C-rate is larger, the changes of terms $\varepsilon_{kj}^{(e)} \frac{\partial v^k}{\partial z^i}$ and $v^k \frac{\partial \varepsilon_{ij}^{(e)}}{\partial z^k}$ in Equation (4.1.46) are larger, finally the trend reversal of ϕ is faster. As ϕ is influenced by \mathbf{v} in Equation (4.1.46), the diffusion-induced creep should take part in the mechanical-diffusional-electrochemical coupling effect of electrodes.

As the influence of the diffusion-induced creep, the terms including \mathbf{v} in rate Equations (4.1.46), (4.1.79) and (4.1.80) make the integrals for elastic strain, elastic stress, and relative chemical potential related to the history of diffusion. Furthermore, the elastic stress is influenced by the rate of deformation, because of the viscous stress $\boldsymbol{\tau}^{(e)}$ in Equations (4.1.48) and (4.1.57). Therefore, the states of a mixture system relate to the history and the rate of the evolution of the

system, which is an essential feature of the non-equilibrium process. Compared to the framework that is based on the rate functions for modeling the non-equilibrium process of electrodes in this study, the formulations in existing contributions [26] [27] [81] [84] [93] [134] are based on the assumed explicit expressions of the free energy density without considering the viscosity and diffusion-induced creep, which are only suitable for the systems in quasi-equilibrium process.

4.3 Conclusion

In this chapter, we have developed a general theory to describe the evolution of a solid solution system with finite deformation. The system is considered as a non-equilibrium process rather than a quasi-equilibrium process. This fully self-consistent theory is hence formulated based on rate functions. Mechanics, diffusion, phase separation, chemical reaction and electrical potential of the system are coupled with each other in the formulation. The key function of the coupling is the rate of the relative chemical potential that depends on the elastic strain rate and Li-ion fraction rate. The general theory has been applied to a simplified Li-Sn system in Li-ion batteries. We set multiple metric spaces to clarify the influence of the diffusion-induced creep of the system and to help assign different strains conveniently. During the non-equilibrium process of the Li-Sn system, the entropy production rate of the system is composed of a mechanical component, a diffusional component, and a chemical reaction component. The mechanical part is comprised of viscosity and plasticity and where the linearized viscosity is used. The plasticity and chemical reaction are formulated based on the transition-state theory. The kinetic formulation of the plasticity generates a continuous interface between elastic deformation and plastic deformation which helps obviate the steps of identifying the plastic region in the system and simplify the procedure of solving the plasticity of electrodes.

Three Sn electrode particles with initial spherical cap geometries and appropriate boundary conditions have been numerically simulated using the finite difference method coded with MATLAB. We have compared the lithiated processes of the particles with three different C-rates, including the lithiation and relaxation. The simulation results show that the bottom region of each particle has more plastic deformation than the bulk region. The plastic deformation helps release the volume expansion around the bottom region, although it is bonded. The particle with

a higher C-rate needs a longer process to obtain a higher rate of plastic deformation, which releases the faster volume expansion around the bottom. During lithiation, the electrical potential of the particle with a higher C-rate shows more polarization. After relaxation, the particle with a lower C-rate consists of more electric energy, even though the final electric capacities of all particles are the same.

With rigorous mathematical formulation, we illuminate the evolution of a solid solution system in detail. Our developed theory and simulation help better understand the mechanical-diffusional-electrochemical coupling effect in Li-ion batteries. Some innovations in this study, such as multiple metric spaces for different components, diffusion-induced creep/convection, viscosity, and kinetic plasticity, may provide more insight into the description of continuous mixtures especially at non-equilibrium.

CHAPTER 5

Summary

In this research, we have studied the mechanical-electrochemical coupling effect and its related kinetic behaviors for electrodes of different materials.

Based on linear stress-chemical potential model and anisotropic dislocation mechanics, the influences of the density and orientation of dislocations are investigated for a single LFP particle. The modified Butler-Volmer equation is applied as the boundary condition of a Li^+ diffusion system that is governed by Fick's law. The anisotropic stiffness of LFP depends on the phase fraction of the system. The partial molar volume of LFP is modeled to depend on the fraction of Li^+ .

The stress field and displacement field for the LFP particle are simulated for 4 groups of dislocations, in which a dislocation changes its orientation in every group. CV curves are simulated for all configurations of dislocations under different scan rates using the finite difference method coded in MATLAB. The peak values of CV curves are substituted into the Randles-Sevcik equation to obtain the effective diffusivity compared for all dislocation configurations. The results show that tailored dislocation configurations can improve the effective diffusivity of Li^+ , especially for stronger non-equilibrium states. Dislocations show their ability to alleviate the capacity loss of LFP, especially for higher densities with optimized orientations.

A potential strategy has been demonstrated that adopting engineered dislocations with optimized configurations can improve the electrode performance for Li-ion batteries, based on the mechanical-electrochemical coupling effect. We provide insights to develop the dislocation-involved mechanics and electrochemistry for battery systems.

Furthermore, dislocation-involved mechanical-electrochemical coupling effect has been applied to find a mechanism to explain the variations of phase transition behaviors for LFP and layered oxides under non-equilibrium process. The formulation of the mechanism constructs the free energy with path factors which are the functions of a series of order parameters describing the multi-layered states of electrodes. The dislocation density has been homogenized to be a continuous field and coupled with electrochemical reaction on particle surfaces. Increased (de)lithiation current can increase the dislocation inside the particle and then increase the free energy of electrode. Order parameters will be spontaneously changed to lower the free energy, during which the path factors change. The mechanism can be simply described in one sentence: the path for the change of free energy alters to lower the free energy. The order parameters can reveal the states of Li-rich/Li-poor, delithiation/lithiation, equilibrium /non-equilibrium, and order/disorder structure of the material. Governing equations derived from the layered free energy are solved in Mathematica and Matlab using the finite difference method. The simulation includes the galvanostatic cycling and relaxation under different C-rates for multi-particle LFP and NMC111, and the potentiostatic delithiation for the order-disorder structure change of LFP. All simulated results well agree with the existing experimental observations, which validate the path altering mechanism for the electrodes of Li-ion batteries. The formulation suggests that adjusting the dislocation density on particle surfaces or adjusting the coupling coefficients between dislocation reaction and electrochemical reaction can change the states of electrode particles, which supplies potential strategies to improve the performance of electrodes.

To expand the description of the mechanical-electrochemical coupling effect to large deformation, a generalized formulation with finite deformation is developed for non-equilibrium process. The rate functions of system's states are applied in the formulation. To develop a self-

consistent architecture, continuum mechanics and non-equilibrium thermodynamics are combined. An elucidated general theory has been applied to a simplified Li-Sn system. The mathematical formulation for finite deformation is based on the metric tensor. Multiple metric spaces are utilized for assigning different strains. Solid viscosity, diffusion-induced creep/convection are included in the dissipation process. The plasticity and the chemical reaction of a Sn particle are modeled based on the transition-state theory. The Sn particle has a spherical cap initial geometry and is simulated in MATLAB using the finite difference method. The evolutions of state functions are compared for different C-rates.

The rigorous mathematical formulation illuminates the mechanism of the mechanical-electrochemical coupling effect for large deformation and non-equilibrium process, which provides more insight into the description of continuous mixtures system at non-equilibrium process.

This research constructs new theories and approaches to formulate the (de)lithiation process of Li-ion batteries, which have explained existing phenomena observed in experiments and predicted undiscovered features that can be applied to enhance the performance of Li-ion batteries. In addition, our theoretical work supplies new insight into understanding the non-equilibrium process for energy storage systems. Based on the theories, our numerical simulations have revealed the data that cannot be directly measured in experiments. For example, the evolutions of order parameters, stress in electrode particles, the velocity of Li^+ migration, plastic and creep deformation, etc. The revealed information can be applied to enhance the performance of Li-ion batteries. The error in the numerical simulation results includes the errors due to following three factors, (1) the limitation of main parameters' number, (2) measured material properties, and (3) the algorithms for numerical solving. Typically, the error from the limitation

of main parameters' number is larger than that from the solving algorithm, if the system keeps convergent. Because of the complexity of electrochemical systems, the experimental results lack strong consistency in detail among different measurements. The lack of consistency may be caused by the change of the distribution of particle sizes, particle shapes, crystalline, ratio between active/inactive components, etc., which are inevitable in experiments. The weak consistency due to the change of material states (1) decreases the significance of pursuing tiny errors in numerical simulations, and (2) increases the tolerance for the error from measured material properties. We have adopted the implicit algorithm for the finite difference method, which avoids the potential divergence of the kinetic system. By adjusting the time-step and space-step for the finite difference to be tiny enough, we can neglect the error from numerical algorithms. The number of main parameters must be compromised to the complexity and cost of computing. The reliability of our theories has been sufficiently validated since the main features and data observed in experiments well match our simulation results.

REFERENCES

- [1] J.-M. Tarascon and M. Armand, "Issues and challenges facing rechargeable lithium batteries," *Nature*, vol. 414, pp. 359–367, 2001, [Online]. Available: www.nature.com
- [2] J. T. Warner, *Lithium-Ion Battery Chemistries, A Primer*. Elsevier, 2019.
- [3] R. A. Huggins, *Advanced batteries: Materials science aspects*. Springer US, 2009. doi: 10.1007/978-0-387-76424-5.
- [4] A. Nyman, T. G. Zavalis, R. Elger, M. Behm, and G. Lindbergh, "Analysis of the Polarization in a Li-Ion Battery Cell by Numerical Simulations," *J Electrochem Soc*, vol. 157, no. 11, p. A1236, 2010, doi: 10.1149/1.3486161.
- [5] C. M. Julien, A. Mauger, K. Zaghib, and H. Groult, "Comparative Issues of Cathode Materials for Li-Ion Batteries," *Inorganics (Basel)*, vol. 2, pp. 132–154, 2014, doi: 10.3390/inorganics2020132.
- [6] R. A. Huggins, "Negative Electrodes in Lithium Cells," *Advanced Batteries*, pp. 123–149, 2008, doi: 10.1007/978-0-387-76424-5_7.
- [7] M. Alkhedher, A. B. Al Tahhan, J. Yousaf, M. Ghazal, R. Shahbazian-Yassar, and M. Ramadan, "Electrochemical and thermal modeling of lithium-ion batteries: A review of coupled approaches for improved thermal performance and safety lithium-ion batteries," *Journal of Energy Storage*, vol. 86. Elsevier Ltd, May 01, 2024. doi: 10.1016/j.est.2024.111172.
- [8] A. Jaiswal *et al.*, "Nanoscale LiFePO₄ and Li₄Ti₅O₁₂ for High Rate Li-Ion Batteries," *J Electrochem Soc*, vol. 156, no. 12, p. A1041, 2009, doi: 10.1149/1.3223987.
- [9] H. Chen and H. Y. S. Huang, "Modeling and simulation of the non-equilibrium process for a continuous solid solution system in lithium-ion batteries," *Int J Solids Struct*, vol. 212, pp. 124–142, 2021, doi: 10.1016/j.ijsolstr.2020.11.014.
- [10] H. Chen, S. Kim, and H. Y. S. Huang, "Exploration of the dislocation-electrochemistry relation in LiFePO₄ cathode materials," *Acta Mater*, vol. 237, Sep. 2022, doi: 10.1016/j.actamat.2022.118158.
- [11] D. Goonetilleke *et al.*, "Structural Evolution and High-Voltage Structural Stability of Li(Ni_xMn_yCo_z)O₂ Electrodes," *Chemistry of Materials*, vol. 31, no. 2, pp. 376–386, Jan. 2019, doi: 10.1021/acs.chemmater.8b03525.
- [12] T. Maxisch and G. Ceder, "Elastic properties of olivine Li_xFePO₄ from first principles," *Phys Rev B Condens Matter Mater Phys*, vol. 73, no. 17, pp. 1–4, 2006, doi: 10.1103/PhysRevB.73.174112.
- [13] Y. C. Song, Z. Z. Li, A. K. Soh, and J. Q. Zhang, "Diffusion of lithium ions and diffusion-induced stresses in a phase separating electrode under galvanostatic and potentiostatic operations: Phase field simulations," *Mechanics of Materials*, vol. 91, pp. 363–371, 2015, doi: 10.1016/j.mechmat.2015.04.015.
- [14] J. Vetter *et al.*, "Ageing mechanisms in lithium-ion batteries," *J Power Sources*, vol. 147, no. 1–2, pp. 269–281, 2005, doi: 10.1016/j.jpowsour.2005.01.006.
- [15] D. Wang, X. Wu, Z. Wang, and L. Chen, "Cracking causing cyclic instability of LiFePO₄ cathode material," *J Power Sources*, vol. 140, no. 1, pp. 125–128, 2005, doi: 10.1016/j.jpowsour.2004.06.059.
- [16] D. M. Piper, T. A. Yersak, and S.-H. Lee, "Effect of Compressive Stress on Electrochemical Performance of Silicon Anodes," *J Electrochem Soc*, vol. 160, no. 1, pp. A77–A81, 2013, doi: 10.1149/2.064301jes.

- [17] F. Shi, Z. Song, P. N. Ross, G. A. Somorjai, R. O. Ritchie, and K. Komvopoulos, "Failure mechanisms of single-crystal silicon electrodes in lithium-ion batteries," *Nat Commun*, vol. 7, no. May, pp. 1–8, 2016, doi: 10.1038/ncomms11886.
- [18] Y. T. Cheng and M. W. Verbrugge, "Evolution of stress within a spherical insertion electrode particle under potentiostatic and galvanostatic operation," *J Power Sources*, vol. 190, no. 2, pp. 453–460, 2009, doi: 10.1016/j.jpowsour.2009.01.021.
- [19] S. Kim and H. Y. S. Huang, "Mechanical stresses at the cathode-electrolyte interface in lithium-ion batteries," *J Mater Res*, vol. 31, no. 22, pp. 3506–3512, 2016, doi: 10.1557/jmr.2016.373.
- [20] S. Kim, J. Wee, K. Peters, and H. Y. S. Huang, "Multiphysics Coupling in Lithium-Ion Batteries with Reconstructed Porous Microstructures," *Journal of Physical Chemistry C*, vol. 122, no. 10, pp. 5280–5290, 2018, doi: 10.1021/acs.jpcc.7b12388.
- [21] S. Kim, H. Chen, and H. Y. S. Huang, "Coupled Mechanical and Electrochemical Analyses of Three-Dimensional Reconstructed LiFePO₄ by Focused Ion Beam/Scanning Electron Microscopy in Lithium-Ion Batteries," *Journal of Electrochemical Energy Conversion and Storage*, vol. 16, no. 1, pp. 1–7, 2019, doi: 10.1115/1.4040760.
- [22] A. F. Bower, P. R. Guduru, and V. A. Sethuraman, "A finite strain model of stress, diffusion, plastic flow, and electrochemical reactions in a lithium-ion half-cell," *J Mech Phys Solids*, vol. 59, no. 4, pp. 804–828, 2011, doi: 10.1016/j.jmps.2011.01.003.
- [23] C. V. Di Leo, E. Rejovitzky, and L. Anand, "Diffusion-deformation theory for amorphous silicon anodes: The role of plastic deformation on electrochemical performance," *Int J Solids Struct*, vol. 67–68, pp. 283–296, 2015, doi: 10.1016/j.ijsolstr.2015.04.028.
- [24] J. Wen, Y. Wei, and Y. T. Cheng, "Stress evolution in elastic-plastic electrodes during electrochemical processes: A numerical method and its applications," *J Mech Phys Solids*, vol. 116, pp. 403–415, 2018, doi: 10.1016/j.jmps.2018.04.006.
- [25] J. Christensen and J. Newman, "Stress generation and fracture in lithium insertion materials," *Journal of Solid State Electrochemistry*, vol. 10, no. 5, pp. 293–319, 2006, doi: 10.1007/s10008-006-0095-1.
- [26] A. F. Bower, P. R. Guduru, and V. A. Sethuraman, "A finite strain model of stress, diffusion, plastic flow, and electrochemical reactions in a lithium-ion half-cell," *J Mech Phys Solids*, vol. 59, no. 4, pp. 804–828, 2011, doi: 10.1016/j.jmps.2011.01.003.
- [27] C. V. Di Leo, E. Rejovitzky, and L. Anand, "A Cahn-Hilliard-type phase-field theory for species diffusion coupled with large elastic deformations: Application to phase-separating Li-ion electrode materials," *J Mech Phys Solids*, vol. 70, no. 1, pp. 1–29, 2014, doi: 10.1016/j.jmps.2014.05.001.
- [28] G. Bucci, T. Swamy, S. Bishop, B. W. Sheldon, Y.-M. Chiang, and W. C. Carter, "The Effect of Stress on Battery-Electrode Capacity," *J Electrochem Soc*, vol. 164, no. 4, pp. A645–A654, 2017, doi: 10.1149/2.0371704jes.
- [29] F. Larché and J. W. Cahn, "A linear theory of thermochemical equilibrium of solids under stress," *Acta Metallurgica*, vol. 26, no. 1, pp. 53–60, 1973, doi: 10.1016/0001-6160(78)90201-8.
- [30] Z. Liu, J. Zhou, B. Chen, and J. Zhu, "Interaction between dislocation mechanics on diffusion induced stress and electrochemical reaction in a spherical lithium ion battery electrode," *RSC Adv*, vol. 5, no. 91, pp. 74835–74843, 2015, doi: 10.1039/c5ra13991k.

- [31] J. Li, D. Lu, Q. Fang, Y. Liu, and P. Wen, "Cooperative surface effect and dislocation effect in lithium ion battery electrode," *Solid State Ion*, vol. 274, pp. 46–54, 2015, doi: 10.1016/j.ssi.2015.03.004.
- [32] J. Zhu, J. Zhou, B. Chen, Z. Liu, and T. Liu, "Dislocation effect on diffusion-induced stress for lithiation in hollow spherical electrode," *Journal of Solid State Electrochemistry*, vol. 20, no. 1, pp. 37–46, 2016, doi: 10.1007/s10008-015-2999-0.
- [33] P. Yan, J. Zheng, M. Gu, J. Xiao, J. G. Zhang, and C. M. Wang, "Intragranular cracking as a critical barrier for high-voltage usage of layer-structured cathode for lithium-ion batteries," *Nat Commun*, vol. 8, pp. 1–9, 2017, doi: 10.1038/ncomms14101.
- [34] A. Singer *et al.*, "Nucleation of dislocations and their dynamics in layered oxide cathode materials during battery charging," *Nat Energy*, vol. 3, no. 8, pp. 641–647, 2018, doi: 10.1038/s41560-018-0184-2.
- [35] N. A. Sobolev, "Defect engineering in implantation technology of silicon light-emitting structures with dislocation-related luminescence," *Semiconductors*, vol. 44, no. 1, pp. 1–23, 2010, doi: 10.1134/S106378261001001X.
- [36] N. Shin, M. Chi, J. Y. Howe, and M. A. Filler, "Rational defect introduction in silicon nanowires," *Nano Lett*, vol. 13, no. 5, pp. 1928–1933, 2013, doi: 10.1021/nl3042728.
- [37] C. Zhou *et al.*, "Defect Engineering for High-Performance n-Type PbSe Thermoelectrics," *J Am Chem Soc*, vol. 140, no. 29, pp. 9282–9290, 2018, doi: 10.1021/jacs.8b05741.
- [38] C. Yan, G. Chen, J. Sun, C. Lv, and J. Pei, "Edge dislocation surface modification: A new and efficient strategy for realizing outstanding lithium storage performance," *Nano Energy*, vol. 15, pp. 558–566, 2015, doi: 10.1016/j.nanoen.2015.05.011.
- [39] M. S. Whittingham, "Lithium batteries and cathode materials," *Chem Rev*, vol. 104, no. 10, pp. 4271–4301, 2004, doi: 10.1021/cr020731c.
- [40] H.-Y. Shadow Huang and Y.-X. Wang, "Dislocation Based Stress Developments in Lithium-Ion Batteries," *J Electrochem Soc*, vol. 159, no. 6, pp. A815–A821, 2012, doi: 10.1149/2.090206jes.
- [41] V. L. Indenbom and J. Lothe, *Elastic Strain Fields and Dislocation Mobility, Volume 31*, 1st ed. North-Holland, 1992.
- [42] P. Dhiman and H. Y. S. Huang, "Dislocation based stresses during electrochemical cycling and phase transformation in lithium-ion batteries," *Comput Mater Sci*, vol. 171, no. July 2019, p. 109275, 2020, doi: 10.1016/j.commatsci.2019.109275.
- [43] B. Lu, Y. Song, Q. Zhang, J. Pan, Y. T. Cheng, and J. Zhang, "Voltage hysteresis of lithium ion batteries caused by mechanical stress," *Physical Chemistry Chemical Physics*, vol. 18, no. 6, pp. 4721–4727, 2016, doi: 10.1039/c5cp06179b.
- [44] X. Li, Q. Fang, H. Wu, J. Li, Y. Liu, and P. Wen, "Misfit dislocations induced by lithium-ion diffusion in a thin film anode," *Journal of Solid State Electrochemistry*, vol. 21, no. 2, pp. 419–427, 2017, doi: 10.1007/s10008-016-3377-2.
- [45] U. Ulvestad *et al.*, "Topological defect dynamics in operando battery nanoparticles," *Science (1979)*, vol. 348, no. 6241, pp. 1344–1347, 2015, doi: 10.1126/science.aaa1313.
- [46] R. Malik, F. Zhou, and G. Ceder, "Kinetics of non-equilibrium lithium incorporation in LiFePO₄," *Nat Mater*, vol. 10, no. 8, pp. 587–590, 2011, doi: 10.1038/nmat3065.
- [47] X. Zhang *et al.*, "Direct view on the phase evolution in individual LiFePO₄ nanoparticles during Li-ion battery cycling," *Nat Commun*, vol. 6, Sep. 2015, doi: 10.1038/ncomms9333.

- [48] B. Kang and G. Ceder, “Battery materials for ultrafast charging and discharging,” *Nature*, vol. 458, no. 7235, pp. 190–193, 2009, doi: 10.1038/nature07853.
- [49] A. A. Adepoju, M. Doumbia, and Q. L. Williams, “Graphene Nanoplatelet Additives for High C-rate LiFePO₄ Battery Cathodes,” *JOM*, vol. 72, no. 9, pp. 3170–3175, Sep. 2020, doi: 10.1007/s11837-020-04224-2.
- [50] R. Yu *et al.*, “Hierarchically Structured Lithium-Rich Layered Oxide with Exposed Active {010} Planes as High-Rate-Capability Cathode for Lithium-Ion Batteries,” *ACS Sustain Chem Eng*, vol. 5, no. 10, pp. 8970–8981, Oct. 2017, doi: 10.1021/acssuschemeng.7b01773.
- [51] J. H. Kim *et al.*, “Improvement of Thermodynamic Phase Stability and High-Rate Capability of Li Layered Oxides,” *ACS Appl Mater Interfaces*, vol. 15, no. 48, pp. 55837–55847, Dec. 2023, doi: 10.1021/acscami.3c13260.
- [52] K. Yang and M. Tang, “Three-dimensional phase evolution and stress-induced non-uniform Li intercalation behavior in lithium iron phosphate,” *J Mater Chem A Mater*, vol. 8, no. 6, pp. 3060–3070, 2020, doi: 10.1039/c9ta11697d.
- [53] G. Chen, X. Song, and T. J. Richardson, “Electron microscopy study of the LiFePO₄ to FePO₄ phase transition,” *Electrochemical and Solid-State Letters*, vol. 9, no. 6, Jun. 2006, doi: 10.1149/1.2192695.
- [54] D. T. O’Connor, M. J. Welland, W. Kam Liu, and P. W. Voorhees, “Phase transformation and fracture in single Li_xFePO₄ cathode particles: A phase-field approach to Li-ion intercalation and fracture,” *Model Simul Mat Sci Eng*, vol. 24, no. 3, Mar. 2016, doi: 10.1088/0965-0393/24/3/035020.
- [55] C.-K. ChiuHuang and H.-Y. Shadow Huang, “Stress Evolution on the Phase Boundary in LiFePO₄ Particles,” *J Electrochem Soc*, vol. 160, no. 11, pp. A2184–A2188, 2013, doi: 10.1149/2.079311jes.
- [56] G. Kobayashi *et al.*, “Isolation of solid solution phases in size-controlled Li_xFePO₄ at room temperature,” *Adv Funct Mater*, vol. 19, no. 3, pp. 395–403, Feb. 2009, doi: 10.1002/adfm.200801522.
- [57] N. Meethong, H. Y. S. Huang, W. C. Carter, and Y. M. Chiang, “Size-dependent lithium miscibility gap in nanoscale Li_{1-x}FePO₄,” *Electrochemical and Solid-State Letters*, vol. 10, no. 5, pp. 134–138, 2007, doi: 10.1149/1.2710960.
- [58] M. Wagemaker *et al.*, “Dynamic solubility limits in nanosized olivine LiFePO₄,” *J Am Chem Soc*, vol. 133, no. 26, pp. 10222–10228, Jul. 2011, doi: 10.1021/ja2026213.
- [59] D. A. Cogswell and M. Z. Bazant, “Coherency strain and the kinetics of phase separation in LiFePO₄ nanoparticles,” *ACS Nano*, vol. 6, no. 3, pp. 2215–2225, 2012, doi: 10.1021/nn204177u.
- [60] U. S. Kasavajjula, C. Wang, and P. E. Arce, “Discharge Model for LiFePO₄ Accounting for the Solid Solution Range,” *J Electrochem Soc*, vol. 155, no. 11, p. A866, 2008, doi: 10.1149/1.2980420.
- [61] S. Daubner, M. Weichel, D. Schneider, and B. Nestler, “Modeling intercalation in cathode materials with phase-field methods: Assumptions and implications using the example of LiFePO₄,” *Electrochim Acta*, vol. 421, Jul. 2022, doi: 10.1016/j.electacta.2022.140516.
- [62] J. Lim *et al.*, “Origin and hysteresis of lithium compositional spatiodynamics within battery primary particles,” *Science (1979)*, vol. 353, no. 6299, pp. 566–571, 2016, [Online]. Available: <https://www.science.org>

- [63] X. Zhang *et al.*, “Rate-induced solubility and suppression of the first-order phase transition in olivine LiFePO₄,” *Nano Lett*, vol. 14, no. 5, pp. 2279–2285, May 2014, doi: 10.1021/nl404285y.
- [64] H. Liu *et al.*, “Capturing metastable structures during high-rate cycling of LiFePO₄ nanoparticle electrodes,” *Science (1979)*, vol. 344, no. 6191, 2014, doi: 10.1126/science.1252817.
- [65] N. Sharma *et al.*, “Direct evidence of concurrent solid-solution and two-phase reactions and the nonequilibrium structural evolution of LiFePO₄,” *J Am Chem Soc*, vol. 134, no. 18, pp. 7867–7873, May 2012, doi: 10.1021/ja301187u.
- [66] J. Niu *et al.*, “In situ observation of random solid solution zone in LiFePO₄ electrode,” *Nano Lett*, vol. 14, no. 7, pp. 4005–4010, 2014, doi: 10.1021/nl501415b.
- [67] C. Ouyang, S. Shi, Z. Wang, X. Huang, and L. Chen, “First-principles study of Li ion diffusion in LiFePO₄,” *Phys Rev B Condens Matter Mater Phys*, vol. 69, no. 10, Mar. 2004, doi: 10.1103/PhysRevB.69.104303.
- [68] P. Bai, D. A. Cogswell, and M. Z. Bazant, “Suppression of phase separation in LiFePO₄ nanoparticles during battery discharge,” *Nano Lett*, vol. 11, no. 11, pp. 4890–4896, 2011, doi: 10.1021/nl202764f.
- [69] H. Zhao and M. Z. Bazant, “Population dynamics of driven autocatalytic reactive mixtures,” in *PHYSICAL REVIEW E*, American Institute of Chemical Engineers, 2019, doi: 10.1103/PhysRevE.100.012144.
- [70] J. Li, L. E. Downie, L. Ma, W. Qiu, and J. R. Dahn, “Study of the Failure Mechanisms of LiNi_{0.8}Mn_{0.1}Co_{0.1}O₂ Cathode Material for Lithium Ion Batteries,” *J Electrochem Soc*, vol. 162, no. 7, pp. A1401–A1408, 2015, doi: 10.1149/2.1011507jes.
- [71] W. Lee *et al.*, “New Insight into Ni-Rich Layered Structure for Next-Generation Li Rechargeable Batteries,” *Adv Energy Mater*, vol. 8, no. 4, Feb. 2018, doi: 10.1002/aenm.201701788.
- [72] W. S. Yoon, K. Y. Chung, J. McBreen, and X. Q. Yang, “A comparative study on structural changes of LiCo_{1/3}Ni_{1/3}Mn_{1/3}O₂ and LiNi_{0.8}Co_{0.15}Al_{0.05}O₂ during first charge using in situ XRD,” *Electrochem commun*, vol. 8, no. 8, pp. 1257–1262, Aug. 2006, doi: 10.1016/j.elecom.2006.06.005.
- [73] Y. N. Zhou *et al.*, “High-Rate Charging Induced Intermediate Phases and Structural Changes of Layer-Structured Cathode for Lithium-Ion Batteries,” *Adv Energy Mater*, vol. 6, no. 21, Nov. 2016, doi: 10.1002/aenm.201600597.
- [74] A. Grenier *et al.*, “Reaction Heterogeneity in LiNi_{0.8}Co_{0.15}Al_{0.05}O₂ Induced by Surface Layer,” *Chemistry of Materials*, vol. 29, no. 17, pp. 7345–7352, Sep. 2017, doi: 10.1021/acs.chemmater.7b02236.
- [75] A. Grenier *et al.*, “Intrinsic Kinetic Limitations in Substituted Lithium-Layered Transition-Metal Oxide Electrodes,” *J Am Chem Soc*, vol. 142, no. 15, pp. 7001–7011, Apr. 2020, doi: 10.1021/jacs.9b13551.
- [76] R. Robert, C. Bunzli, E. J. Berg, and P. Novák, “Activation Mechanism of LiNi_{0.8}Co_{0.15}Al_{0.05}O₂: Surface and bulk operando electrochemical, differential electrochemical mass spectrometry, and x-ray diffraction analyses,” *Chemistry of Materials*, vol. 27, no. 2, pp. 526–536, Jan. 2015, doi: 10.1021/cm503833b.
- [77] J. Park *et al.*, “Fictitious phase separation in Li layered oxides driven by electroautocatalysis,” *Nat Mater*, vol. 20, no. 7, pp. 991–999, Jul. 2021, doi: 10.1038/s41563-021-00936-1.

- [78] Y. Qi, L. G. Hector, C. James, and K. J. Kim, “Lithium Concentration Dependent Elastic Properties of Battery Electrode Materials from First Principles Calculations,” *J Electrochem Soc*, vol. 161, no. 11, pp. F3010–F3018, 2014, doi: 10.1149/2.0031411jes.
- [79] J. Wen, Y. Wei, and Y. T. Cheng, “Stress evolution in elastic-plastic electrodes during electrochemical processes: A numerical method and its applications,” *J Mech Phys Solids*, vol. 116, pp. 403–415, 2018, doi: 10.1016/j.jmps.2018.04.006.
- [80] A. F. Bower, E. Chason, P. R. Guduru, and B. W. Sheldon, “A continuum model of deformation, transport and irreversible changes in atomic structure in amorphous lithium-silicon electrodes,” *Acta Mater*, vol. 98, pp. 229–241, 2015, doi: 10.1016/j.actamat.2015.07.036.
- [81] C. V. Di Leo, E. Rejovitzky, and L. Anand, “Diffusion-deformation theory for amorphous silicon anodes: The role of plastic deformation on electrochemical performance,” *Int J Solids Struct*, vol. 67–68, pp. 283–296, 2015, doi: 10.1016/j.ijsolstr.2015.04.028.
- [82] A. F. Bower, P. R. Guduru, and E. Chason, “Analytical solutions for composition and stress in spherical elastic-plastic lithium-ion electrode particles containing a propagating phase boundary,” *Int J Solids Struct*, vol. 69–70, pp. 328–342, 2015, doi: 10.1016/j.ijsolstr.2015.05.018.
- [83] H. Dal and C. Miehe, “Computational electro-chemo-mechanics of lithium-ion battery electrodes at finite strains,” *Comput Mech*, vol. 55, no. 2, pp. 303–325, 2014, doi: 10.1007/s00466-014-1102-5.
- [84] G. Bucci, Y. M. Chiang, and W. C. Carter, “Formulation of the coupled electrochemical-mechanical boundary-value problem, with applications to transport of multiple charged species,” *Acta Mater*, vol. 104, pp. 33–51, 2016, doi: 10.1016/j.actamat.2015.11.030.
- [85] B. Kang and G. Ceder, “Battery materials for ultrafast charging and discharging,” *Nature*, vol. 458, no. 7235, pp. 190–193, 2009, doi: 10.1038/nature07853.
- [86] J. Xie, J. F. M. Oudenhoven, P.-P. R. M. L. Harks, D. Li, and P. H. L. Notten, “Chemical Vapor Deposition of Lithium Phosphate Thin-Films for 3D All-Solid-State Li-Ion Batteries,” *J Electrochem Soc*, vol. 162, no. 3, pp. A249–A254, 2015, doi: 10.1149/2.0091503jes.
- [87] A. P. Thompson, S. J. Plimpton, and W. Mattson, “General formulation of pressure and stress tensor for arbitrary many-body interaction potentials under periodic boundary conditions,” *Journal of Chemical Physics*, vol. 131, no. 15, 2009, doi: 10.1063/1.3245303.
- [88] R. B. JONES, “Diffusion Creep in Polycrystalline Magnesium,” *Nature*, vol. 207, no. 70, p. 1965, 1965.
- [89] M. Pharr, Z. Suo, and J. J. Vlassak, “Variation of stress with charging rate due to strain-rate sensitivity of silicon electrodes of Li-ion batteries,” *J Power Sources*, vol. 270, pp. 569–575, 2014, doi: 10.1016/j.jpowsour.2014.07.153.
- [90] M. S. Whittingham, “Lithium batteries and cathode materials,” *Chem Rev*, vol. 104, no. 10, pp. 4271–4301, 2004, doi: 10.1021/cr020731c.
- [91] Y. C. Song, Z. Z. Li, A. K. Soh, and J. Q. Zhang, “Diffusion of lithium ions and diffusion-induced stresses in a phase separating electrode under galvanostatic and potentiostatic operations: Phase field simulations,” *Mechanics of Materials*, vol. 91, pp. 363–371, 2015, doi: 10.1016/j.mechmat.2015.04.015.
- [92] C.-K. ChiuHuang and H.-Y. Shadow Huang, “Stress Evolution on the Phase Boundary in LiFePO₄ Particles,” *J Electrochem Soc*, vol. 160, no. 11, pp. A2184–A2188, 2013, doi: 10.1149/2.079311jes.

- [93] Z. Cui, F. Gao, and J. Qu, "Interface-reaction controlled diffusion in binary solids with applications to lithiation of silicon in lithium-ion batteries," *J Mech Phys Solids*, vol. 61, no. 2, pp. 293–310, 2013, doi: 10.1016/j.jmps.2012.11.001.
- [94] L. I. Sedov, *Mechanics of Continuous Media*. World Scientific, 1997.
- [95] L. I. Sedov, *Introduction to the mechanics of a continuous medium*, 1st ed. Addison-Wesley, 1965.
- [96] S. R. de Groot and P. Mazur, *Non-equilibrium Thermodynamics*. Dover Publications, 2011.
- [97] I. M. Gelfand and S. V. Fomin, *The calculus of variations*. Dover Publications, 2000.
- [98] A. Yamada, H. Koizumi, N. Sonoyama, and R. Kanno, "Phase change in Li_xFePO_4 ," *Electrochemical and Solid-State Letters*, vol. 8, no. 8, pp. 409–413, 2005, doi: 10.1149/1.1945373.
- [99] C. K. ChiuHuang and H. Y. S. Huang, "Critical lithiation for C-rate dependent mechanical stresses in LiFePO_4 ," *Journal of Solid State Electrochemistry*, vol. 19, no. 8, pp. 2245–2253, 2015, doi: 10.1007/s10008-015-2836-5.
- [100] C.-K. ChiuHuang and H.-Y. Shadow Huang, "Stress Evolution on the Phase Boundary in LiFePO_4 Particles," *J Electrochem Soc*, vol. 160, no. 11, pp. A2184–A2188, 2013, doi: 10.1149/2.079311jes.
- [101] R. W. Hertzberg, R. P. Vinci, and J. L. Hertzberg, *Deformation and Fracture Mechanics of Engineering Materials*, 5th Editio. Wiley, 2012.
- [102] M. Tang, H. Y. Huang, N. Meethong, Y. H. Kao, W. C. Carter, and Y. M. Chiang, "Model for the particle size, overpotential, and strain dependence of phase transition pathways in storage electrodes: application to nanoscale olivines," *Chemistry of Materials*, vol. 21, no. 8, pp. 1557–1571, 2009, doi: 10.1021/cm803172s.
- [103] M. . Stern, "Closure to 'Discussion of "Electrochemical Polarization, 1. A Theoretical Analysis of the Shape of Polarization Curves" [M. Stern and A. L. Geary (pp. 56–63, Vol. 104)],'" *J Electrochem Soc*, vol. 104, no. 12, p. 751, 1957, doi: 10.1149/1.2428473.
- [104] H. Wang *et al.*, "Design and synthesis of high performance LiFePO_4/C nanomaterials for lithium ion batteries assisted by a facile H^+/Li^+ ion exchange reaction," *J Mater Chem A Mater*, vol. 3, no. 15, pp. 8062–8069, 2015, doi: 10.1039/c5ta00178a.
- [105] J. P. Jegal and K. B. Kim, "Carbon nanotube-embedding LiFePO_4 as a cathode material for high rate lithium ion batteries," *J Power Sources*, vol. 243, pp. 859–864, 2013, doi: 10.1016/j.jpowsour.2013.06.090.
- [106] P. Zanello, *Inorganic Electrochemistry: Theory, Practice, and Application*. Royal Society of Chemistry, 2003.
- [107] A. J. Bard and L. R. Faulkner, *Electrochemical Methods: Fundamentals and Applications*, 2nd ed. Wiley, 2000.
- [108] A. Yamada *et al.*, "Room-temperature miscibility gap in Li_xFePO_4 ," *Nat Mater*, vol. 5, no. 5, pp. 357–360, 2006, doi: 10.1038/nmat1634.
- [109] A. V. Churikov, A. V. Ivanishchev, I. A. Ivanishcheva, V. O. Sycheva, N. R. Khasanova, and E. V. Antipov, "Determination of lithium diffusion coefficient in LiFePO_4 electrode by galvanostatic and potentiostatic intermittent titration techniques," *Electrochim Acta*, vol. 55, no. 8, pp. 2939–2950, 2010, doi: 10.1016/j.electacta.2009.12.079.
- [110] H. Liu *et al.*, "Capturing metastable structures during high-rate cycling of LiFePO_4 nanoparticle electrodes," *Science (1979)*, vol. 344, no. 6191, 2014, doi: 10.1126/science.1252817.

- [111] P. Wei *et al.*, “Effects of dislocation mechanics on diffusion-induced stresses within a spherical insertion particle electrode,” *J Mater Chem A Mater*, vol. 2, no. 4, pp. 1128–1136, 2014, doi: 10.1039/c3ta13925e.
- [112] Z. Ma, Z. Xie, Y. Wang, and C. Lu, “Softening by electrochemical reaction-induced dislocations in lithium-ion batteries,” *Scr Mater*, vol. 127, pp. 33–36, Jan. 2017, doi: 10.1016/j.scriptamat.2016.08.032.
- [113] Z. Ma, H. Wu, Y. Wang, Y. Pan, and C. Lu, “An electrochemical-irradiated plasticity model for metallic electrodes in lithium-ion batteries,” *Int J Plast*, vol. 88, pp. 188–203, Jan. 2017, doi: 10.1016/j.ijplas.2016.10.009.
- [114] J. Li, Q. Fang, F. Liu, and Y. Liu, “Analytical modeling of dislocation effect on diffusion induced stress in a cylindrical lithium ion battery electrode,” *J Power Sources*, vol. 272, pp. 121–127, 2014, doi: 10.1016/j.jpowsour.2014.07.191.
- [115] S. R. de Groot and P. Mazur, *Non-equilibrium Thermodynamics*. Dover Publications, 2011.
- [116] L. I. Sedov, *Mechanics of Continuous Media*. World Scientific, 1997.
- [117] C. B. Hirschberger, R. H. J. Peerlings, W. A. M. Brekelmans, and M. G. D. Geers, “On the role of dislocation conservation in higher-order crystal plasticity,” *PAMM*, vol. 9, no. 1, pp. 309–310, Dec. 2009, doi: 10.1002/pamm.200910128.
- [118] E. J. Cheng, K. Hong, N. J. Taylor, H. Choe, J. Wolfenstine, and J. Sakamoto, “Mechanical and physical properties of LiNi_{0.33}Mn_{0.33}Co_{0.33}O₂ (NMC),” *J Eur Ceram Soc*, vol. 37, no. 9, pp. 3213–3217, Aug. 2017, doi: 10.1016/j.jeurceramsoc.2017.03.048.
- [119] H. Zhao and M. Z. Bazant, “Population dynamics of driven autocatalytic reactive mixtures,” Jan. 2019, doi: 10.1103/PhysRevE.100.012144.
- [120] R. Pathak *et al.*, “Fluorinated hybrid solid-electrolyte-interphase for dendrite-free lithium deposition,” *Nat Commun*, vol. 11, no. 1, Dec. 2020, doi: 10.1038/s41467-019-13774-2.
- [121] E. A. Kearsley and J. T. Fong, “Linearly independent sets of isotropic Cartesian tensors of ranks up to eight,” *Journal of Research of the National Bureau of Standards, Section B: Mathematical Sciences*, vol. 79B, no. 1, p. 49, 1975, doi: 10.6028/jres.079b.005.
- [122] R. DeHoff, “Thermodynamics in Materials Science.” CRC Press, p. 624, 2006.
- [123] P. O. Persson and G. Strang, “A simple mesh generator in MATLAB,” *SIAM Review*, vol. 46, no. 2, pp. 329–345, 2004, doi: 10.1137/S0036144503429121.
- [124] N. Perrone and R. Kao, “A general finite difference method for arbitrary meshes,” *Comput Struct*, vol. 5, no. 1, pp. 45–57, 1975, doi: 10.1016/0045-7949(75)90018-8.
- [125] S. Takeuchi *et al.*, “Editors’ Choice Communication—Comparison of Nanoscale Focused Ion Beam and Electrochemical Lithiation in β -Sn Microspheres,” *J Electrochem Soc*, vol. 163, no. 6, pp. A1010–A1012, 2016, doi: 10.1149/2.1161606jes.
- [126] Q. Zheng and J. C. Mauro, “Viscosity of glass-forming systems,” *Journal of the American Ceramic Society*, vol. 100, no. 1, pp. 6–25, 2017, doi: 10.1111/jace.14678.
- [127] M. E. Stournara, P. R. Guduru, and V. B. Shenoy, “Elastic behavior of crystalline Li-Sn phases with increasing Li concentration,” *J Power Sources*, vol. 208, pp. 165–169, 2012, doi: 10.1016/j.jpowsour.2012.02.022.
- [128] V. B. Shenoy, P. Johari, and Y. Qi, “Elastic softening of amorphous and crystalline Li-Si Phases with increasing Li concentration: A first-principles study,” *J Power Sources*, vol. 195, no. 19, pp. 6825–6830, 2010, doi: 10.1016/j.jpowsour.2010.04.044.

- [129] D. R. Lide, “CRC Handbook of Chemistry and Physics, Internet Version 2005,” *CRC Press, Taylor and Francis Boca Raton FL*, p. 2660, 2005, doi: 10.1016/0165-9936(91)85111-4.
- [130] J. Marcicki, A. T. Conlisk, and G. Rizzoni, “A lithium-ion battery model including electrical double layer effects,” *J Power Sources*, vol. 251, pp. 157–169, 2014, doi: 10.1016/j.jpowsour.2013.11.001.
- [131] N. Ding *et al.*, “Determination of the diffusion coefficient of lithium ions in nano-Si,” *Solid State Ion*, vol. 180, no. 2–3, pp. 222–225, 2009, doi: 10.1016/j.ssi.2008.12.015.
- [132] J. Shi, Z. Wang, and Y. Q. Fu, “Density functional theory study of diffusion of lithium in Li–Sn alloys,” *J Mater Sci*, vol. 51, no. 6, pp. 3271–3276, 2016, doi: 10.1007/s10853-015-9639-z.
- [133] J. Marcicki, A. T. Conlisk, and G. Rizzoni, “A lithium-ion battery model including electrical double layer effects,” *J Power Sources*, vol. 251, pp. 157–169, 2014, doi: 10.1016/j.jpowsour.2013.11.001.
- [134] Z. Cui, F. Gao, and J. Qu, “A finite deformation stress-dependent chemical potential and its applications to lithium ion batteries,” *J Mech Phys Solids*, vol. 60, no. 7, pp. 1280–1295, 2012, doi: 10.1016/j.jmps.2012.03.008.
- [135] R. Hill, *The Mathematical Theory Of Plasticity*, 2nd ed. Oxford University Press, U.S.A, 1998.
- [136] J. C. Simo and R. L. Taylor, “A return mapping algorithm for plane stress elastoplasticity,” *Int J Numer Methods Eng*, vol. 22, no. 3, pp. 649–670, 1986, doi: 10.1002/nme.1620220310.
- [137] L. H. Wang and S. N. Atluri, “An analysis of an explicit algorithm and the radial return algorithm, and a proposed modification, in finite plasticity,” *Comput Mech*, vol. 13, no. 5, pp. 380–389, 1994, doi: 10.1007/BF00512590.

APPENDICES

APPENDIX A

The auxiliary angles were expressed in the below arctan functions by Indenbom and Lothe [41],

$$\omega = \tan^{-1} \frac{2r_x r_y \lambda \sin \phi}{r_x^2 - \lambda^2 r_y^2}, \quad (\text{A.1})$$

$$\eta_x = \tan^{-1} \frac{r_x^2 \sin 2\phi}{\lambda^2 r_y^2 - r_x^2 \cos 2\phi} \quad (\text{A.2})$$

$$\eta_y = \tan^{-1} \frac{r_y^2 \lambda^2 \sin 2\phi}{r_x^2 - \lambda^2 r_y^2 \cos 2\phi} \quad (\text{A.3})$$

and can be transferred to the forms $\omega = \omega(\psi)$, $\eta_x = \eta_x(\psi)$, and $\eta_y = \eta_y(\psi)$, with $\tan \psi = r_x / r_y$.

However, the range of arctan functions is $(-\pi/2, \pi/2)$. Hence the spatial distributions of ω , η_x , and η_y calculated using Equations (A.1), (A.2), and (A.3) are discontinuous respectively

along the straight lines whose azimuths ψ_ω^* , $\psi_{\eta_x}^*$, and $\psi_{\eta_y}^*$ satisfy the equalities

$$\left(\tan \psi_\omega^*\right)^2 = 1 / \lambda^2, \left(\tan \psi_{\eta_x}^*\right)^2 = \cos 2\phi / \lambda^2, \text{ and } \left(\tan \psi_{\eta_y}^*\right)^2 = \sec 2\phi / \lambda^2. \text{ The discontinuous}$$

auxiliary angles suggest the discontinuity of the displacement at the azimuths ψ_ω^* , $\psi_{\eta_x}^*$, and $\psi_{\eta_y}^*$,

which are not plausible because ψ_ω^* , $\psi_{\eta_x}^*$, and $\psi_{\eta_y}^*$ are independent of the Burgers vectors of

dislocations. To solve this problem, we use differential forms of Equations (A.1), (A.2), and

(A.3). The auxiliary angles can be obtained by numerically solving the equations $[D_\psi] \cdot \omega = \frac{d\omega}{d\psi}$

$$, [D_\psi] \cdot \eta_x = \frac{d\eta_x}{d\psi}, \text{ and } [D_\psi] \cdot \eta_y = \frac{d\eta_y}{d\psi}, \text{ where } \frac{d\omega}{d\psi}, \frac{d\eta_x}{d\psi}, \text{ and } \frac{d\eta_y}{d\psi} \text{ are the derivatives yielded}$$

from the equality $\tan \psi = r_x / r_y$ and Equations (A.1), (A.2), and (A.3). To conveniently calculate

the auxiliary angles for the dislocation with an arbitrary Burgers vector, the independent variable ψ (the azimuth relative to the coordinate frame) is replaced with Ψ , which is the azimuth relative to the Burgers vector, with the range $-\pi < \Psi \leq \pi$ and the equality $\Psi = \psi - \psi_B$, where ψ_B is the azimuth of the Burgers vector.

APPENDIX B

B.1 Introduction to the Metric-based Kinematics of Finite Deformation

The initial configuration and the deformed configuration of a continuum correspond to two spaces with curvilinear coordinate frames $(\zeta^1, \zeta^2, \zeta^3)$ and (η^1, η^2, η^3) respectively. The

differential of radius vector is invariant in both spaces: $d\mathbf{r} = \frac{\partial \mathbf{r}}{\partial \zeta^i} d\zeta^i = \frac{\partial \mathbf{r}}{\partial \eta^j} d\eta^j$. The basis of

initial space and deformed space are defined by $\mathbf{e}_i = \frac{\partial \mathbf{r}}{\partial \zeta^i}$ and $\hat{\mathbf{e}}_j = \frac{\partial \mathbf{r}}{\partial \eta^j}$ respectively, where \wedge

denotes the deformed space. With the function relation $\zeta^i = \zeta^i(\eta^1, \eta^2, \eta^3)$, we have

$d\mathbf{r} = d\eta^j \hat{\mathbf{e}}_j = d\zeta^i \mathbf{e}_i = \frac{\partial \zeta^i}{\partial \eta^j} d\eta^j \mathbf{e}_i$, which yields

$$\hat{\mathbf{e}}_j = \frac{\partial \zeta^i}{\partial \eta^j} \mathbf{e}_i. \quad (\text{B.1.1})$$

The function relation $\eta^i = \eta^i(\zeta^1, \zeta^2, \zeta^3)$ yields

$$d\eta^i = \frac{\partial \eta^i}{\partial \zeta^j} d\zeta^j. \quad (\text{B.1.2})$$

Equations (B.1.1) and (B.1.2) show the transformations between two spaces for the basis and components of $d\mathbf{r}$ respectively. Quantities which transform like the basis of $d\mathbf{r}$, by Equation (B.1.1), is named *covariant*. Quantities which transform like the components of $d\mathbf{r}$, by Equation (B.1.2), is named *contravariant*. Please note the different locations of the dummy indices in Equation (B.1.1) and Equation (B.1.2). The transformations for covariant quantities and contravariant quantities are mutually inverse. The indices of covariant quantities are subscripts.

The indices of contravariant quantities are superscripts. A pair of the same indices that one is subscript and the other is superscripts indicates the Einstein summation convention.

The *metric* of a space is defined as the dot product between two base vectors of the space.

The metric of the initial space is $g_{ij} = \mathbf{e}_i \cdot \mathbf{e}_j$. The contravariant metric g^{ij} is the inverse of g_{ij} :

$[g^{ij}] = [g_{ij}]^{-1}$. We use g^{ij} to introduce the contravariant basis of the initial space: $\mathbf{e}^j = g^{ij} \mathbf{e}_i$.

The deformed space also has the corresponding metric \hat{g}_{ij} and contravariant basis $\hat{\mathbf{e}}^i$.

Based on the invariance of tensors, a 1st order tensor \mathbf{A} and a 2nd order tensor \mathbf{T} respectively satisfy below equations:

$$\mathbf{A} = A^i \mathbf{e}_i = A_i \mathbf{e}^i = \hat{A}^i \hat{\mathbf{e}}_i = \hat{A}_i \hat{\mathbf{e}}^i, \text{ and} \quad (\text{B.1.3})$$

$$\mathbf{T} = T^{ij} \mathbf{e}_i \mathbf{e}_j = T_{ij} \mathbf{e}^i \mathbf{e}^j = T^i_j \mathbf{e}_i \mathbf{e}^j = \hat{T}^{ij} \hat{\mathbf{e}}_i \hat{\mathbf{e}}_j = \hat{T}_{ij} \hat{\mathbf{e}}^i \hat{\mathbf{e}}^j, \quad (\text{B.1.4})$$

where T^i_j and \hat{T}^i_j are called mixed components of \mathbf{T} . The contravariant components, covariant components, and mixed components of \mathbf{T} in different spaces are transformed by

$$\hat{T}^{ij} = T^{kl} \frac{\partial \eta^i}{\partial \zeta^k} \frac{\partial \eta^j}{\partial \zeta^l}, \quad \hat{T}_{ij} = T_{kl} \frac{\partial \zeta^k}{\partial \eta^i} \frac{\partial \zeta^l}{\partial \eta^j}, \text{ and } \hat{T}^i_j = T^k_l \frac{\partial \eta^i}{\partial \zeta^k} \frac{\partial \zeta^l}{\partial \eta^j} \text{ respectively.}$$

The metric of a space can be used to change the indices' location of the tensor components in the space. For example, $A^i = A_j g^{ij}$, and $\hat{T}_{ij} = \hat{T}^{kl} \hat{g}_{ki} \hat{g}_{lj} = \hat{T}^l_i \hat{g}_{lj}$. It can be proved that g_{ij} and g^{ij} are respectively the covariant and contravariant components of a tensor \mathbf{g} , named the *fundamental metric tensor*, whose mixed components are equal to the Kronecker delta: $g^i_k = \mathbf{e}^i \cdot \mathbf{e}_k = g^{ij} g_{jk} = \delta^i_k$. The mixed components of \mathbf{g} are usually used to change the indices of quantities. For example, the trace of \mathbf{T} is calculated by

$$\text{Tr}(\mathbf{T}) = (T^{ij} \mathbf{e}_i \mathbf{e}_j) : (g_{kl} \mathbf{e}^k \mathbf{e}^l) = T^{ij} g_{kl} (\mathbf{e}_i \cdot \mathbf{e}^k) (\mathbf{e}_j \cdot \mathbf{e}^l) = T^{ij} g_{kl} g_i^k g_j^l = T^{ij} g_{ij} = T^i_i = \hat{T}^i_i.$$

We consider the configuration of a deformed continuum as a deformed space. The covariant component of strain for the space deformation is defined as half of the metric change of the space from initial state to final state, as shown below,

$$\varepsilon_{ij} = \frac{1}{2}(\tilde{g}_{ij} - \bar{g}_{ij}), \quad (\text{B.1.5})$$

where ε_{ij} is the covariant component of strain, \tilde{g}_{ij} and \bar{g}_{ij} are the metric of the final space and the initial space respectively. ε_{ij} can be used to introduce two strain tensors with the same covariant components but different contravariant basis: $\tilde{\boldsymbol{\varepsilon}} = \varepsilon_{ij} \tilde{\mathbf{e}}^i \tilde{\mathbf{e}}^j$ and $\bar{\boldsymbol{\varepsilon}} = \varepsilon_{ij} \bar{\mathbf{e}}^i \bar{\mathbf{e}}^j$. The tensor $\tilde{\boldsymbol{\varepsilon}}$ is equivalent to the Green strain tensor when the initial space is undeformed, which is proved below: The final metric and the initial metric are \hat{g}_{ij} and g_{ij} respectively, which indicates

$\hat{\varepsilon}_{ij} = \frac{1}{2}(\hat{g}_{ij} - g_{ij})$, where the $\hat{\ }$ in $\hat{\varepsilon}_{ij}$ emphasizes the basis of deformed space for strain tensor.

With $F^i_j = \frac{\partial \zeta^i}{\partial \eta^j}$, we have

$$\hat{\varepsilon}_{ij} \hat{\mathbf{e}}^i \hat{\mathbf{e}}^j = \frac{1}{2}(\hat{g}_{ij} \hat{\mathbf{e}}^i \hat{\mathbf{e}}^j - g_{ij} \hat{\mathbf{e}}^i \hat{\mathbf{e}}^j) = \frac{1}{2}(g_{kl} F^k_i F^l_j \hat{\mathbf{e}}^i \hat{\mathbf{e}}^j - g_{ij} \hat{\mathbf{e}}^i \hat{\mathbf{e}}^j), \text{ and then} \quad (\text{B.1.6})$$

$$\hat{\varepsilon}_{ij} \hat{\mathbf{e}}^i \hat{\mathbf{e}}^j = \frac{1}{2}[(\mathbf{e}_k \cdot \mathbf{e}_l) F^k_i F^l_j \hat{\mathbf{e}}^i \hat{\mathbf{e}}^j - g_{ij} \hat{\mathbf{e}}^i \hat{\mathbf{e}}^j] = \frac{1}{2}[(F^k_i \hat{\mathbf{e}}^i \cdot \mathbf{e}_k) \cdot (F^l_j \mathbf{e}_l \hat{\mathbf{e}}^j) - g_{ij} \hat{\mathbf{e}}^i \hat{\mathbf{e}}^j] \quad (\text{B.1.7})$$

The deformation gradient is a two-point tensor, which includes the basis of two different spaces.

As the initial space is undeformed, $g_{ij} \hat{\mathbf{e}}^i \hat{\mathbf{e}}^j = \mathbf{I}$. We hence have,

$$\hat{\boldsymbol{\varepsilon}} = \frac{1}{2}(\mathbf{F}^T \cdot \mathbf{F} - \mathbf{I}), \quad (\text{B.1.8})$$

where the right side is the definition of Green strain tensor.

When we decompose a deformation to multiple sequential processes, we have the multiplicative decomposition of deformation gradient and the additive decomposition of strain component. The additive decomposition of strain component (Equation (4.1.11)) is proved as below: For simplicity, we consider two sequential processes for a deformation, (a) and (b). Based on Equation (B.1.5), the covariant component of strain for the process (a) is

$$\hat{\varepsilon}_{ij}^{(a)} = \frac{1}{2} \left(\tilde{g}_{ij}^{(a)} - \bar{g}_{ij}^{(a)} \right) = \frac{1}{2} \left(\tilde{g}_{ij}^{(a)} - g_{ij} \right), \quad (\text{B.1.9})$$

and the covariant component of strain for the process (b) is

$$\hat{\varepsilon}_{ij}^{(b)} = \frac{1}{2} \left(\tilde{g}_{ij}^{(b)} - \bar{g}_{ij}^{(b)} \right) = \frac{1}{2} \left(\hat{g}_{ij} - \bar{g}_{ij}^{(b)} \right). \quad (\text{B.1.10})$$

Because processes (a) and (b) are sequential, we have $\tilde{g}_{ij}^{(a)} = \bar{g}_{ij}^{(b)}$, summing Equations (B.1.9) and (B.1.10) yields the additive decomposition below,

$$\hat{\varepsilon}_{ij} = \hat{\varepsilon}_{ij}^{(a)} + \hat{\varepsilon}_{ij}^{(b)}. \quad (\text{B.1.11})$$

Hence, as two different mathematical forms of decomposing the finite deformation, the multiplicative decomposition of deformation gradient and the additive decomposition of strain component (Equation (4.1.11)) are mutually consistent. Please note that only the covariant components in Lagrangian measure satisfy the additive decomposition of strain component.

In a curvilinear coordinate frame, the covariant derivative and Laplacian for scalars, and the covariant derivatives for the covariant/contravariant components of 1st and 2nd order tensors, are listed below:

$$\nabla_i \varphi = \frac{\partial \varphi}{\partial \zeta^i},$$

$$\nabla^2 \varphi = \frac{\partial^2 \varphi}{\partial \zeta^i \partial \zeta^j} g^{ij} - \frac{\partial \varphi}{\partial \zeta^k} \Gamma_{ij}^k g^{ij},$$

$$\nabla_i w^j = \frac{\partial w^j}{\partial \zeta^i} + w^k \Gamma_{ki}^j,$$

$$\nabla_i w_j = \frac{\partial w_j}{\partial \zeta^i} - w_k \Gamma_{ji}^k,$$

$$\nabla_i H^{jk} = \frac{\partial H^{jk}}{\partial \zeta^i} + H^{lk} \Gamma_{li}^j + H^{jl} \Gamma_{li}^k, \text{ and}$$

$$\nabla_i H_{jk} = \frac{\partial H_{jk}}{\partial \zeta^i} - H_{mk} \Gamma_{ij}^m - H_{jm} \Gamma_{ik}^m,$$

where Γ_{ij}^k is called Christoffel symbols. In Euclidean space and Riemannian Space, Christoffel symbols are calculated as below,

$$\Gamma_{jk}^i = \frac{1}{2} g^{is} \left(\frac{\partial g_{js}}{\partial \zeta^k} + \frac{\partial g_{ks}}{\partial \zeta^j} - \frac{\partial g_{jk}}{\partial \zeta^s} \right).$$

For more information about the metric-based continuum mechanics, see the reference [94].

B.2 Generalized Mass Conservation Equation

A density function f of a continuum can be written as $f = f(Z^1, Z^2, Z^3, t)$ or $f = f(z^1, z^2, z^3, t)$. The rate of the volume integral of f depends on the local rate of f and the deformation of the domain of integration as shown below [94]:

$$\frac{d}{dt} \int_V f dV = \int_V \left[\left(\frac{\partial f}{\partial t} \right)_Z + \nabla \cdot (f \mathbf{v}_v^L) \right] dV, \quad (\text{B.2.1})$$

where \mathbf{v}_v^L is the velocity of the domain of integration of the continuum relative to the lab space.

The rate of f for fixed Lagrangian coordinates of the continuum has two forms below:

$$\frac{df}{dt} = \left(\frac{\partial f}{\partial t} \right)_z + \mathbf{v}_v^L \cdot \nabla f \quad (\text{B.2.2})$$

$$\frac{df}{dt} = \left(\frac{\partial f}{\partial t} \right)_z + \mathbf{v}_v \cdot \nabla f , \quad (\text{B.2.3})$$

where \mathbf{v}_v is the velocity of the domain of integration of the continuum relative to the reference space. The relation between \mathbf{v}_v^L and \mathbf{v}_v is

$$\mathbf{v}_v^L = \mathbf{v}_v + \mathbf{z} . \quad (\text{B.2.4})$$

Substituting Equations (B.2.2), (B.2.3), and (B.2.4) into Equation (B.2.1) yields

$$\frac{d}{dt} \int_V f dV = \int_V \left[\left(\frac{\partial f}{\partial t} \right)_z + \nabla \cdot (f \mathbf{v}_v) + f \nabla \cdot \mathbf{z} \right] dV . \quad (\text{B.2.5})$$

Based on mass conservation for component k , chemical reactions determine the variation of total mass which is equal to the variation of the volume integral of $\rho_{(k)}$, as shown in Equations (B.2.6) and (B.2.7):

$$\frac{dm_{(k)}}{dt} = \int_V \sum_j \xi_{(k)}^{(j)} J^{(j)} dV \quad (\text{B.2.6})$$

$$\frac{dm_{(k)}}{dt} = \frac{d}{dt} \int_V \rho_{(k)}(z^1, z^2, z^3, t) dV . \quad (\text{B.2.7})$$

Setting $f = \rho_{(k)}$ and $\mathbf{v}_v = \mathbf{v}_{(k)}$ in Equation (B.2.5) and combining Equation (B.2.6) yield

Equation (4.1.1).

B.3 Entropy Production Rate

Combining Equations (4.1.12), (4.1.14), (4.1.15) and the divergence theorem yields

$$\delta \int_V u \rho dV = \int_V \left[\rho \delta q + \sum_k \rho_{(k)} \left(\delta \mathbf{r}_{(k)}^L - \delta \mathbf{r}^L \right) \cdot \mathbf{F}_{(k)}^L + \mathbf{p} : \nabla \delta \mathbf{r}^L \right] dV . \quad (\text{B.3.1})$$

Because $\rho dV = dm$, which is conserved mass differential, the variational of the total internal energy for the mass center continuum relates to the functional derivatives with respect to independent variables by

$$\delta \int_V u \rho dV = \int_V \left[\left(\frac{\delta U}{\delta s} \right)_{\mathbf{e},x} \delta s + \sum_l \left(\frac{\delta U}{\delta \hat{\varepsilon}_{ij}^{(l)}} \right)_{s,\mathbf{e}^{(l \neq l)},x} \delta \hat{\varepsilon}_{ij}^{(l)} + \sum_k^{K-1} \left(\frac{\delta U}{\delta x_{(k)}} \right)_{s,\mathbf{e},x_{(k \neq k)}} \delta x_{(k)} \right] \rho dV . \quad (\text{B.3.2})$$

Combining Equations (B.3.1) and (B.3.2), setting $\delta s = ds$, $\delta \hat{\varepsilon}_{ij}^{(l)} = d\hat{\varepsilon}_{ij}^{(l)}$, $\delta x_{(k)} = dx_{(k)}$, $\delta q = dq$,

$\delta \mathbf{r}_{(k)}^L = \mathbf{v}_{(k)}^L dt$, and $\delta \mathbf{r}^L = \mathbf{v}^L dt$ (variational are arbitrary and can be set following the real process), and using Equation (4.1.4) yield

$$\rho T ds + \sum_l \hat{\sigma}^{(l)ij} d\hat{\varepsilon}_{ij}^{(l)} + \sum_k^{K-1} \rho \mu_{(kk)} dx_{(k)} = \rho dq + \sum_k \mathbf{J}_{(k)} \cdot \mathbf{F}_{(k)}^L dt + \mathbf{p} : \nabla \mathbf{v}^L dt . \quad (\text{B.3.3})$$

We assume that \mathbf{p} is a symmetric tensor. Using the kinematic relations Equations (B.3.4) and (B.3.5) for strain rate and strains yields Equation (B.3.6):

$$\dot{\varepsilon}_{ij} = \frac{1}{2} \left(\nabla_i v_j^L + \nabla_j v_i^L \right) , \quad (\text{B.3.4})$$

$$\hat{\varepsilon}_{ij} = \sum_l \hat{\varepsilon}_{ij}^{(l)} , \text{ and} \quad (\text{B.3.5})$$

$$\mathbf{p} : \nabla \mathbf{v}^L dt = \mathbf{p} : \dot{\varepsilon} dt = \hat{p}^{ij} d\hat{\varepsilon}_{ij} = \sum_l \hat{p}^{ij} d\hat{\varepsilon}_{ij}^{(l)} . \quad (\text{B.3.6})$$

Then, substituting $\sum_k^K \mathbf{J}_{(k)} = 0$, the definition of heat flux $\rho dq = -\nabla \cdot \mathbf{J}_Q dt$, Equations (4.1.26),

(4.1.27), and (B.3.6) into Equation (B.3.3) yields Equations (B.3.7), (B.3.8), and (B.3.9) for entropy change, entropy flow and entropy production rate, respectively. Using Equations (B.3.10) and (4.1.25) we have Equation (4.1.24).

$$\rho \frac{ds}{dt} = -\nabla \cdot \mathbf{J}_s + \theta, \quad (\text{B.3.7})$$

$$\mathbf{J}_s = \frac{1}{T} \left(\mathbf{J}_Q - \sum_k^{K-1} \mu_{(kK)} \mathbf{J}_{(k)} \right), \quad (\text{B.3.8})$$

$$T\theta = -\mathbf{J}_s \cdot \nabla T + \sum_l (p^{ij} - \sigma^{(l)ij}) \frac{d\hat{\epsilon}_{ij}^{(l)}}{dt} - \sum_k^{K-1} \mathbf{J}_{(k)} \cdot \nabla \Psi_{(kK)}^L + \sum_j J^{(j)} A_C^{(j)}, \text{ and} \quad (\text{B.3.9})$$

$$\hat{e}_{ij}^{(l)} = \frac{d\hat{\epsilon}_{ij}^{(l)}}{dt}. \quad (\text{B.3.10})$$

B.4 Relative Chemical Potential

Because s is assumed to be independent of $\nabla x_{(1)}$ and $\nabla \boldsymbol{\epsilon}^{(l)}$, we have

$$\left(\frac{\partial s}{\partial x_{(1)}} \right)_{T, \dots} = f(x_{(1)}, \hat{\boldsymbol{\epsilon}}_{ij}^{(l)}). \quad (\text{B.4.1})$$

It yields

$$d \left[T \left(\frac{\partial s}{\partial x_{(1)}} \right)_{T, \dots} \right] = \left(\frac{\partial s}{\partial x_{(1)}} \right)_{T, \dots} dT + T \left(\frac{\partial^2 s}{\partial x_{(1)}^2} \right)_{T, \dots} dx_{(1)} + \sum_l T \left(\frac{\partial^2 s}{\partial x_{(1)} \partial \hat{\epsilon}_{ij}^{(l)}} \right)_{T, \dots} d\hat{\epsilon}_{ij}^{(l)}. \quad (\text{B.4.2})$$

Based on the symmetry of the 2nd order derivatives of a_F , Equations (4.1.30) and (4.1.31) yield

$$\sum_l T \left(\frac{\partial^2 s}{\partial x_{(1)} \partial \hat{\epsilon}_{ij}^{(l)}} \right)_{T, \dots} d\hat{\epsilon}_{ij}^{(l)} = \sum_l - \left(\frac{\partial \hat{\gamma}^{(l)ij}}{\partial x_{(1)}} \right)_{T, \dots} T d\hat{\epsilon}_{ij}^{(l)}. \quad (\text{B.4.3})$$

Substituting Equation (B.4.3) into Equation (B.4.2), we have

$$\left(\frac{\partial s}{\partial x_{(1)}} \right)_{T, \dots} dT + T \left(\frac{\partial^2 s}{\partial x_{(1)}^2} \right)_{T, \dots} dx_{(1)} = d \left[T \left(\frac{\partial s}{\partial x_{(1)}} \right)_{T, \dots} \right] + T \left(\frac{\partial \gamma}{\partial x_{(1)}} \right)_{T, \dots} \hat{g}^{ij} d\hat{\varepsilon}_{ij}^{(e)} . \quad (\text{B.4.4})$$

Using Equation (B.4.4) in Equation (4.1.33) yields

$$d\mu_{HOM(12)} = -d \left[T \left(\frac{\partial s}{\partial x_{(1)}} \right)_{T, \dots} \right] - T \left(\frac{\partial \gamma}{\partial x_{(1)}} \right)_{T, \dots} \hat{g}^{ij} d\hat{\varepsilon}_{ij}^{(e)} + \kappa \hat{g}^{ij} d\hat{\varepsilon}_{ij}^{(e)} + \left(\frac{\partial^2 u}{\partial x_{(1)}^2} \right)_{T, \dots} dx_{(1)} . \quad (\text{B.4.5})$$

The parameter tensors with the 1st and 3rd orders are zero in isotropic material [94]. Using Equation (4.1.29) we simplify Equation (4.1.34) to

$$d\hat{\mu}_{INH(12)}^i = \hat{\omega}_{\nabla(12)}^{rspi} d\hat{\nabla}_p \hat{\varepsilon}_{rs}^{(e)} + K_{(12)} \hat{g}^{iq} d\hat{\nabla}_q x_{(1)} , \quad (\text{B.4.6})$$

with defining a material property

$$\frac{\partial^2 u}{\partial \hat{\nabla}_i x_{(1)} \partial \hat{\nabla}_q x_{(1)}} = \hat{K}_{\nabla(12)}^{iq} = K_{(12)} \hat{g}^{iq} . \quad (\text{B.4.7})$$

The specific entropy s is related to the molar entropy s_M composed of a fraction part

$s_{MF} = s_{MF}(y'_{(1)})$ and a deformation part $s_{MD} = s_{MD}(\varepsilon_{ij}^{(l)})$ as shown below:

$$s = \frac{S}{m} = \frac{N_{(2)} N_B}{m} s_M = x_{(2)} \frac{N_B}{M_{(2)}} (s_{MF} + s_{MD}) . \quad (\text{B.4.8})$$

The fraction part obeys the entropy of the ideal solution as shown below [122]:

$$s_{MF} = -R \left[y'_{(1)} \ln y'_{(1)} + (1 - y'_{(1)}) \ln(1 - y'_{(1)}) \right] . \quad (\text{B.4.9})$$

Equation (B.4.9) yields

$$\frac{\partial}{\partial x_{(1)}} \left(x_{(2)} \frac{N_B}{M_{(2)}} s_{MF} \right)_{T, \dots} = -R \left[\frac{1}{M_{(1)}} \ln \frac{y'_{(1)}}{y'_{(2)}} - \frac{N_B}{M_{(2)}} \ln y'_{(2)} \right] . \quad (\text{B.4.10})$$

We define the excess relative chemical potential as below:

$$\mu_{EX(12)} = \mu_{HOM(12)} + T \frac{\partial}{\partial x_{(1)}} \left(x_{(2)} \frac{N_B}{M_{(2)}} s_{MF} \right)_{T, \dots} . \quad (\text{B.4.11})$$

Substituting Equations (B.4.8) and (B.4.11) into Equation (B.4.5) yields

$$d\mu_{EX(12)} = \frac{N_B}{M_{(2)}} T ds_{MD} - T \left(\frac{\partial \gamma}{\partial x_{(1)}} \right)_{T, \dots} \hat{g}^{ij} d\hat{\varepsilon}_{ij}^{(e)} + \kappa \hat{g}^{ij} d\hat{\varepsilon}_{ij}^{(e)} + \left(\frac{\partial^2 u}{\partial x_{(1)}^2} \right)_{T, \dots} dx_{(1)} , \quad (\text{B.4.12})$$

where γ is related to the stiffness and thermal expansion ratio as shown below

$$\begin{aligned} \hat{\gamma}^{(e)ij} &= \gamma \hat{g}^{ij} = - \frac{\partial}{\partial \hat{\varepsilon}_{kl}^{(e)}} \left(\frac{\hat{\sigma}_{HOM}^{ij}}{\rho} \right)_{x_{(1)}, \hat{\varepsilon}_{mn}^{(e)}} \left(\frac{\partial \hat{\varepsilon}_{kl}^{(e)}}{\partial T} \right)_{\frac{\sigma_{HOM}}{\rho}} . \\ &= - \left(\lambda_{\rho} \hat{g}^{ij} \hat{g}^{kl} + G_{\rho} \hat{g}^{ik} \hat{g}^{jl} + G_{\rho} \hat{g}^{il} \hat{g}^{jk} \right) \alpha_T \hat{g}_{kl} \end{aligned} \quad (\text{B.4.13})$$

Thus, the coupling coefficient in the relative chemical potential of an isotropic material is

$$K_D = \kappa - T \left(\frac{\partial \gamma}{\partial x_{(1)}} \right)_{T, \dots} - \frac{T}{x_{(2)}} \gamma . \quad (\text{B.4.14})$$

With defining a material property $h = \left(\frac{\partial^2 u}{\partial x_{(1)}^2} \right)_{T, \dots}$, substituting Equation (B.4.14) into Equation

(B.4.12) yields Equation (4.1.80).

We assume $\hat{\mu}_{INH(12)}^i$ is a 1st order homogeneous function of $\hat{\nabla}_p \hat{\varepsilon}_{rs}^{(e)}$ and $\hat{\nabla}_q x_{(1)}$. Equation

(B.4.6) yields

$$\hat{\mu}_{INH(12)}^i = \hat{\omega}_{\nabla}^{rspi} \hat{\nabla}_p \hat{\varepsilon}_{rs}^{(e)} + K_{(12)} \hat{g}^{iq} \hat{\nabla}_q x_{(1)} , \quad (\text{B.4.15})$$

where $\hat{\omega}_{\nabla}^{rspi}$ for isotropic material satisfies

$$\hat{\omega}_{\nabla}^{rspi} = \omega_I \hat{g}^{rs} \hat{g}^{pi} + \omega_{IIA} \hat{g}^{rp} \hat{g}^{si} + \omega_{IIB} \hat{g}^{ri} \hat{g}^{sp} . \quad (\text{B.4.16})$$

For simplicity, we assume $\omega_{IIA} = \omega_{IIB} = 0$. Combining Equations (4.1.21), (B.4.10), (B.4.11),

(B.4.15) and (B.4.16) yields Equation (4.1.81). If $\left(\frac{\partial \gamma}{\partial x_{(1)}}\right)_{T,\dots} = 0$, we have Equation (4.1.82).

Equation (4.1.83) is obtained from Equation (B.4.13).

B.5 Transformed Equations

We divide the relative chemical potential into a homogeneous-logarithm part and an inhomogeneous-excess part, $\mu_{(12)} = \mu_{HL(12)} + \mu_{IE(12)}$ with

$$\mu_{HL(12)} = RT \left[\frac{1}{M_{(1)}} \ln \frac{y'_{(1)}}{y'_{(2)}} - \frac{N_B}{M_{(2)}} \ln y'_{(2)} \right]. \quad (\text{B.5.1})$$

Using Equations (4.1.81) and (B.5.1) yields Equation (4.1.98). Combining Equations (4.1.35), (4.1.36), (4.1.37), (4.1.62), (4.1.81), (4.1.85), (4.1.86), and (4.1.98) yields Equations (4.1.84) and (4.1.89). Combining Equations (4.1.12), (4.1.13), and $\mathbf{v}^L = \mathbf{v} + \mathbf{v}_{(2)}^L$ yields Equation (4.1.87). Using Equations (4.1.48) and (4.1.60) we have Equation (4.1.88).

B.6 Relation between D and L

Using Equations (4.1.5) and (4.1.35), the flux of Li^+ can be written as

$$\mathbf{J}_{(1)} = \rho_{(1)} x_{(2)} \mathbf{v}_{(1)} = c_{(1)} M_{(1)} x_{(2)} \mathbf{v}_{(1)}, \quad (\text{B.6.1})$$

where $c_{(1)}$ is the concentration of Li^+ . To estimate the relation between D and L , we only

consider $\mu_{HL(12)}$ in the diffusion for simplicity, as shown below,

$$\mathbf{J}_{(1)} \approx -\frac{L}{T} \nabla \mu_{HL(12)} = -LR \left(\frac{1}{M_{(1)} y'_{(1)} y'_{(2)}} + \frac{N_B}{M_{(2)} y'_{(2)}} \right) \nabla y'_{(1)}. \quad (\text{B.6.2})$$

The Fick's 1st law yields

$$c_{(1)} \mathbf{v}_{(1)} = -D \nabla c_{(1)} = -D c_{MAX} \nabla y'_{(1)} = -D \frac{N_B \rho_{(2)}}{M_{(2)}} \nabla y'_{(1)}. \quad (\text{B.6.3})$$

Combining Equations (B.6.1), (B.6.2), (B.6.3), and (4.1.63) yields the expression of D as shown below,

$$D = \frac{RL_0 f_L \left(M_{(2)} + M_{(1)} N_B y'_{(1)} \right)^2}{N_B \rho_{(2)} M_{(1)}^2 M_{(2)} y'_{(1)} y'_{(2)}}. \quad (\text{B.6.4})$$

B.7 Differential of Expanded Surface Area

Initially, the area differential of the particle surface is governed by

$$|dl_0|^2 = g_{(2)ij}^{\circ} dz^i dz^j = (dz^1)^2 + (dz^3)^2 \quad (\text{B.7.1})$$

and

$$|d\zeta_0|^2 = g_{(2)22}^{\circ} (dz^2)^2 = (z^1)^2 (dz^2)^2, \quad (\text{B.7.2})$$

where dl_0 is the initial length of the infinitesimal arc perpendicular to the initial basis vector \mathbf{e}_2 on the particle surface and $d\zeta_0$ is the initial length of the infinitesimal arc parallel to the initial basis vector \mathbf{e}_2 on the particle surface. After the particle is deformed, the lengths of the infinitesimal arcs have

$$|dl|^2 = g_{(2)ij} dz^i dz^j = g_{(2)11} (dz^1)^2 + 2g_{(2)13} dz^1 dz^3 + g_{(2)33} (dz^3)^2 \quad (\text{B.7.3})$$

and

$$|d\zeta|^2 = g_{(2)22} (dz^2)^2 = (Z^1)^2 (dz^2)^2, \quad (\text{B.7.4})$$

where dl is the length of the infinitesimal arc perpendicular to the basis vector \mathbf{e}_2 on the particle surface and $d\zeta$ is the length of the infinitesimal arc parallel to the basis vector \mathbf{e}_2 on the particle surface. Hence, the initial and present area differentials respectively have

$$(dA_0)^2 = |dl_0|^2 |d\zeta_0|^2 \quad (\text{B.7.5})$$

and

$$(dA)^2 = |dl|^2 |d\zeta|^2 . \quad (\text{B.7.6})$$

Combining Equations (B.7.1), (B.7.2), (B.7.3), (B.7.4), (B.7.5), and (B.7.6) yields Equation (4.1.106).

B.8 The Component of $\mathbf{v}^{L(2)}$ in the Lab Space

The relation between the components of a tensor in different coordinate frames yields Equations (4.1.116) and (B.8.1) [94],

$$g_{(2)ij} = g_{pq}^L \frac{\partial Z^p}{\partial z^i} \frac{\partial Z^q}{\partial z^j} , \quad (\text{B.8.1})$$

where g_{pq}^L is the metric of lab space. Using Equation (B.8.1) we have Equation (4.1.113). If we

assume $\frac{\partial Z^3}{\partial z^1} < 0$ and $\frac{\partial Z^3}{\partial z^3} > 0$, Equation (B.8.1) implies Equations (4.1.114) and (4.1.115).